Strål
säkerhets
myndigheten
Swedish Radiation Safety Authority

Author: Joel E. Geier

Technical Note

2015:40

Assessment of flow-related transport parameters used in the SR-Site safety case

Report number: 2015:40 ISSN: 2000-0456
Available at www.stralsakerhetsmyndigheten.se

SSM perspektiv

Bakgrund

Strålsäkerhetsmyndigheten (SSM) granskar Svensk Kärnbränslehantering AB:s (SKB) ansökningar enligt lagen (1984:3) om kärnteknisk verksamhet om uppförande, innehav och drift av ett slutförvar för använt kärnbränsle och av en inkapslingsanläggning. Som en del i granskningen ger SSM konsulter uppdrag för att inhämta information i avgränsade frågor. I SSM:s Technical note-serie rapporteras resultaten från dessa konsultuppdrag.

Projektets syfte

Föreliggande projekt syftar till att granska SKB:s beräkningar av så kallade flödesrelaterade prestandamått. SKB har definierat tre prestandamått som avser Darcyhastigheterna vid deponeringshålen, flödestider från deponeringshålen till biosfären och F-faktorn vilken relaterar till den flödesvätta ytan för sprickorna längs flödesvägarna från deponeringshålen till biosfären. Därutöver är målsättningen att bedöma SKB:s beräkningar av nedträngning av utspädda vatten till förvarsdjup, påverkan på flödet av termiska effekter orsakade av det radioaktiva avfallet samt hur undersökningsborrhål kan påverka flödena i berget på lång sikt. SSM har givit i uppdrag att genomföra en granskning baserad på en förenklad diskret spricknätverksmodell för flöde genom berget. Modellen har parameteriserats med SKB:s platsundersökningsdata.

Författarsammanfattning

Flödesrelaterade prestandamått som används i SKB:s säkerhetsanslys SR-Site utvärderas både genom en granskning av SKB:s hantering av osäkerheter samt oberoende beräkningar baserade på en förenklad modell. Ytterligare frågor i samband med grundvattenflöden som behandlas i denna granskning omfattar salthaltens utveckling, nedträngning av utspädda vatten till förvarsdjup, effekter av borrhål på flödet i slutförvarets närområde samt termiska effekter som orsakas av det radioaktiva avfallet.

En enkel modell av kopplade flödande sprickor används för att producera rimligt konservativa uppskattningar av SKB:s definierade prestandamått. Dessa uppskattningar baseras på SKB: s parametrisering av det hydrogeologiska diskreta spricknätverket (DFN), inte på en fullständig analys av källdata. Detta förhållandevis enkla angreppsätt ger en transparent metod för att kontrollera de betydligt mer komplexa DFN-modeller som används av SKB.

Resultaten överensstämmer i huvudsak med SKB: s DFN-hydromodeller, vilket tyder på att de prestandamått som resulterar från DFN-modellerna är avhängiga samma faktorer som styr den enkla modellen, nämligen storlek och transmissivitet i första sprickan längs en flödesväg som ansluter till ett givet deponeringshål.

Den viktigaste skillnaden mellan SKB:s basmodell för det geologiska spricknätverket och SKB:s alternativa modeller (de så kallade OSM-TFM och TCM modellerna) är antalet anslutna deponeringshål. Båda alternativa geologiska DFN-modellerna leder till fler deponeringshål som skärs av sprickor. Men de kumulativa fördelningarna för prestandamåtten stämmer väl överens med resultaten för den så kallade r0-fixerade modellen som SKB använder som basfall.

SKB:s modeller för beräkning av salthaltsutvecklingen är rimliga och matematiskt sofistikerade, men deras tillförlitlighet begränsas av den tillgängliga mängden data på djupet. Generellt sett är dock SKB:s metod för att beräkna risken för att utspädda vatten ska tränga ner till deponeringshål konservativ. Ett icke-konservativt antagande är att hela bergmatrisen mellan vattenförande sprickor är tillgänglig för matrisdiffusion. Ett mer konservativt antagande skulle vara att anta att diffusionsdjupet är heterogent och mer begränsat.

SKB:s analys av effekter av undersökningsborrhål täcker in de viktigaste fallen som kan öka flödet till deponeringshål, men antalet simuleringar för varje fall är begränsat. Ett flertal variabler som skulle kunna påverka säkerheten har inte analyserats.

SKB behandlar oförseglade borrhål som en hydrogeologisk variant snarare än som en del av riskbedömningen i SR-Site. Kopplade effekter av två eller flera borrhål har inte analyserats, men relevanta överslagsberäkningar som hanterar samverkan av flera borrhål skulle kunna begäras för att kontrollera om ökat flöde i ett system som liknar ett U-rör skulle kunna inträffa (till exempel om det skulle uppstå en så kallad ”common mode failure” som är förknippad med borrhålstätningsmetoden).

SKB:s överslagsberäkningar rörande termiska effekter på flödet begränsas genom en kontinuumrepresentation av flödesdomänen och genom att viskositetens minskning med förhöjd temperatur försummas. Minskad viskositet skulle kunna öka långsiktiga flöden med uppskattningsvis upp till en faktor fyra de första 1000 åren av den tempererade perioden. SKB:s slutsats att utsläppspunkter till biosfären inte är känsliga för termiska effekter kanske inte är tillförlitlig för en diskret representation av flödesdomänen. Det verkar dock osannolikt att en förändring av flödesvägarna pga. termisk inverkan avsevärt skulle ändra säkerhetsanalysens viktigaste slutsatser.

Projektinformation
Kontaktperson på SSM: Georg Lindgren
Diarienummer ramavtal: SSM2011-3629
Diarienummer avrop: SSM2014-1403
Aktivitetsnummer: 3030012-4091

SSM perspective

Background

The Swedish Radiation Safety Authority (SSM) reviews the Swedish Nuclear Fuel Company's (SKB) applications under the Act on Nuclear Activities (SFS 1984:3) for the construction and operation of a repository for spent nuclear fuel and for an encapsulation facility. As part of the review, SSM commissions consultants to carry out work in order to obtain information on specific issues. The results from the consultants' tasks are reported in SSM's Technical Note series.

Objectives of the project

The objective of this project is to review SKB's calculations of flow related performance measures. SKB has defined three performance measures concerning Darcy velocities at the deposition holes, travel times from the deposition holes to the biosphere, and the F-factor which is related to the flow-wetted surface in the fractures along the flow path from the deposition holes to the biosphere. In addition, the objective is to evaluate SKB's calculations of penetration of diluted water to repository depth, the influence of thermal effects caused by the radioactive waste, and effect of investigation boreholes on long-term flows. The review is based on a simplified discrete fracture network model for flow through the rock. The model is parameterized with SKB's site investigation data.

Summary by the author

Flow-related performance measures used in the SR-Site safety case by the Swedish Nuclear Fuel and Waste Management Co. (SKB) are evaluated both by review of the handling of uncertainties and by independent calculations based on a simple model. Additional groundwater flow issues considered in this review include salinity evolution, fresh water penetration, effects of boreholes and thermal effects of the radioactive waste.

A simple series-conductor model is used to produce reasonably conservative estimates of performance parameters. These estimates are based on SKB's derivation of hydrogeological discrete-fracture network (DFN) model parameters, not a full re-analysis of the source data. However this very simple approach provides a transparent method for checking the much more complex DFN models used by SKB.

The results agree substantially with SKB's DFN models, indicating that the performance measures produced by the DFN models are strongly determined by the same factors that control the simple model, namely the size and transmissivity of the first fracture in a flow path that connects to a given deposition hole.

The main effects of the OSM-TFM and TCM alternative geological DFN models are in terms of the number of connected deposition holes; both of these produce more connected holes. However the cumulative density functions of performance parameters are nearly identical to the results for the r0-fixed alternative that SKB uses as a base case.

SKB's models for salinity evolution are reasonable and mathematically sophisticated, but their reliability is constrained by the limited amount of data at depth. However, generally SKB's approach to calculating the risk of dilute waters penetrating to deposition holes is conservative. One non-conservative assumption is that the entire matrix between transmissive fractures is uniformly accessible for matrix diffusion. A more conservative assumption would be that diffusion depths are more limited and heterogeneous.

SKB's analysis of borehole effects covers the main cases that could enhance flow to deposition holes, but the number of simulations for each case is very small. Numerous additional variables that could affect the impact on safety have not been analyzed.

Unsealed boreholes are treated as a hydrogeological variant rather than as part of the SR-Site risk assessment. Coupled effects of two or more boreholes have not been analyzed, but relevant preliminary results for multiple boreholes could be requested to check if U-tube enhanced flow paths could occur (for example if there is a common-mode failure of borehole sealing methods).

SKB's scoping evaluation of thermal effects on flow is limited by use of a continuum representation, and by neglecting viscosity reduction due to heating, which could reasonably enhance long-term flowrates by a factor of up to four for the first 1000 years of the temperate period. SKB's conclusions on insensitivity of discharge locations to thermal effects may not be reliable for a discrete representation. However it seems it seems doubtful that that thermal path-switching phenomena would significantly alter the main conclusions of the safety case.

Project information
Contact person at SSM: Georg Lindgren

Strål
säkerhets
myndigheten
Swedish Radiation Safety Authority

Author: Joel E. Geier
Clearwater Hardrock Consulting
Corvallis, Oregon, U.S.A

Technical Note 84

2015:40

Assessment of flow-related transport parameters used in the SR-Site safety case

Date: October 2015
Report number: 2015:40 **ISSN:** 2000-0456
Available at www.stralsakerhetsmyndigheten.se

This report was commissioned by the Swedish Radiation Safety Authority (SSM). The conclusions and viewpoints presented in the report are those of the author(s) and do not necessarily coincide with those of SSM.

Contents

1. Introduction

In support of the SR-Site safety case, the Swedish Nuclear Fuel and Waste Management Co. (SKB) has presented performance-assessment calculations that are based on calculated distributions of the following flow-related far-field migration parameters or *performance measures*:

U_r = equivalent flux at the release point (from a deposition hole) [L/T]
Q_{eq} = equivalent flow rate (to a deposition hole) [L^3/T]
t_w = advective travel time (from a deposition hole to the biosphere) [T]
F = transport resistance (integrated along the discharge path) [T/L]

These parameters are derived from groundwater flow simulations, as summarized in Sections 6.6 and 6.7 of the SR-Site Data Report (SKB TR-10-52).

The groundwater flow calculations that provide quantitative support for the chosen distributions of performance parameters are described in more detail by Joyce et al. (2010) and Vidstrand et al. (2010). The hydrogeological models are based, in varying degrees, on upscaling from a discrete-fracture-network (DFN) conceptual model of the sparsely fractured bedrock, to equivalent continuum representations. Physical processes that affect groundwater flow, including meteoric water infiltration, land uplift, permafrost development and glaciation in future climates, density-dependent flow and coupled diffusion of variably saline groundwater are taken into account in varying degrees, depending on the particular model and calculation case.

The main goals of this assignment are:

- to assess the reasonableness of the flow-related far-field transport parameters (performance measures) resulting from SKB's hydrogeological calculations with respect to how uncertainties have been handled in view of their use in the consequence analysis calculations, and

- to develop reasonably conservative estimates of the performance parameters u_r, t_r, F_r, and L_r. that can be used for independent assessment of consequences for safety.

These goals are addressed in Section 2 of this technical note by a combination of review of SKB's calculations and interpretations, and by implementation and application of a simple, transparent model that yields conservative, alternative estimates of the performance measures.

Additional goals were to address a series of specific modelling topics relating to SKB's treatment of salinity evolution and freshwater penetration, the effects of boreholes, and thermal effects from waste on groundwater flow. These topics are assessed in Sections 3, 4, and 5 respectively.

An integrated assessment of all of these topics is provided in Section 6.

2. Evaluation of performance measures

2.1. SKB's presentation

2.1.1. SKB's approach to estimation of performance measures

SKB's approach to evaluation of flow-related far-field migration parameters for use in SR-Site performance assessment calculations is summarized in Section 6.7 of the SR-Site Data Report (SKB TR 10-52). The parameters:

U_r = equivalent flux at the release point (from a deposition hole) [L/T]
Q_{eq} = equivalent flow rate (to a deposition hole) [L^3/T]
t_w = advective travel time (from a deposition hole to the biosphere) [T]
F = transport resistance (integrated along the discharge path) [T/L]

are derived from groundwater flow simulations as summarized in Section 6.6 of the same report, and as described in more detail in the modelling reports by Joyce et al. (2010) and Vidstrand et al. (2010).

The groundwater flow simulations by Joyce et al. (2010) and Vidstrand et al. (2010) are based on models that use different conceptualizations for different scales and components of the geosphere and engineered-barrier system. An equivalent-continuum porous-medium (ECPM) representation of the bedrock at larger scales is based on upscaling from a discrete-fracture-network (DFN) model at smaller scales. The ECPM also incorporates the inferred geometry and hydraulic properties of hydraulic conductor domains (HCDs, i.e. brittle deformation zones that are considered to be hydrogeologically significant), on scales above 1 km.

These different submodels are combined in a single flow model (Figure 1) that includes both 3D elements (representing blocks of the ECPM) and 2D elements (representing discrete fractures in the DFN), with coupling at nodes and edges that are shared between the different components. Groundwater pressures and fluxes are calculated by the finite-element method.

SKB's method for obtaining equivalent flow rates Q_{eq}, from this type of model are detailed in Section 3.2.5 of Joyce et al. (2010). Three different conceptual pathways for release of radionuclides were considered:

Q1: release into the fractured bedrock around a deposition hole;
Q2: release into the excavation-damaged zone (EDZ) at the top of the hole;
Q3: release into the backfilled tunnel.

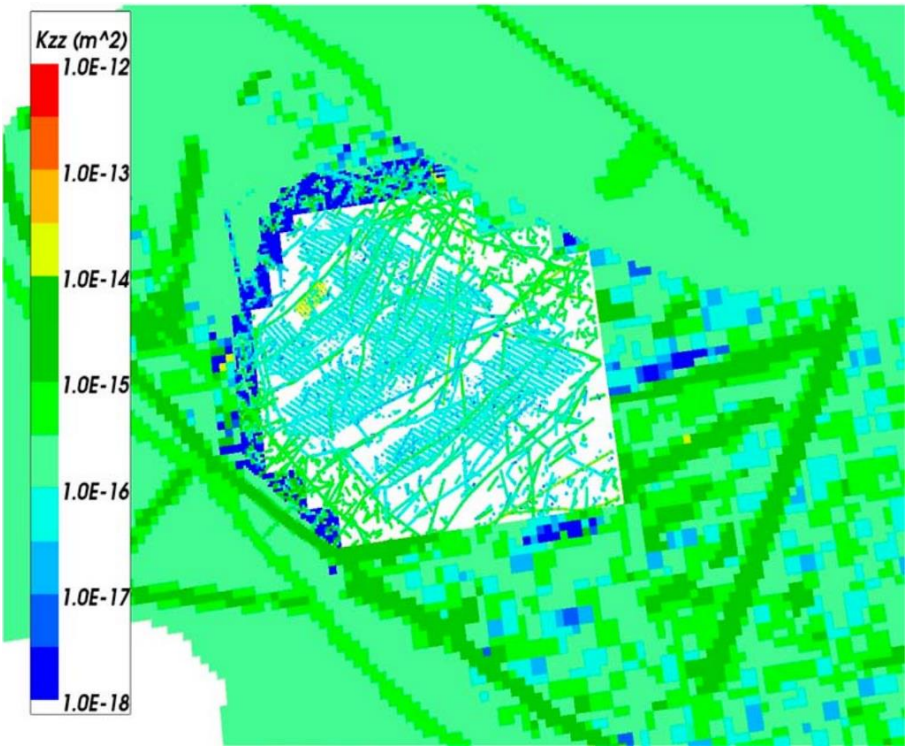

Figure 1: Horizontal cross-section through one of the multi-scale models used for calculation of groundwater flow and flow-related performance measures for SR-Site (from Joyce et al., 2010, Figure 3-6). The inner portion of the model is the detailed-scale DFN submodel around the repository tunnels, while the outer portion is the larger-scale ECPM submodel, with block properties derived by upscaling from the DFN representation. The site-scale HCDs are visible as linear patterns of elevated hydraulic conductivity (as indicated by the color scale at left).

For the Q1 path, which is the main path considered in the present analysis, the formula used is (SKB R-09-20, Eq. 3-7):

$$Q_{eq1} = \sum_f \left(\frac{Q_f}{\sqrt{a_f}} \sqrt{\frac{4 D_w t_{wf}}{\pi}}\right)$$

where Q_f is the volumetric flowrate in the fracture intersecting the deposition hole, a_f is the area of the intersecting fracture, D_w is the diffusivity in water, t_{wf} is the time that the water in a given fracture is in contact with the deposition hole, and the summation is over all intersecting fractures f.

The average equivalent flux for all fractures intersecting a given deposition hole is given by (SKB R-09-20, Eq. 3-8):

$$U_{r1} = \frac{1}{w_c} \sum_f \frac{Q_f}{\sqrt{a_f}}$$

where w_c is the deposition hole height (in SKB's calculations, a value of 5 m representing the canister height rather than the deposition hole height was used according to Joyce et al., 2010).

Travel time t_r and transport resistance F_r are calculated by an advective particle tracking method, in which non-reactive particles are assumed to move along with the local groundwater, at the same velocity, for each segment of a transport path from the source location to the biosphere.

The travel time through the DFN portion of the model is calculated as the sum of the time spent in each segment of a fracture:

$$t_{r(DFN)} = \sum_f \frac{e_{tf} w_f \delta l}{Q_f}$$

where δl is the step length along a path of f steps, each between a pair of fracture intersections and e_{tf} is the fracture aperture. The travel time through the ECPM part of the model is calculated analogously as:

$$t_{r(ECPM)} = \sum_l \frac{\phi_f \delta l}{q}$$

where ϕ_f is the porosity, δl is the step length along a path of l steps, and q is the local Darcy flux.

The transport resistance likewise is calculated by summing up the transport resistances for each segment of a transport path through the DFN:

$$F_{r(DFN)} = \sum_f \frac{2 w_f \delta l}{Q_f}$$

where w_f is the flow-path width, or through the ECPM:

$$F_{r(ECPM)} = \sum_l \frac{a_r \delta l}{q}$$

where a_r is the flow-wetted surface per unit volume of rock.

In the simulations by Joyce et al. (2010) and by Vidstrand et al. (2010), deposition holes are spaced uniformly along the deposition tunnels, without taking into account SKB's criteria for acceptance or rejection of deposition holes as described by Munier (2010). The criteria for deciding whether or not a hole should be excluded are (Joyce et al., 2010):

1. *Full perimeter criteria (FPC) – a deposition hole is excluded if it is intersected by the hypothetical extension of a fracture that intersects the full perimeter of the corresponding deposition tunnel.*
2. *Extended full perimeter criteria (EFPC) – a deposition hole is excluded if its full perimeter is intersected by a fracture that also intersects the full perimeter of four or more neighbouring deposition holes in the same deposition tunnel.*

Holes that would be rejected based on either of these criteria were not excluded in the flow or particle tracking calculations. However, these locations were identified in the data listing performance measures that were delivered by the flow modelers for SR-Site consequence assessment calculations.

2.1.2. Ranges of parameters estimated for temperate climate

Distributions of equivalent flux U_r and transport resistance F_r for SKB's base-case model for temperate conditions are presented graphically by Joyce et al. (2010). These plots are reproduced here in Figures 2 and 3.

For U_r, the values range from about $2x10^{-7}$ m/yr to nearly 0.01 m/yr (with higher values being of primary concern for engineered-barrier performance). The U_r values are barely sensitive to time of release.

For F_r, the values range from about 10^4 y/m to $2x10^8$ y/m (with lower values being of primary concern for engineered-barrier performance), if only the contribution from the DFN portion of the model is included ($F_{r(DFN)}$).

The F_r values are somewhat sensitive to time of release, with marginally higher values seen for release times after 5000 AD. As explained by Joyce et al. (2010), this is expected as shoreline retreat leads to more lateral particle trajectories, in turn leading to longer travel times in the rock, giving an increase in F_r. By comparing the upper and lower plots in Figure 3, it can be seen that the contribution of the ECPM portion of the model is negligible for release times from 2000 AD to 3000 AD.

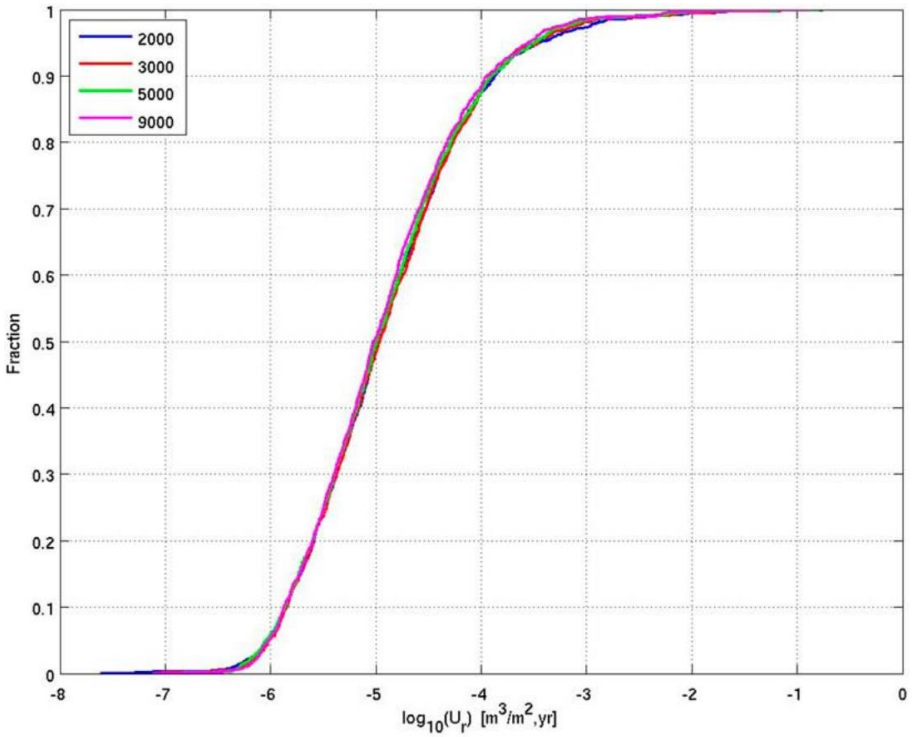

Figure 2: Cumulative distributions of the performance measure U_r for SKB's base-case groundwater flow model of temperate conditions (Joyce et al., 2010, Figure 6-8). Curves with different colors represent releases from the engineered barriers at 2000 AD, 3000 AD, 5000 AD and 9000 AD, according to the legend.

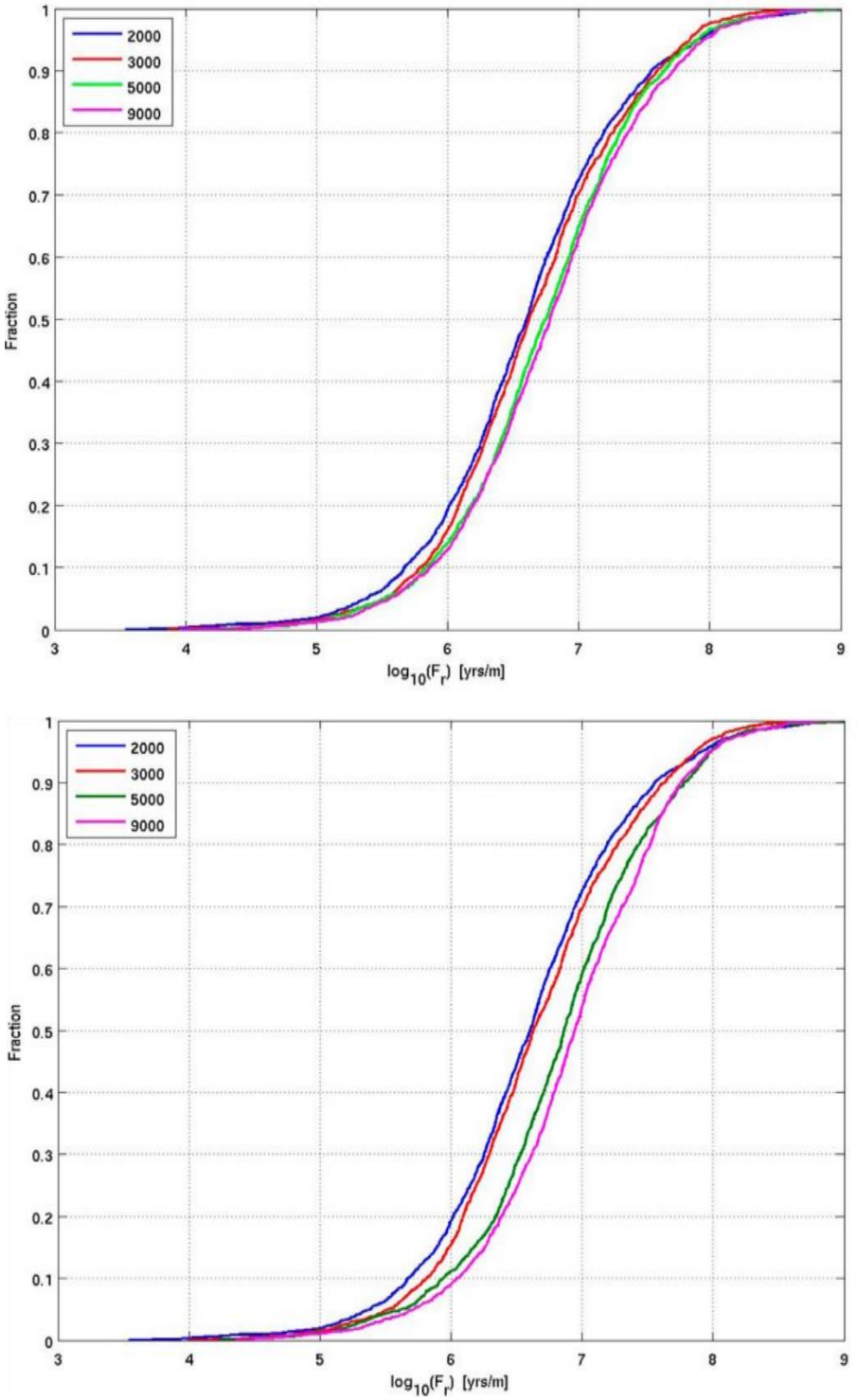

Figure 3: Cumulative distributions of the performance measures F_r for SKB's base-case groundwater flow model of temperate conditions (from Joyce et al., 2010, Figures 6-8 and 6-9). The upper plot shows F_r only from the DFN portion of the flow model ($F_{r(DFN)}$ in the notation used here). The lower plot includes the contribution from the ECPM and CPM parts of the model ($F_{r(DFN)} + F_{r(ECPM)}$). Curves with different colors represent releases from the engineered barriers at 2000 AD, 3000 AD, 5000 AD and 9000 AD, according to the legend.

The effect of screening out deposition hole locations that are intersected by large fractures, based on the FPC and EFPC criteria, is mainly to decrease the percentage of deposition holes that are connected to the far-field boundaries via the DFN (Figure 4). As noted by Joyce et al. (2010), the frequency of high-U_r deposition holes is also reduced, but there is less effect on the frequency of low-F_r deposition holes. From inspection of Figure 4, the range of U_r values is not reduced but the frequency of high values over 10^{-4} m/yr is reduced by about one half.

The statistical ranges of U_r, F_r, and t_r for SKB's hydrogeological base case model and for 10 stochastic realizations of the HCDs and HRDs are summarized as bar-and-whisker plots on Figure 5. The median values are fairly stable from one realisation to the next, within about half an order of magnitude. The high (95th percentile) values of U_r and the low (5th percentile) values of F_r and t_r show more variation.

According to Joyce et al. (2010) the extreme values seen for realisation r5 are associated with a single large, high-transmissivity fracture that intersects several tunnels and extends from the repository to the surface. They argue that such a feature would most likely be detected during repository construction, and would moreover have depth-dependent transmissivity that would moderate its effects.

Independent analysis in support of SSM's review (Geier, 2014) supports the first part of this argument, that such fractures would normally be detectable. The second part of this argument, however, depends on an inferred depth-transmissivity relationship which is not unequivocally supported by SKB's site data and analysis.

The effect of alternative size-transmissivity relationships in the DFN submodel was considered by Joyce et al. (2010). The base case referred to as “semi-correlated” (a log-linear relationship between fracture size and transmissivity, with a lognormal multiplicative noise term) is compared with a “correlated” model (perfect log-linear correlation between size and transmissivity) and an “uncorrelated” model (transmissivity sampled from a lognormal distribution, independent of fracture size).

The results are shown in Figure 6. Both in terms of high values of U_r and low values of F_r, it can be seen that the most significant of these three cases is the “correlated” case. According to Joyce et al. (2010, p. 102), the deposition holes with high U_r are thought to be associated with a few large stochastic fractures. For the (perfectly) correlated model, these large fractures will invariably have high transmissivities, compared with the semi-correlated and uncorrelated cases.

The deposition holes with low F_r are generally noted by Joyce et al. (2010) to be close to deterministic deformation zones (HCDs), but this does not explain the differences among the three cases. Joyce et al. (2010, p. 102) suggest that “[t]his may indicate more flow between the repository structures and the deformation zones in [the correlated and uncorrelated] cases.”

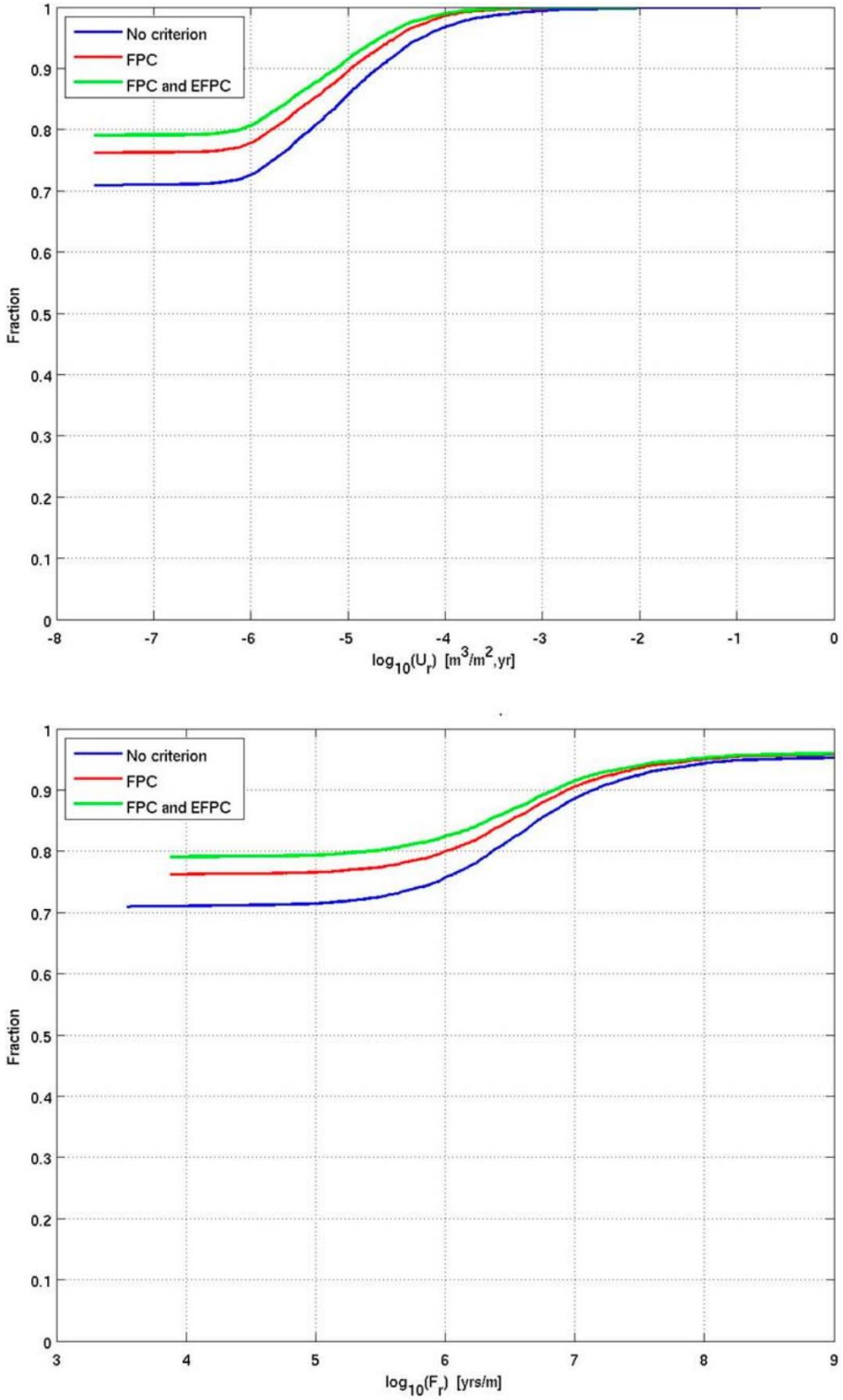

Figure 4: Effects on U_r and F_r of applying FPC and EFPC criteria for deposition holes, for SKB's base-case groundwater flow model of temperate conditions (from Joyce et al., 2010, Figure 6-15).

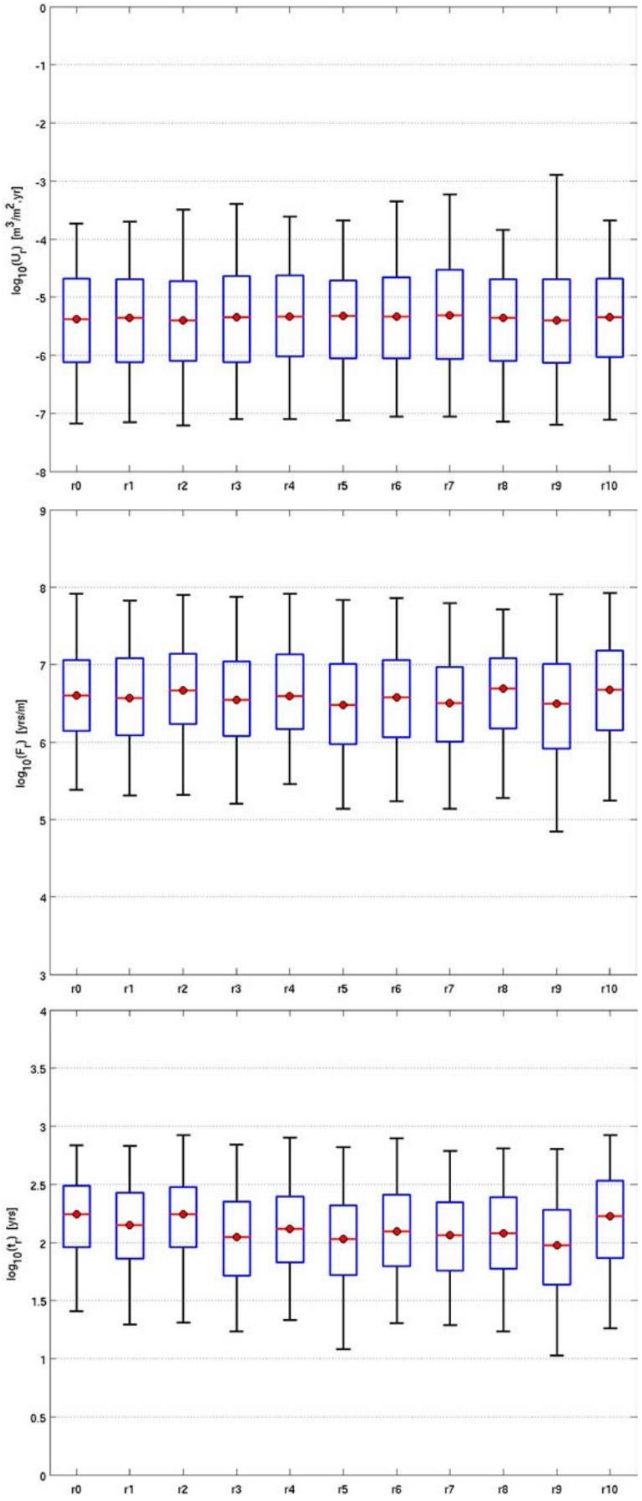

Figure 5: Bar and whisker plots of U_r (top), F_r (middle), and t_r (bottom) of stochastic variation in SKB's base-case groundwater flow model of temperate conditions (r0) and 10 stochastic realizations of the HCD and HRD (r1 to r10) for the Q1 particles that successfully started (28% to 31% of canister locations), released at 2000 AD. The statistical measures are the median (red), 25th and 75th percentiles (blue bar) and the 5th and 95th percentiles (black whiskers). From Joyce et al., 2010, Figure 6-18.

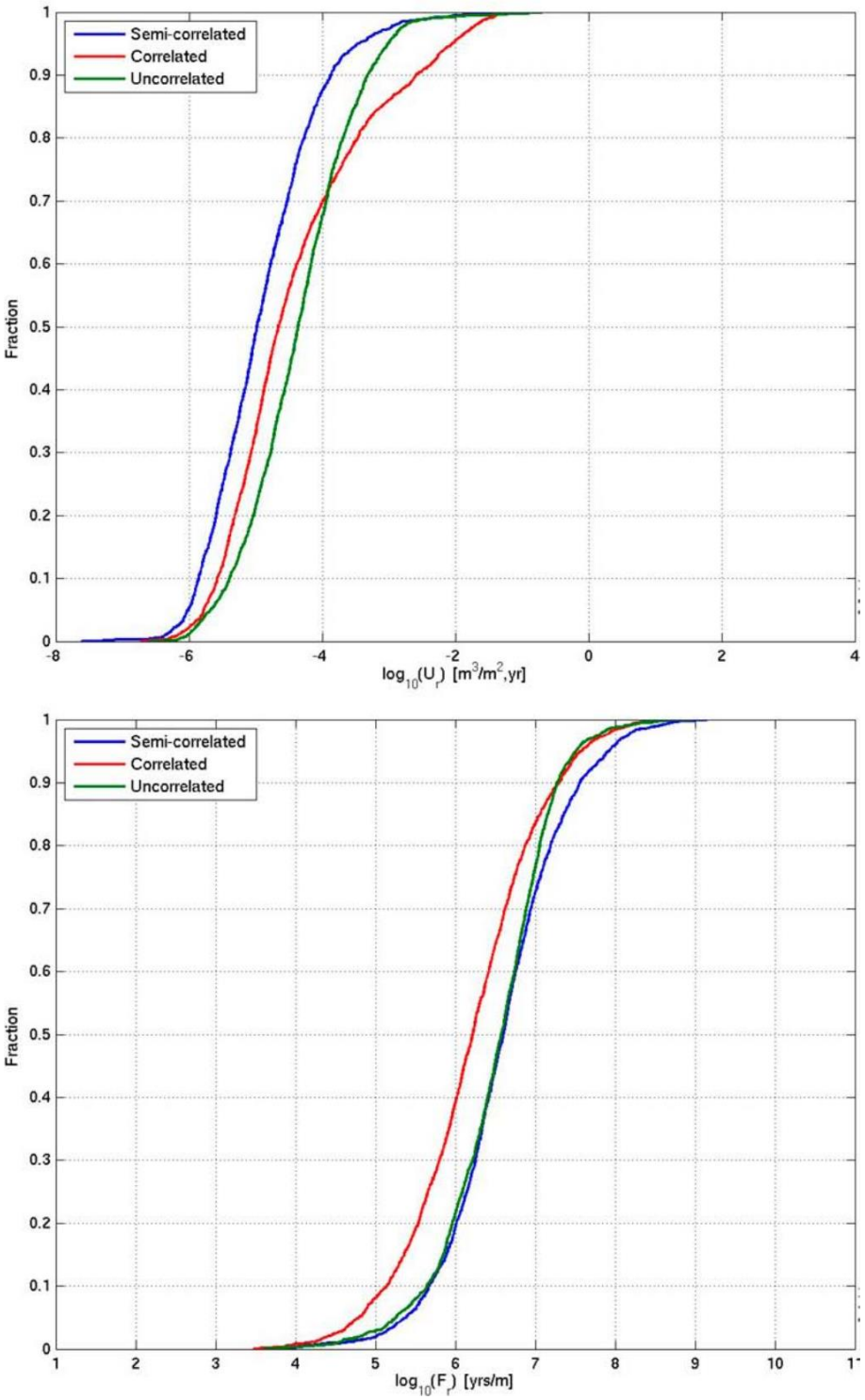

Figure 6: Influence of alternative models for the relationship of fracture transmissivity to fracture size (as indicated by the legend), for the performance measures U_r and F_r. From Joyce et al., 2010, Figure 6-28.

2.1.3. Ranges of parameters estimated for future climates

Performance measures for future climate situations were produced by Vidstrand et al. (2010), using an ECPM/CPM representation of the entire model domain. This simplified representation made it feasible to treat the more complicated physics of future permafrost and glacial situations, but resulted in a simplified treatment of flow paths through the fractured rock around the repository.

The hydraulic conductivities of ECPM blocks within the model were calculated based on a damage-tensor approach to upscaling (Vidstrand et al. refer to Svensson et al., 2010 for details), rather than network flow simulations. The method basically amounts to adding up an assumed contribution of each fracture considered as a separate entity, without considering network effects.

Figure 7 shows the effect in terms of Darcy flux q, for the ECPM representation used by Vidstrand et al. (2010) in comparison with the combination of DFN for the rock around the repository and ECPM based on more rigorous upscaling using a network-modeling approach for the surrounding portions of the model, as used by Joyce et al. (2010). The model of Vidstrand et al. has fewer extreme values of either low or high q. It also produces a noticeably bimodal distribution of q, evident from the steep slopes at around $\log_{10} q$ = -5.5 and $\log_{10} q$ = -3.7 [m/s], whereas the model of Joyce et al. produces a more broad, unimodal distribution of q. Vidstrand et al. do not comment on these differences, and simply state that "the results are in a reasonable agreement given the differences in flow concept and model scale."

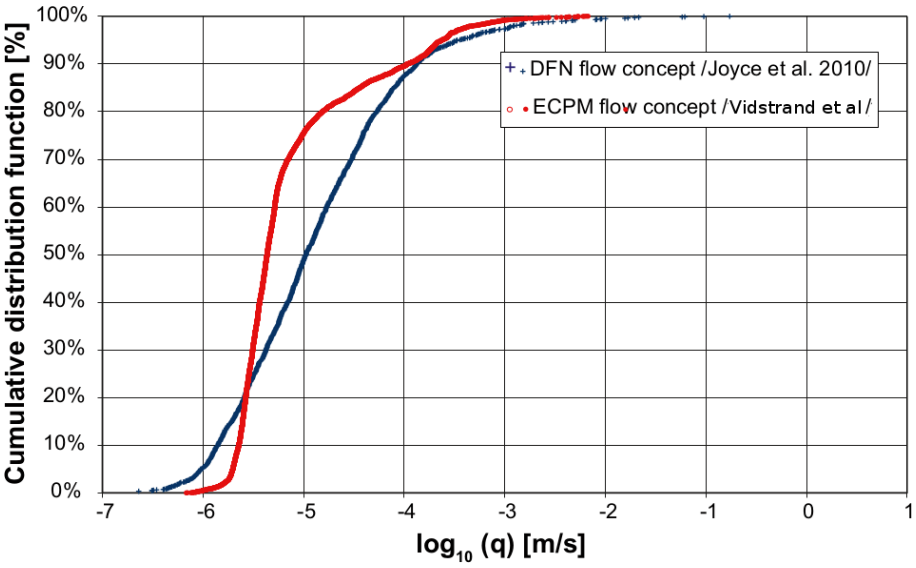

Figure 7: Effect of ECPM representation of Vidstrand et al. (2010) vs. DFN representation of Joyce et al. (2010), in terms of the cumulative distribution of Darcy flux q, for temperate climate conditions. The curve for the model of Joyce et al. only includes deposition hole positions for which particles reached the upper boundary of the model. Figure adapted from Vidstrand et al., 2010, Figure 6-1.

Values of block-scale kinematic porosity (which are needed to relate Darcy fluxes to travel times) are calculated by adding up the contributions of individual fractures for

a given block of the model; thus as for hydraulic conductivity, network effects on porosity are not taken into account. As a further simplification, according to Vidstrand et al. (2010, Appendix B) all stochastically generated fractures were assumed to have the same values of fracture thickness b_f and fracture kinematic porosity φ_f, resulting in a constant value of transport aperture for all fractures:

$$(e_t)_f = b_f \phi_f = (0.1\text{m})(0.001) = 10^{-4}\text{m}$$

based on the values listed in Table B-12 of Vidstrand et al. (2010). Vidstrand et al. do not comment on the consequences of these simplifications, but presumably they result in a much more uniform field of block-scale kinematic porosities than would be obtained from explicit DFN upscaling of a model with variable fracture apertures.

For calculating the transport resistance F_r, values of flow-wetted fracture surface area per unit volume of rock mass (a_r) need to be assumed for each block of the continuum model. Vidstrand et al. (2010, Table B-10) assumed a homogeneous value of a_r for each of three depth zones in each of of the six fracture domains FFM01–FFM06, based on median values upscaled from simulations of the DFN model by Joyce et al. (2010), based on upscaling from the DFN model.

For the regional scale outside of these fracture domains, homogeneous values were assumed to apply for a_r as well as for hydraulic conductivity and kinematic porosity (Vidstrand et al., 2010, Table B-11).

Vidstrand et al. (2010) evaluated performance measures for discharge paths by releasing particles from each of 6,916 deposition hole positions and from each of five measurement localities, ML 1–5. Particles were tracked for 100 years; not all of the released particles reach the ground surface within this period of time.

Reverse particle-tracking, using the same methods but reversing the groundwater velocity field, was also performed to obtain performance measures for recharge paths. All of the recharge paths identified by this method were found to originate from the model boundary (rather than the ground surface within the model area), according to Vidstrand et al. (2010, Appendix G).

The predicted evolution of Darcy flux in the repository during a future glaciation, based on the ECPM model of Vidstrand et al. (2010), is shown in Figure 8 (for a complete period of glacial advance and retreat), and in Figure 9 (for a detailed view of the initial period of glacial advance). The peak fluxes are predicted occur during the relatively short periods when the ice front is either advancing over, or retreating back over the repository site.

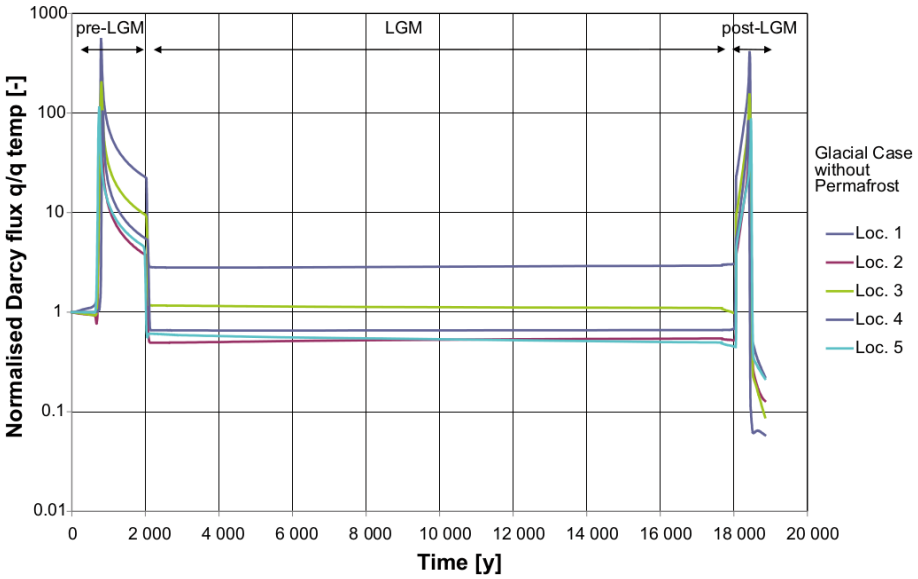

Figure 8: Plot (from Vidstrand et al., 2010, Figure 6-7) showing the evolution of Darcy flux (normalized as q/q_{temp}), at five locations denoted ML 1-5 during approximately 19,000 years for the glacial case without permafrost. ML 1 is located close to a steeply dipping deformation zone). The period labeled "pre-LGM" represents the time when the ice front is advancing over the Forsmark site, the period labeled "post-LGM" represents the time when the ice front is retreating back over the site, and the period labeled "LGM" represents the interim period when the continental glaciation is at maximum extent.

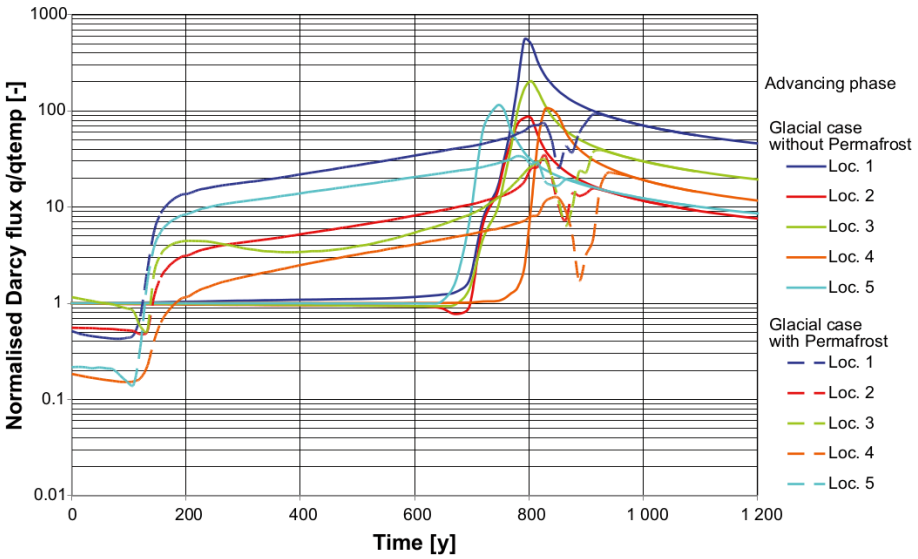

Figure 9: Plot (from Vidstrand et al., 2010, Figure 6-8) showing the detailed evolution of Darcy flux, (normalized as q/q_{temp}), at the same locations as in Figure 8, for the initial 1200 years spanning glacial advance, and showing the influence of different assumptions regarding permafrost. In addition to the glacial case with permafrost (solid lines), the evolution of the glacial case without permafrost (dashed lines) is shown. After approximately 1,000 years, the two scenarios are identical.

Vidstrand et al. note that the abrupt shift to low, constant values at the start of the period of complete ice coverage (labeled "LGM" in Figure 8) is an artefact of an instantaneous shift in ice sheet gradient which is applied as a boundary condition, at the same moment. A more smooth transition would be expected in reality. For the

glacial case with permafrost, slightly different flux evolution curves are obtained during glacial advance (Figure 9), but for subsequent periods the curves are identical to those shown in Figure 8, as there is no permafrost during these periods.

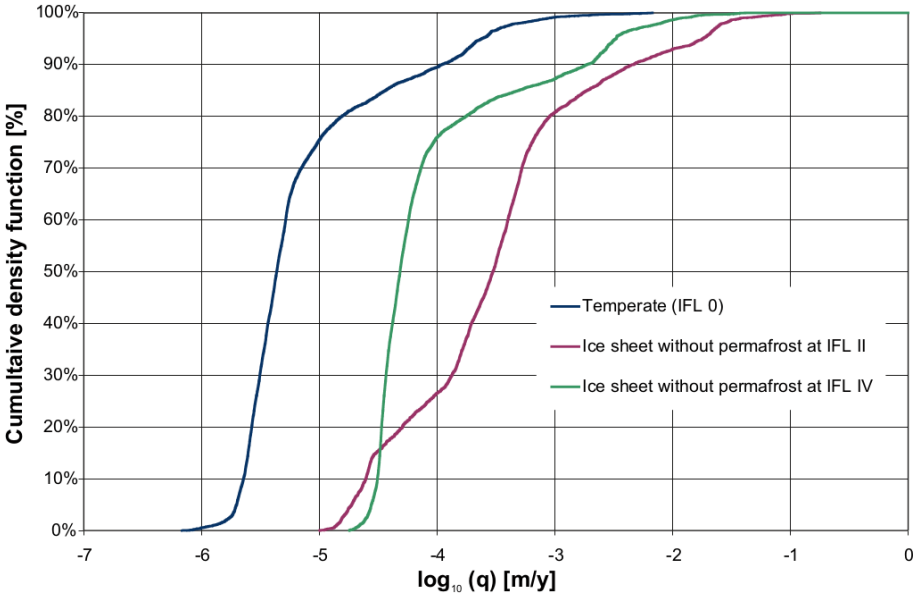

Figure 10: Comparison of cumulative distributions of Darcy flux between the temperate case (IFL 0) and two different positions of the ice sheet margin for the case of an ice sheet without permafrost (from Vidstrand et al., 2010, Figure 6-13).

From Figure 10 which compares the cumulative distribution of Darcy fluxes for temperate climate conditions with that for two different positions of an ice margin, it is seen that the median Darcy flux of is increased by 1.5 to 2 orders of magnitude when the ice sheet margin is at the positions denoted IFL IV and IFL II, respectively. Vidstrand et al. suggest that "the Darcy fluxes are more or less uniformly influenced by the glacial boundary conditions ... regions with low fluxes are equally affected by the high gradients induced by the ice sheet as regions with high fluxes." However they comment that this may be at least partly an artefact of the use of a continuum (ECPM) rather than discrete (DFN) representation of the sparsely fractured rock at repository depths.

The corresponding distributions of transport resistance F_r are shown in Figure 11. As noted by Vidstrand et al., the main effect of different ice front positions is a uniform shift of the cumulative distribution, by 1 to 2 orders of magnitude depending on the ice-front position.

Model variants that considered different directions of ice front movement and uniform changes in transmissivity of fractures had only minor effects on performance measures.

The performance measures predicted for future climates are summarized by Vidstrand et al. (2010) in terms of median values which are listed here in Table 1.

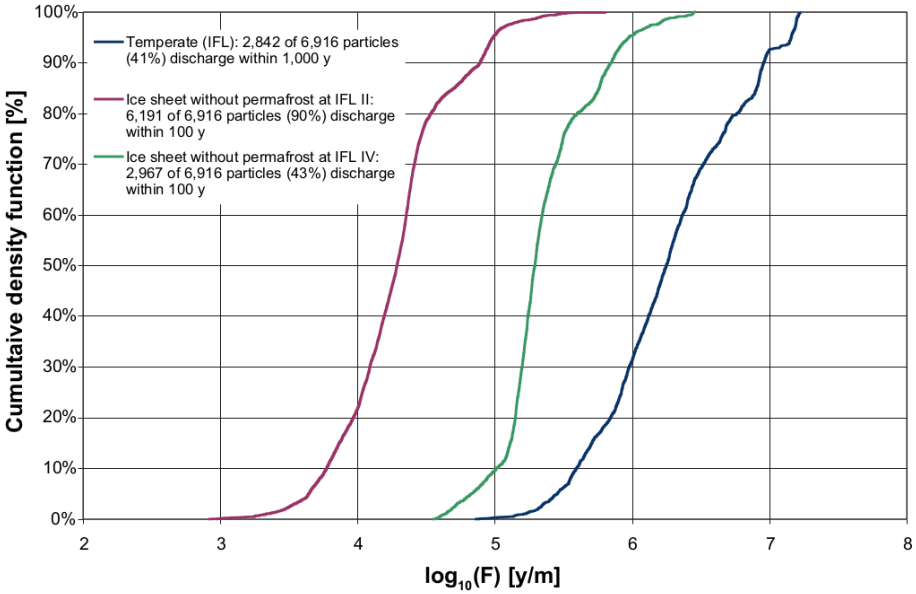

Figure 11: Comparison of cumulative distributions of transport resistance F_r between the temperate case (IFL 0) and two different positions of the ice sheet margin for the case of an ice sheet without permafrost (from Vidstrand et al., 2010, Figure 6-14).

Table 1: Median values of performance measures calculated for five different measurement locations (ML = 1-5), for the case of temperate climate and for two future glacial situations with an advancing ice front at position IFL II (Vidstrand et al., 2010, Tables 6-1, 6-2 and 6-3).

Case	ML	Discharge path length (m)	Travel time (y)	Transport resistance (y/m)	Recharge path length (m)	Travel time (y)	Transport resistance (y/m)
Temperate	1	602	11	$3.4x10^5$	3104	60	$1.8x10^6$
	2	3403	875	$8.4x10^6$	4570	330	$3.9x10^6$
	3	1918	380	$8.9x10^6$	2221	63	$1.0x10^6$
	4	1635	4	$4.4x10^4$	2338	38	$9.2x10^5$
	5	1198	361	$7.6x10^5$	2467	50	$1.4x10^6$
Glacial (no permafrost)	1	815	0.1	$2.8x10^3$	24896	159.5	$1.1x10^5$
	2	997	3.1	$2.4x10^4$	14737	137.4	$7.7x10^4$
	3	764	1.3	$1.0x10^4$	28414	9.9	$3.2x10^5$
	4	1505	2.9	$2.2x10^4$	31004	32	$9.3x10^5$
	5	2038	0.8	$1.2x10^4$	25831	40.5	$1.6x10^5$
Glacial (with permafrost)	1	13032	24	$7.0x10^5$	27876	40	$1.2x10^6$
	2	12155	36	$5.5x10^5$	28162	168	$2.9x10^6$
	3	9537	7	$1.7x10^5$	29859	287	$8.5x10^6$
	4	10580	25	$7.3x10^5$	30989	8	$2.6x10^5$
	5	6650	3	$4.3x10^4$	25410	31	$1.7x10^5$

The median transport resistances F_r for discharge paths and recharge paths are plotted in Figures 12 and 13, respectively.

For discharge paths (Figure 12), the median F_r for the glacial case with no permafrost is reduced up to three orders of magnitude relative to the temperate case, depending on source location.

When permafrost is present in the model for glacial conditions, the median F_r is generally higher than for the glacial case with no permafrost. For some measurement locations, F_r for the glacial case with permafrost can even be higher than for the temperate case, apparently because permafrost leads to very long discharge path lengths, on the order of tens of kilometers (as can be seen from Table 1).

For recharge paths (Figure 13), there is less difference between the temperate case and the two glacial cases, and between the two glacial cases with and without permafrost. From Table 1 it can be seen that recharge path lengths and travel times are of similar magnitude for both of the glacial cases, regardless of whether permafrost is included in the model.

In the temperate case, the recharge path lengths are shorter by about an order of magnitude compared with the glacial cases. Apparently this helps to offset the much higher pressure differences that drive flows in the glacial cases.

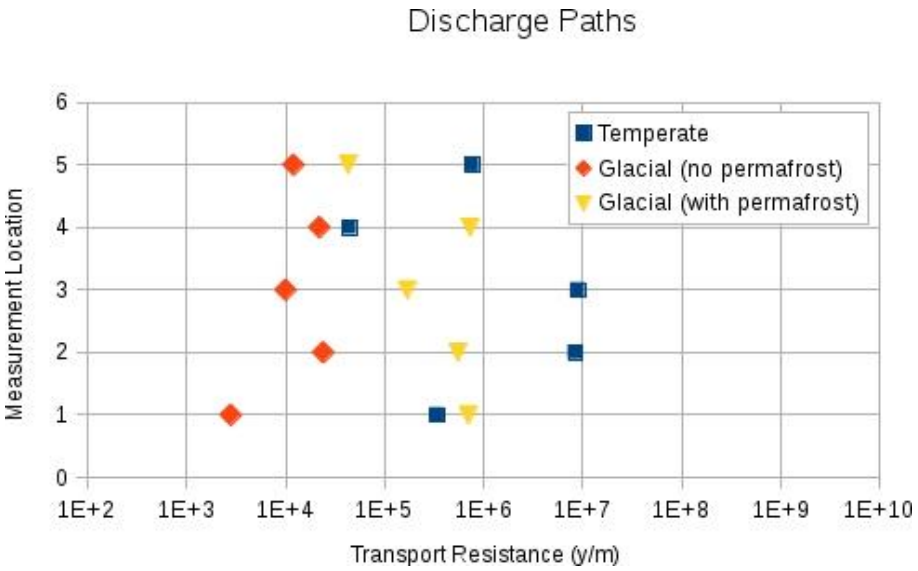

Figure 12: Median values of transport resistance F_r as calculated for the ensemble of discharge flow paths originating from five different measurement locations (ML = 1-5), for the case of temperate climate and for two future glacial situations with an advancing ice front at position IFL II (based on Vidstrand et al., 2010, Tables 6-1, 6-2 and 6-3).

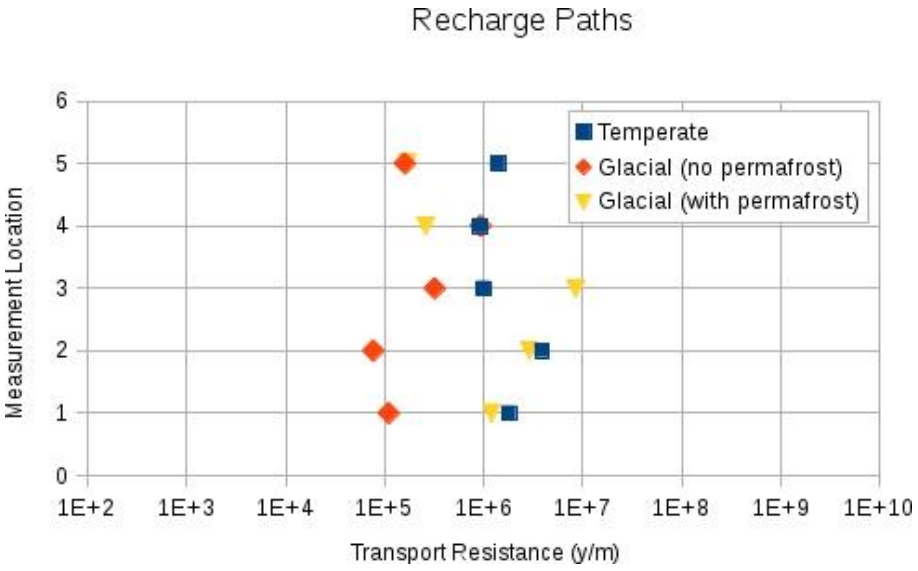

Figure 13: Median values of transport resistance F_r as calculated for the ensemble of recharge flow paths extending from the surface or model boundaries to five different measurement locations (ML = 1-5), for the case of temperate climate and for two future glacial situations with an advancing ice front at position IFL II (based on Vidstrand et al., 2010, Tables 6-1, 6-2 and 6-3).

2.2. Motivation of the assessment

The performance parameters calculated from groundwater flow models are a key input to SKB's consequence analysis calculations for SR-Site. The flowrate or equivalent flux to deposition holes is a key factor entering into calculations of buffer erosion and canister corrosion. The transport resistance F_r is a dominant parameter governing the far-field geosphere's influence on release of sorbing radionuclides to the biosphere. In addition to being used for this purpose, F_r values from groundwater flow models have also been used by SKB to evaluate penetration of dilute glacial meltwaters to deposition holes, and thus are important for evaluating whether conditions that would allow chemical erosion of the buffer are likely to occur in the near field.

While SKB's groundwater flow models can fairly be described as “state-of-the-art” for assessment of flow in sparsely fractured crystalline rock, the models are highly complex and difficult to evaluate from a regulatory perspective. The regional-scale and site-scale models depend at least in part on upscaling from a DFN model to a equivalent porous-medium representation, which introduces significant theoretical uncertainties that have been only partly addressed.

SKB's presentation is largely graphical, and only limited intermediate results have been presented in terms of the predicted head/pressure gradients and flow fields. The way in which uncertainties in the DFN model propagate are sometimes difficult to interpret from the end results.

Therefore comparisons with a simpler and a more transparent method of evaluating the performance measures are desirable from a review perspective. This assessment has included the development and application of a simple model that provides reasonably conservative estimates of the performance measures, and gives insights into the consequences of uncertainties in the DFN model.

2.3. Independent assessment of parameter ranges

The approach to estimating far-field performance parameters makes use of results from calculations of the number of critical fracture positions in the repository. The main steps that are utilized for the present calculations are as described by Geier (2014):

(1) Stochastic simulation of the fracture population in the vicinity of the proposed repository,
(2) Simulation of the adaptive placement of deposition holes within the repository layout, and
(3) Identification of intersections between fractures and deposition holes

The fracture/deposition-hole intersections identified in the third step are used in the present calculations as the potential starting points for transport paths that connect from these deposition holes to the nearest hydrogeological deformation zone (HCD) that discharges to the biosphere.

2.3.1. Methodology

The main steps in the present calculations are:

(1) Identification (by random selection) of fracture/deposition hole intersections to treat as the starting points of transport paths,
(2) Deterministic calculation of transport-path segment lengths for each transport path,
(3) Calculation of segment transmissivities as a deterministic or stochastic function of the segment length,
(4) Calculation of segment transport apertures based on a given deterministic or stochastic correlation to transmissivity,
(5) Estimation of the hydraulic head differential between the deposition-hole location and the nearest discharging HCD, and
(6) Calculation of the resulting performance-assessment parameters u_r, t_r, F_r, and L_r.

Details are described in the following subsections.

Identification of starting points of transport paths

The calculations treat the repository as consisting of a single section, characterized by the statistics of the fracture domain FFM01. The Forsmark Site Descriptive Model (SKB, 2008) considers fracture domain FFM06 to be statistically identical to FFM01 at repository depth, so the part of the repository within FFM06 is treated together with that in FFM01.

The linear frequency (per length of deposition hole) $P_{10,trans}$ of transport paths connecting from deposition holes to the ensemble of discharging HCDs is defined as:

$$P_{10,trans} = \frac{N_{trans}}{L_{dh} N_{dh}}$$

where N_{trans} is the expected number of transport paths in the repository section, L_{dh} is the deposition hole length (7.83 m), and N_{dh} is the number of deposition holes in the repository section.

$P_{10,trans}$ is assumed to be equal to $P_{10,PFL,corr}$, the total linear frequency of flowing features (PFL-f) identified by the Posiva Flow Log from deep core-drilled holes. The values used are for the rock below z = -400 m.

- FFM01: $P_{10,PFL,corr}$ = 0.005 m^{-1} (SKB R-08-23, Table 3-4);
- FFM03: $P_{10,PFL,corr}$ = 0.05 m^{-1} (SKB R-08-23, Table 3-6).

Starting points for transport paths are chosen at random from the set of fracture/deposition-hole intersections for a full repository layout, adapted to simulations of the Geo-DFN model for the site according to SKB's FPC and EFPC criteria. 10 realizations of repository layouts based on the Geo-DFN model are considered, each giving rise to a separate set of transport paths.

The Geo-DFN simulations only consider fractures radius larger than 3.5 m. These calculations do not take into account deposition holes that could be connected via a tunnel EDZ, or are connected only via very low-T fractures that would be below the PFL detection limit. Such deposition holes would be unlikely to experience significant buffer erosion or canister corrosion (according to SKB's models of those processes).

A given fracture-deposition hole intersection $\boldsymbol{X}$ is assumed to have a uniform probability p_c of connecting to the nearest discharging HCD.

Two different assumptions are considered regarding this probability, length-based scaling and area-based scaling, as detailed in the following paragraphs.

Length-based scaling

Under this assumption, the frequency of transport paths per unit length of deposition hole, $P_{10,trans}$, is assumed to be equal to the linear frequency of PFL anomalies that were encountered in the same fracture domain in deep boreholes:

$$P_{10,trans} = P_{10,PFL,corr}$$

This would be expected for a system in which the portions of PFL-anomaly fractures that carry significant flow are wide in relation to the diameters of both the boreholes and the deposition holes. In such a situation, the expected number of transport paths that intersect deposition holes is:

$$N_{trans} = P_{10,trans} L_{dh} N_{dh} = P_{10,PFL,corr} L_{dh} N_{dh}$$

so the length-scaled probability of a given fracture/deposition-hole intersection being part of a transport path is:

$$p_{cL} = \frac{N_{trans}}{N_X} = \frac{P_{10,PFL,corr} L_{dh} N_{dh}}{N_X}$$

where N_X is the total number of fracture/deposition-hole intersections in the repository section considered.

Area-based scaling

In a strongly channelized fracture flow system where, within a given fracture, flow tends to be concentrated in channels of finite width, the length-based scaling assumption might not be conservative. If the typical flow-channel width is small relative to the deposition-hole diameter, then the probability of intersecting a given flow channel scales in proportional to the vertical cross-sectional area of the deposition holes vs. the boreholes, rather than just the length.

In the bounding situation where flow channels are effectively point flows, the frequency of transport paths that intersect deposition holes, per unit length of deposition hole, is related to the linear frequency in deep boreholes as:

$$P_{10,trans} = P_{10,PFL,corr} \frac{r_{dh}}{r_{bh}}$$

where r_{dh} is the deposition-hole radius and r_{bh} is the nominal radius of boreholes at repository depth.

In this bounding case, the area-scaled probability of a given fracture/deposition-hole intersection being part of a transport path is:

$$p_{cA} = \frac{N_{trans}}{N_X} = \frac{P_{10,PFL,corr} L_{dh} N_{dh}}{N_X} \cdot \frac{r_{dh}}{r_{bh}}$$

In practice, p_{cA} often exceeds 1, leading to the result that all fracture/deposition-hole intersections ***X*** are treated as transmissive intersections.

Calculation of transport-path segment lengths

Transport paths are assumed to consist of the minimum number and length of fracture segments that are necessary to connect to the nearest point on the closest discharging HCD, subject to the constraints:

> (1) The first segment of the path is the fracture that intersects the deposition hole, with length equal to the fracture radius,
> (2) The second segment (and third, fourth, etc. segments if needed) are assumed to be of length equal to the remaining distance to the HCD, or the maximum fracture radius (whichever is less).

The distance to the nearest hydrogeological deformation zone is calculated using the following module of the DFM software:

> *pancalc* (version 2.4.1.1, executable pancalc2411 compiled February 17, 2014)

The distance calculations are carried out by the same method as was used in similar calculations to identify critical fracture intersections by Geier (2014), but here a different set of deformation zones are considered (deformation zones which act as discharging HCDs according to SKB's site-scale flow model, rather than deformation zones that are considered to be potentially seismically unstable.

The main assumptions introduced by the constraints listed above are:

- The radius of the fracture that intersects the deposition hole is a reasonable upper-bound estimate of the length of the connection from the deposition hole to the nearest fracture that connects to the larger-scale hydraulic network.

- Stochastic fractures (or minor deformation zones) are not larger than the 1000 m scale estimated by SKB.

- The transport path is directly to the nearest point on the nearest discharging HCD, with negligible tortuosity.

The first assumption (if SKB's Hydro-DFN model is assumed to be valid) is reasonably conservative, because in most cases this first segment is the shortest segment of the pathway, and hence (for the typical case where fracture transmissivity is positively correlated to fracture size) this will be the lowest-transmissivity segment, which accounts for the major part of the transport time through the rock t_r and the corresponding transport resistance F_r.

A more strictly conservative assumption would be to assume that the length of the first segment is negligible, so this first fracture does not contribute significantly to either t_r or F_r. However, such a conservative assumption is not realistic as SKB's criteria for deposition-hole acceptance require that the initial segment of a transport path will be via a relatively small-radius fracture, in most cases.

An intermediate assumption (more conservative than the first assumption, but more realistic than neglecting the first segment) would be to assume that the initial segment extends for just a short distance, less than the fracture radius, before connecting to the large-scale network. However, such an assumption may still be excessively conservative in view of the long mixing lengths inferred from experiments in similar geological media (Black et al., 2007).

The second assumption (that stochastic fractures forming the second and subsequent segments of a transport path are not larger than 1000 m in extent) hinges upon the question of whether SKB's site investigations have really managed to exclude larger fractures or minor deformation zones.

An alternative and more conservative assumption would be that the second segment of a transport path always connects directly to the nearest discharging HCD. This would be inconsistent with SKB's site descriptive model, but arguably has not been excluded by the site investigations. Such an assumption could easily be considered in the present approach, if more conservative estimates are needed.

The third assumption of a direct path is purely conservative. Any alternative assumption of greater tortuosity would require a longer transport-path length L_r and would give rise to higher values of t_r and F_r. Arguably some higher degree of tortuosity would be more realistic. Alternative assumptions for tortuosity could be considered within this approach, but it is expected that the effects on transport-path parameters would be less than an order of magnitude.

Calculation of segment transmissivities

Transport-path segment transmissivities T are calculated based on a specified deterministic or stochastic correlation to equivalent fracture radius r, depending on the SKB model variant considered. The three variants considered are the fully correlated model (in which case T is deterministically related to r), the semi-correlated model (in which case T is logarithmically correlated to r), and the uncorrelated model (in which case T varies independently of r) are considered as separate calculation cases. All of these can be expressed in the general form of the semi-correlated model:

$$T = ar^b 10^{\sigma N(0,1)}$$

where a, b, and σ are empirical parameters and $N(0,1)$ is a random value from the standard normal (Gaussian) distribution with zero mean and unit standard deviation.

For the case of the (perfectly) correlated model, $\sigma = 0$ so this reduces to:

$$T = ar^b$$

For the case of the uncorrelated model, $b = 0$ so the general form reduces to:

$$T = a \cdot 10^{\sigma N(0,1)}$$

or alternatively (in the form used by SKB):

$$T = 10^{\mu+\sigma N(0,1)}$$

where $\mu = \log_{10}(a)$, so $a = 10^{\mu}$.

The values of these parameters for fracture domains FFM01 and FFM03, for the depth zone $z < -400$ m, are listed in Table 2. Note that the values for FFM01 are used for fracture domain FFM06 according to SKB's interpretation. The parameter values for fracture domain FFM03 have not been used in the present computations, as this fracture domain is not encountered within the repository layout. However the possibility to model this domain as an alternative has been included in the AWK script *Tmodels_skb.awk* which implements these models (Appendix 2).

Table 2: Parameters of segment transmissivity models for Fracture Domains FFM01 and FFM03 in depth zones z < -400 m, based on Tables 6-75 and 6-77 of SKB TR-10-52 and using the formula $a = 10^{\mu}$ to convert from the values given in the case of the uncorrelated model. Parameter values in bold font are those listed in the specified tables in SKB TR-10-52. Parameter values in normal font are inferred based on the equations given above.

Fracture Domain	Case	a (m^2/s)	$\log_{10} a$	b (-)	σ (-)
FFM01	semi-correlated	**5.3×10^{-11}**	-10.3	**0.5**	**1.0**
	correlated	**1.8×10^{-10}**	-9.7	**0.5**	0
	uncorrelated	1.58×10^{-9}	**-8.8**	0	**1.0**
FFM03	semi-correlated	**1.8×10^{-8}**	-7.7	**0.3**	**0.5**
	correlated	**7.1×10^{-9}**	-8.1	**0.6**	0
	uncorrelated	$6.3.\times10^{-8}$	**-7.2**	0	**0.8**

Calculation of segment transport apertures

Transport-path segment apertures b_T are calculated based on specified correlations to transmissivity T, depending on the SKB model variant considered. Four variants have been considered in the present calculations (b_T expressed in units of m and T in units of m2/s, in all cases):

Äspö Task Force model (Dershowitz et al., 2003):

$$b_T = 0.5T^{0.5}$$

Stochastic variant of Äspö Task Force model

Stochastic model based on Äspö Task Force model but with a half-order-magnitude standard deviation:

$$b_T = 0.5T^{0.5}10^{0.5N(0,1)}$$

Hjerne model (Hjerne et al., 2010):

$$b_T = 0.28T^{0.3}$$

Cubic law:

$$b_T = \sqrt[3]{\frac{12\mu_w T}{\rho_w g}}$$

where μ_w is the dynamic viscosity of water, ρ_w is the density of water, and g is gravitational acceleration.

The cubic-law model can be written in the same form as the preceding aperture models as:

$$b_T = cT^{1/3}$$

where:

$$c = \sqrt[3]{\frac{12\mu_w}{\rho_w g}}$$

Using rough values of μ_w = 1 cP (0.001 Pa s), ρ_w = 1000 kg/m^3 and g = 9.81 m/s^2 gives c ≈ 0.0106 m$^{1/3}$s$^{1/3}$.

Figure 6-66 of TR-10-52 shows a value of c = 0.0117 (units not stated but presumably m$^{1/3}$s$^{1/3}$). This value was calculated by Hjerne et al. (2010, p. 17) based on a viscosity value μ_w = 1.3 cP for water at 10°C.

These four models – Äspö Task Force model and its stochastic variant, the Hjerne model, and the cubic-law model – are implemented in the AWK script *aperture_models.awk* (Appendix 2).

Estimation of hydraulic head differentials

The hydraulic head differential Δh between the deposition-hole location and the nearest discharging HCD is conservatively assessed as the maximum hydraulic head observed within the repository in SKB's hydraulic simulations, minus atmospheric head. This is equivalent to assuming that the HCDs provide no resistance to flow.

The value used for all of the simulations described in this report is Δh = 2 m. This is viewed as moderately pessimistic. A hydraulic gradient of 0.01 m/m gives Δh = 2 m for a transport distance of 200 m. The upper end of the Δh range within the repository horizon as calculated by a discrete-feature model (Geier, 2010) was slightly higher than 1 m, for a model that did not account for the effects of groundwater density variations. Gradients presented for a single discharge pathway at Forsmark as calculated by SKB (Figure 14) were typically around 0.001 m/m.

A less conservative and more realistic assumption would be to use actual values of hydraulic heads as calculated by SKB for different parts of the repository, and/or actual values of heads as calculated by SKB for the HCDs in the repository horizon. This is feasible to evaluate within the present approach. However, the difference is expected to be less than an order of magnitude in terms of transport times and transport resistances.

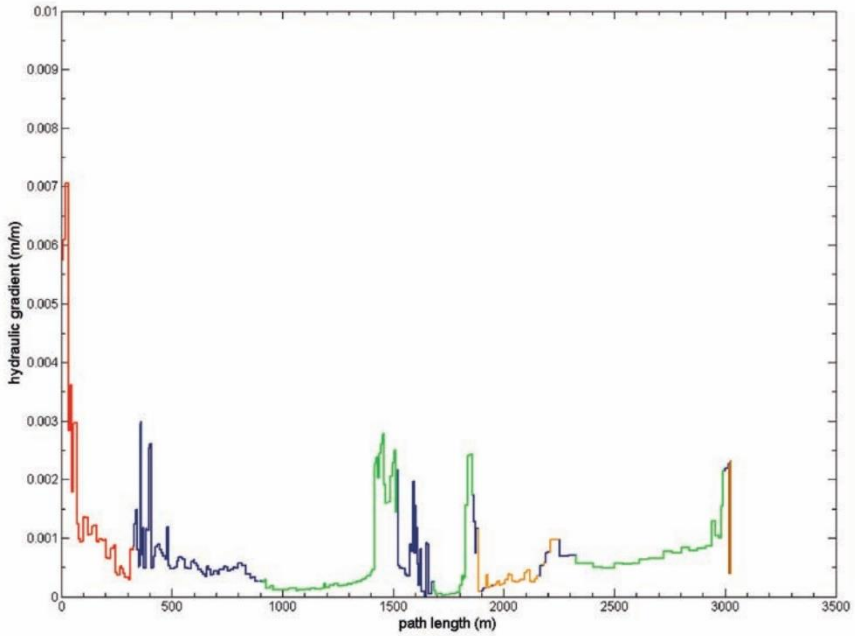

Figure 14: Hydraulic gradients encountered by a single particle representing solute along a calculated discharge flow path in an equivalent-continuum porous medium hydrogeological model for Forsmark (from SKB TR-08-05, Figure 8-62). The different colors represent different structural elements encountered by the particle along the discharge path.

Calculation of performance-assessment parameters

The performance-assessment parameters u_r, t_r, F_r, and L_r are calculated based on the assumption that the transport path segments are effectively in series, and of uniform width. Conceptually the transport path segments can be thought of as transmissive channels within more equidimensional fractures (Figure 15).

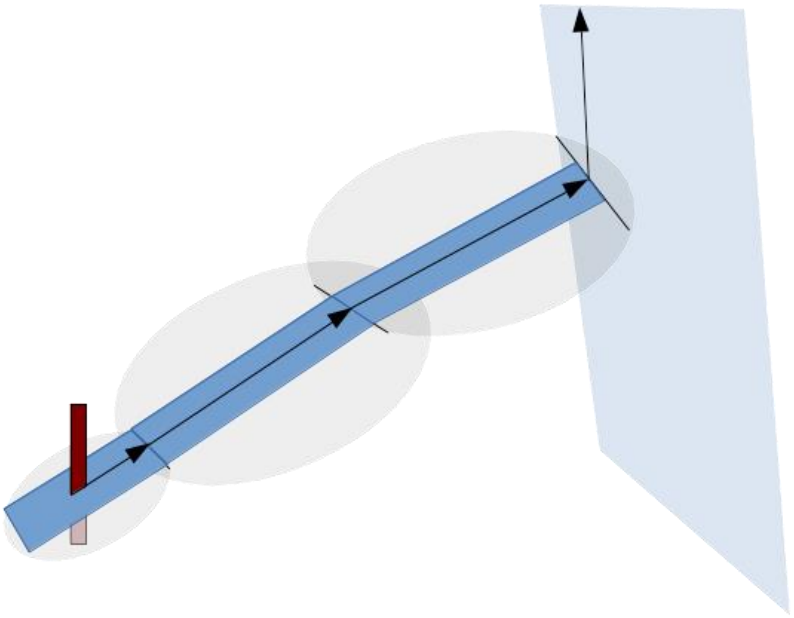

Figure 15: Conceptual illustration of transport path segments as channels of constant width in a series of three fractures connecting from a deposition hole to the nearest hydraulically conductive deformation zone. The arrows indicate the direction of transport.

The flux density (flowrate per unit width of fracture or channel) is calculated as:

$$q = -T_{eq}\frac{\Delta h}{L_r}$$

where T_{eq} is the equivalent transmissivity of the series of segments *i* (here making use of the assumption of equal segment width):

$$T_{eq} = \frac{L_r}{\sum_i L_i/T_i}$$

and L_r is the total length of the path:

$$L_r = \sum_i L_i$$

where L_i and T_i are respectively the length and transmissivity of the *i*th segment. Note that the flux density has the same units [L^2/T] as transmissivity and should not be confused with Darcy velocity (which has units of velocity, i.e. L/T).

The advective velocity within the *i*th segment is:

$$u_i = q/b_{T_i}$$

where b_{T_i} is the transport aperture of the *i*th segment. The incremental advective transport time through the segment is:

$$t_i = L_i/u_i$$

The total advective transport time through the rock for a given path is:

$$t_r = \sum_i t_i = \sum_i L_i / u_i$$

and the mean advective transport velocity is:

$$u_r = L_r / t_r$$

where L_r is the total length of the path. The transport resistance is calculated as:

$$F_r = \sum_i \frac{2L_i}{b_{T_i} u_i}$$

The average equivalent flux for all fractures intersecting a given deposition hole according to SKB R-09-20, Eq. 3-8, is:

$$U_0 = U_{r1} = \frac{1}{w_c} \sum_f \frac{Q_f}{\sqrt{a_f}}$$

where w_c = 5 m (the nominal canister length used in these calculations by SKB), a_f is the area of the intersecting fracture, Q_f is the volumetric flowrate in the fracture intersecting the deposition hole, and the summation is over all intersecting fractures. $Q_f / \sqrt{a_f}$ is effectively the flux density q for SKB's models in which flow is considered to take place across the full width $\sqrt{a_f}$ of the intersecting fracture. Hence in the present simple model, U_0 is calculated as:

$$U_0 = \frac{1}{w_c} \sum_f q_f = \frac{1}{w_c} \sum_f u_{0_f} b_{T_f}$$

where u_{0_f} is the advective velocity in the fth intersecting fracture where this intersects the deposition hole, and b_{t_f} is the corresponding transport aperture. For the simplest case where there is just one intersecting, flowing fracture with advective velocity u_0 and transport aperture b_T, this reduces to:

$$U_0 = \frac{1}{w_c} u_0 b_T$$

With this interpretation it can be noted that U_0 is not directly dependent on the size of the fracture that intersects a given deposition hole, but only on its aperture. However, there is an indirect dependence for model variants in which fracture transmissivity (and hence both aperture and advective flux) are positively correlated to fracture size.

The assumption of uniform segment width comparable to the width in the first intersecting feature (which is utilized in calculating the effective transmissivity for a series of fractures) can be viewed as reasonably conservative. With the stated assumptions of this simple model, typically the first fracture that intersects the deposition hole will be the narrowest part of the path. Especially for the model variants that assume a positive logarithmic correlation of fracture transmissivity to fracture size (i.e. the correlated and semi-correlated variants), this first fracture will have the highest resistance to flow, and hence will tend to control the total flowrate through the series of segments.

For a pathway that consists of multiple segments, this amounts to an assumption that the volumetric flowrate that passes through a deposition hole does not spread out as it encounters larger fractures. This is conservative with respect to the total advective transport time t_r and transport resistance F_r.

Whether this conservatism is "reasonable" or "excessive" depends in part on the conceptual view of flow and transport through fractured rock. In a typical discrete-fracture-network composed of equidimensional fractures in which transmissivity is uniform throughout a given fracture plane, this might be viewed as overly conservative. However, in a channelized fracture network, the assumption of nominally constant channel width could be viewed as reasonable.

2.3.2. Calculation cases

Selection of fracture statistical model variants

The following Geo-DFN alternatives were developed in the course of SKB's site descriptive modelling of the Forsmark side, to assess uncertainty in the statistical models for fracture size in relation to fracture intensity (Fox et al., 2007):

- r_0-fixed alternative
- OSM + TFM alternative
- TCM alternative ("k_r-fixed")

Discrete-fracture network (DFN) simulations of these three Geo-DFN alternatives for fracture domains FFM01 and FFM06 at repository depths were available from previous calculations (Geier, 2014). Those simulations considered both a "base case" that used SKB's estimates of fracture intensity, and an "elevated-P_{32}" variant in which the values of fracture intensity for each fracture set were increased uniformly by 25%, to scope uncertainty in this parameter.

For the present calculations of performance parameters using the series model, only the base case is propagated for each alternative:

- r_0-fixed alternative, base case (DFN calculation case r3)
- OSM + TFM alternative, base case (DFN calculation case o3)
- TCM alternative, base case (DFN calculation case t2)

For the simplified series-conductor model applied here, the elevated-P_{32} variants would not be expected to affect the probability distributions of the performance parameters. The only expected effect would be to increase the number of deposition holes affected, in direct proportion to the increase in P_{32}. Therefore the elevated-P_{32} variants are not evaluated numerically, as their consequences can be estimated by a simple scaling calculation.

For each of the three Geo-DFN alternatives, 10 realizations of the base case variants (DFN calculation cases r3, o3, and t2) are available from the previous calculations (Geier, 2014).

Calculation cases for series model

The r_0-fixed alternative is treated as the main case for evaluation of performance parameters, while the other two alternatives (OSM + TFM and TCM) are used to evaluate the effect of uncertainty in the Geo-DFN model. The calculation cases evaluated are summarized in Table 3. For each calculation case, all 10 realizations of the DFN model were evaluated.

Table 3: Summary of calculation cases evaluated.

Calculation case ID	Geo-DFN Alternative	Relationship between fracture size and transmissivity	Relationship between fracture transmissivity and aperture	Scaling	Random seed value
semiaspo1	r0-fixed (r3)	semi-correlated	base case	Linear	1
semiaspo2	r0-fixed (r3)	semi-correlated	base case	Linear	2
semiaspo1a	r0-fixed (r3)	semi-correlated	base case	Area	1
semiaspo2a	r0-fixed (r3)	semi-correlated	base case	Area	2
semistoch1	r0-fixed (r3)	semi-correlated	stochastic	Linear	1
semistoch1a	r0-fixed (r3)	semi-correlated	stochastic	Area	1
semihjerne1	r0-fixed (r3)	semi-correlated	Hjerne	Linear	1
semihjerne1a	r0-fixed (r3)	semi-correlated	Hjerne	Area	1
semicubic1	r0-fixed (r3)	semi-correlated	cubic law	Linear	1
semicubic1a	r0-fixed (r3)	semi-correlated	cubic law	Area	1
corraspo1	r0-fixed (r3)	correlated	base case	Linear	1
corraspo1a	r0-fixed (r3)	correlated	base case	Area	1
uncoaspo1	r0-fixed (r3)	uncorrelated	base case	Linear	1
uncoaspo1a	r0-fixed (r3)	uncorrelated	base case	Area	1
uncohjerne1	r0-fixed (r3)	uncorrelated	Hjerne	Linear	1
uncohjerne1a	r0-fixed (r3)	uncorrelated	Hjerne	Area	1
o3semiaspo1	OSM-TFM	semi-correlated	base case	Linear	1
o3semiaspo1a	OSM-TFM	semi-correlated	base case	Area	1
o3uncohjerne1	OSM-TFM	semi-correlated	Hjerne	Linear	1
o3uncohjerne1a	OSM-TFM	semi-correlated	Hjerne	Area	1
t2semiaspo1	TCM	semi-correlated	base case	Linear	1
t2semiaspo1a	TCM	semi-correlated	base case	Area	1
t2uncohjerne1	TCM	semi-correlated	Hjerne	Linear	1
t2uncohjerne1a	TCM	semi-correlated	Hjerne	Area	1

In initial runs the r_0-fixed alternative with transmissivity semi-correlated to fracture size was evaluated for all four of the aperture-transmissivity relationships. The case of transmissivity (perfectly) correlated and uncorrelated to fracture size were initially evaluated only for the base-case aperture relationship.

After initial evaluation of results indicated that the most significant cases for buffer erosion calculations were associated with the uncorrelated transmissivity-size relationship and the Hjerne aperture relationship, the combination of these cases for the r_0-fixed alternative was evaluated.

Finally, to assess the effects of uncertainty in the Geo-DFN conceptual models, the OSM-TFM and TCM alternatives were evaluated for two combinations: semi-correlated transmissivity with base-case aperture model, and uncorrelated transmissivity with the Hjerne aperture model.

2.3.3. Results of calculations

Base-case results

The combination of r_0-fixed alternative for the Geo-DFN model, semi-correlated transmissivity-size relationship, and Äspö Task Force model for correlation of aperture to transmissivity, is used as a base case for the present calculations.

The results for ten realizations of this base case, with length-based scaling for frequency of transport pathways, are plotted for each of the three performance parameters U_{r1}, t_w, and F_r in Figure 16. The number of transport paths per realization ranges from 243 to 256, with a median value of 245.

Figure 17 gives the equivalent plots for area-based estimates of U_{r1}, t_w, and F_r. The number of transport paths per realization, using area-based scaling, ranges from 2057 to 2308, with a median value of 2245.

In terms of the cumulative distributions of the performance parameters, the effect of the increased number of transport paths for area-based scaling of frequency is that the results for individual realizations converge toward a central curve representing the cumulative density function that would be expected for an infinite number of realizations.

A similar effect is seen for all of the calculation cases that have been considered. For the remaining calculation cases, results are presented graphically only for the case of area-based scaling, as these give a more clear view of the effects of other assumptions. Results for length-based scaling are provided in spreadsheet form as part of the data deliveries.

Effects of different assumptions regarding the relationship between fracture transmissivity and transport aperture are shown in Figure 18, for a single realization of each case (using the r_0-fixed alternative and semi-correlated T vs. r model, with area-based scaling of frequency).

The different models for aperture influence the advective transport time t_w. The difference between the base case and either the stochastic or cubic-law model are minor. The Hjerne model yields significantly longer advective transport times.

The alternative models for aperture do not influence either U_{r1} or F_r, due to the way that these are linked to the flux density q under the mathematical assumptions of this model.

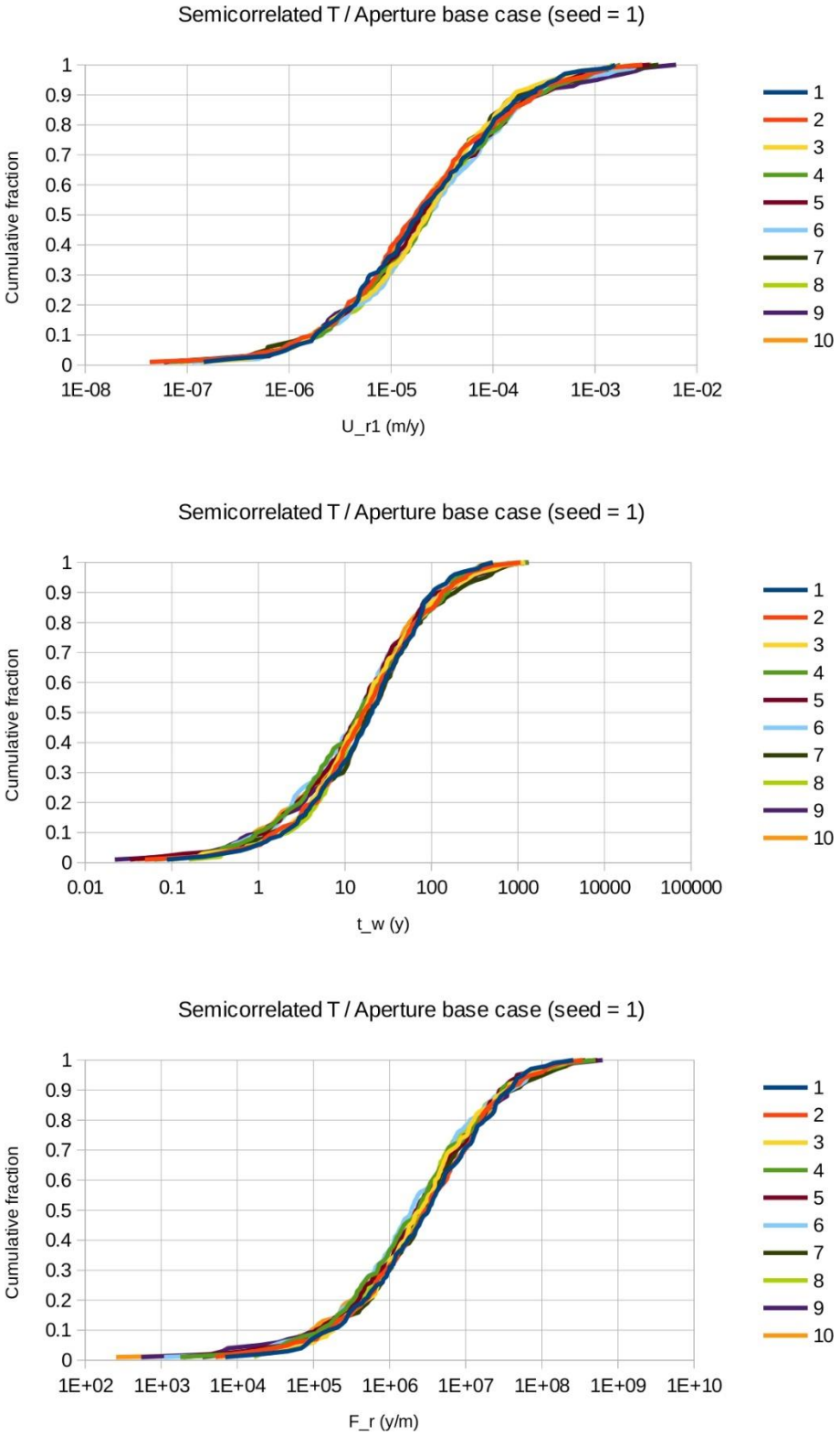

Figure 16: Cumulative distributions of performance parameters U_{r1}, t_w, and F_r for r_0-fixed alternative, semi-correlated transmissivity-size relationship, base-case aperture model and length-based scaling of transport-path frequency. Lines of different colors represent ten different realizations of the Geo-DFN model (according to the legend).

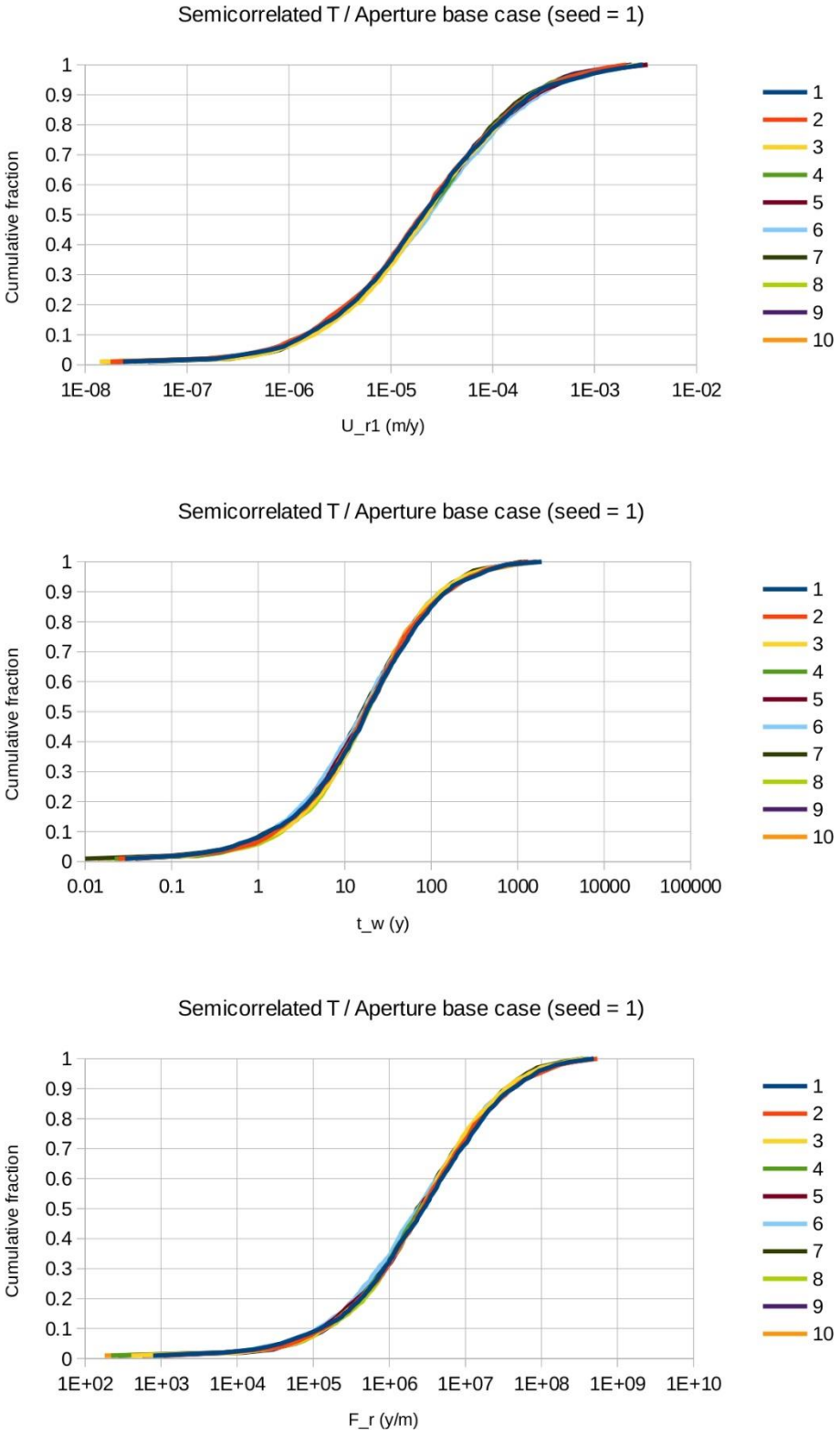

Figure 17: Cumulative distributions of performance parameters U_{r1}, t_w, and F_r for r_0-fixed alternative, semi-correlated transmissivity-size relationship, base-case aperture model and area-based scaling of transport-path frequency. Lines of different colors represent ten different realizations of the Geo-DFN model (according to the legend).

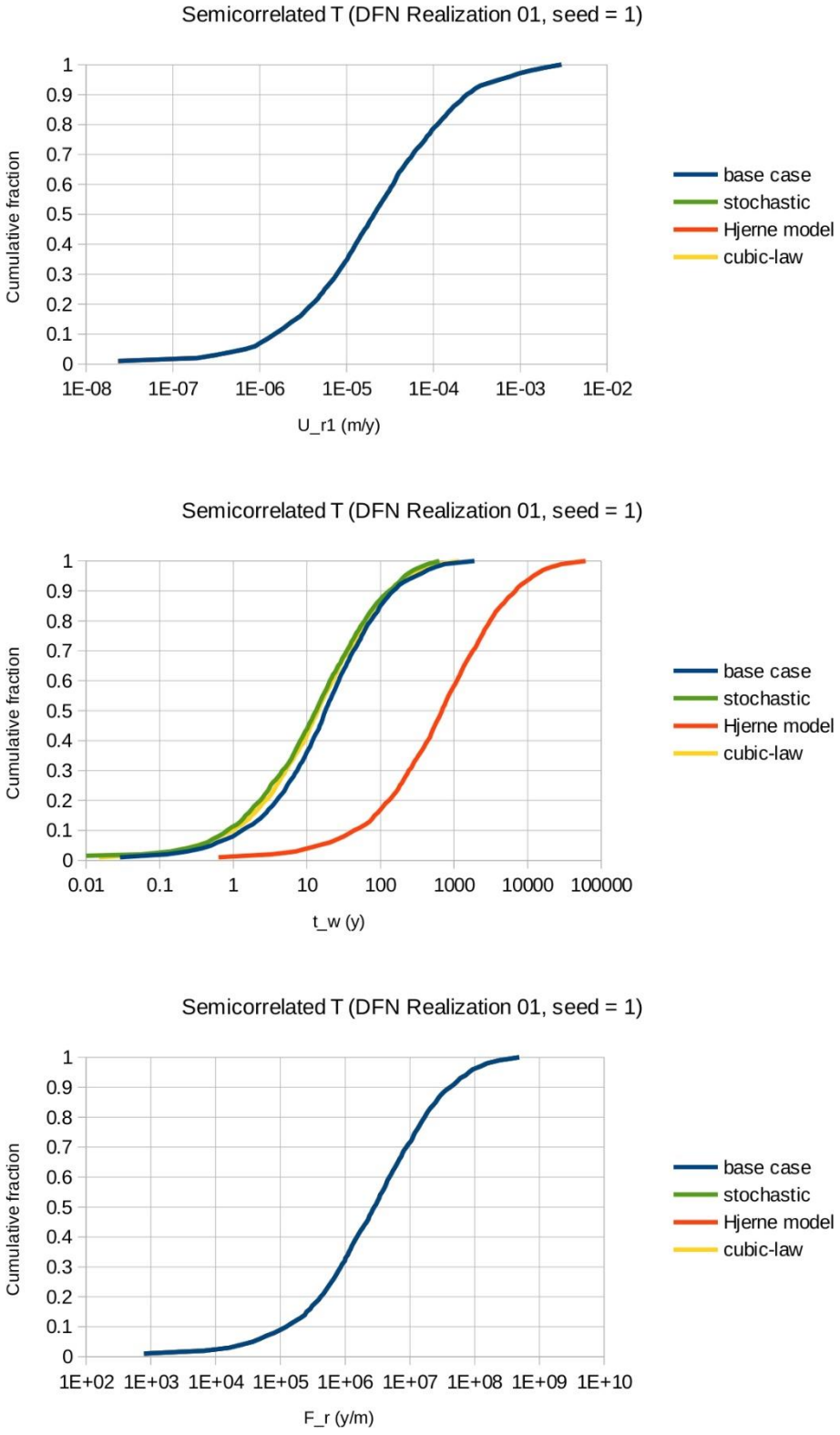

Figure 18: Effect of different assumptions for the relationship of aperture to transmissivity, in terms of cumulative distributions of performance parameters U_{r1}, t_w, and F_r for a single realization of models based on the r_0-fixed alternative, semi-correlated transmissivity-size relationship, and area-based scaling of transport-path frequency. Lines of different colors represent the different aperture-transmissivity relationships (according to the legend).

The uncorrelated transmissivity-size model (Figure 19) results in a near-field flux U_{rl} distribution which is shifted toward higher values by about half an order of magnitude relative to the semi-correlated case (with the base-case aperture model). Advective travel times t_w are decreased by less than half an order of magnitude. Transport resistance F_r is also decreased by less than half an order of magnitude.

The correlated transmissivity-size model (Figure 20) has a more pronounced effect on the performance-parameter distributions. The median value of near-field flux U_{rl} is increased by nearly an order of magnitude relative to the semi-correlated case, but the distribution of values is significantly narrower, with the net result that the highest values of U_{rl} are an order of magnitude less than the highest values in the semi-correlated case.

Advective travel times t_w and transport resistance F_r likewise have narrower ranges of variation. For these two parameters, extremely low values are of primary concern for safety assessment. The correlated model produces less extremely low values of t_w and F_r than the semicorrelated model.

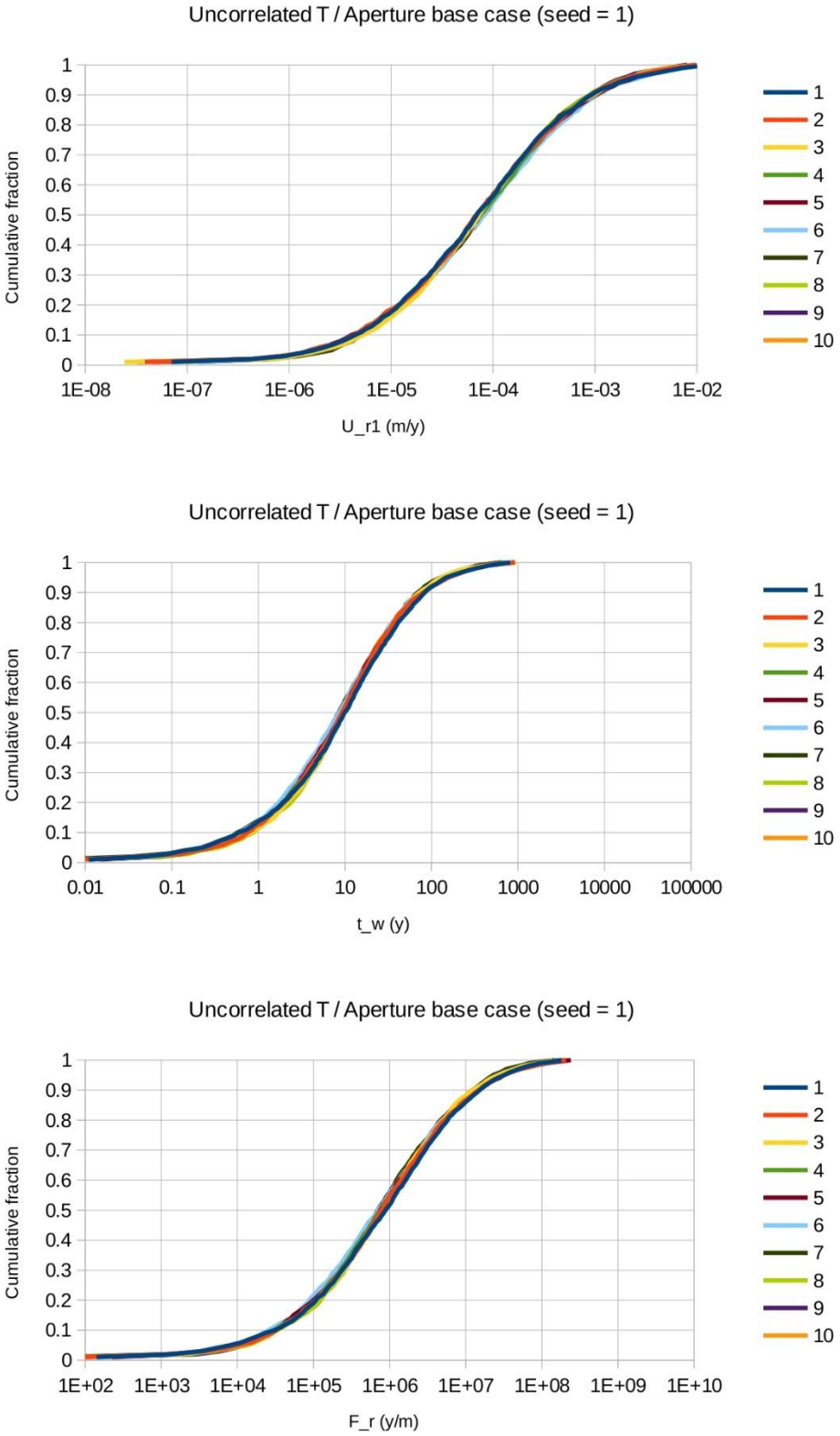

Figure 19: Performance parameter estimates for r_0-fixed alternative, uncorrelated transmissivity-size relationship, base-case aperture model and linear scaling of transport-path frequency, for ten realizations of the Geo-DFN model (as indicated by differently colored lines).

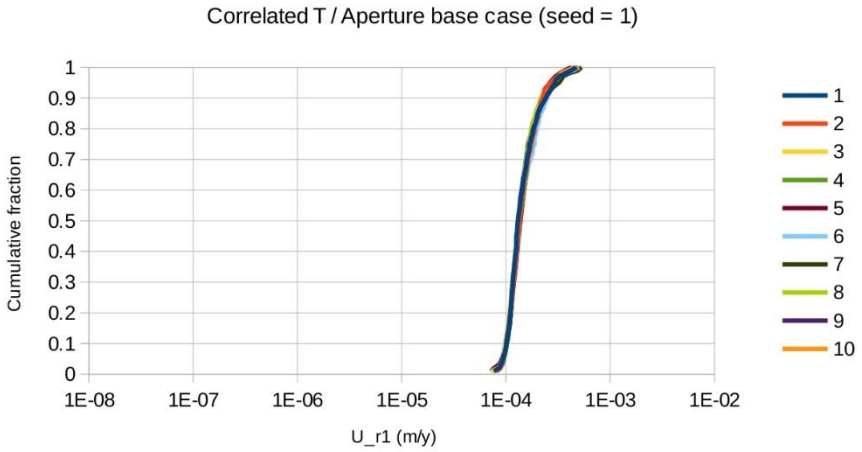

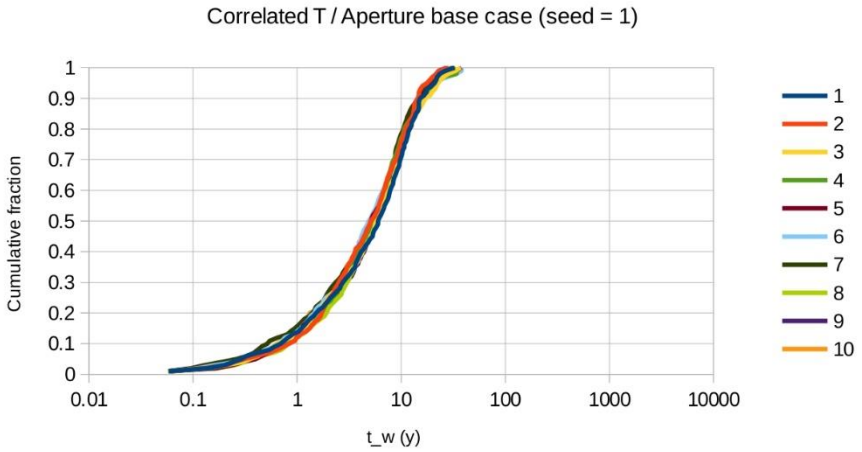

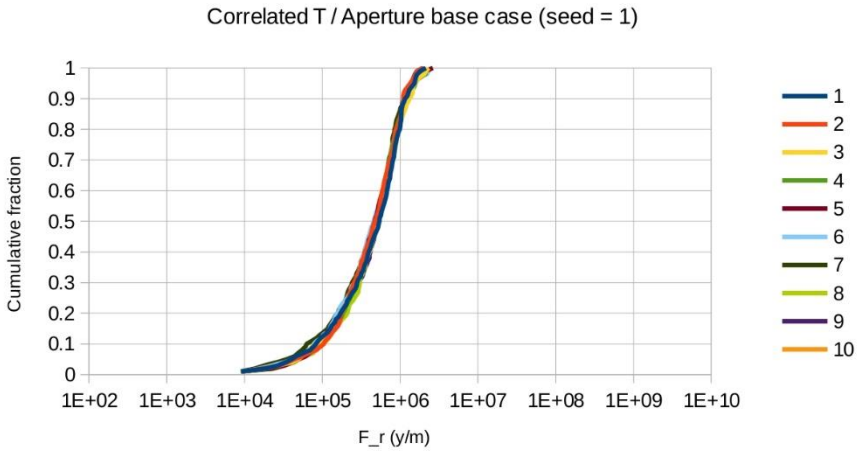

Figure 20: Performance parameter estimates for r_0-fixed alternative, perfectly correlated transmissivity-size relationship, base-case aperture model and linear scaling of transport-path frequency, for ten realizations of the Geo-DFN model (as indicated by differently colored lines).

The main effects of the OSM-TFM and TCM alternative Geo-DFN models are in terms of the number of deposition holes that connect to transport pathways for area-based scaling (Table 4). These are directly a result of differences between these models in terms of intersections with deposition holes (Table 5). The TCM and OSM-TFM models both produce more intersections with deposition holes (considering just the medium- to large-radius fractures that are not avoided by SKB's criteria for placement of deposition holes, as detailed by Geier, 2014). For area-based scaling, effectively all intersections count as potential transport paths.

Table 4: Effect of Geo-DFN alternative and frequency scaling method on the predicted numbers N_{trans} of deposition holes that are connected to transport pathways. Note that the models for fracture size-transmissivity relationship and fracture transmissivity-aperture relationship have no effect on these numbers, so it is sufficient to consider the results for semicorrelated T vs. r and the base-case (Äspö Task Force) model for b_T vs. T.

Geo-DFN Alternative	Scaling	Minimum Nt_{rans}	Maximum Nt_{rans}	Mean Nt_{rans}	Median Nt_{rans}
r0-fixed (r3)	Linear	243	256	246	245
OSM-TFM (o3)	Linear	239	245	242	241
TCM (t2)	Linear	224	236	230	231
r0-fixed (r3)	Area	2057	2308	2224	2245
OSM-TFM (o3)	Area	3921	4265	4040	4031
TCM (t2)	Area	4924	5406	5199	5192

Table 5: Effect of Geo-DFN alternative on numbers N_X of intersections with deposition holes.

Geo-DFN Alternative	Scaling	Minimum Nt_{rans}	Maximum Nt_{rans}	Mean Nt_{rans}	Median Nt_{rans}
r0-fixed (r3)		2057	2308	2224	2245
OSM-TFM (o3)		3921	4265	4040	4031
TCM (t2)		4924	5406	5199	5192

Comparing the values of N_{trans} for area-based scaling with the values of N_X in Table 5, it can be seen that the numbers are identical. This is because, as mentioned previously, p_{cA} generally exceeds 1 so all fracture/deposition-hole intersections $\boldsymbol{X}$ are treated as transmissive intersections.

For length-based scaling, p_{cL} is always less than 1 so the number of potential transport paths N_{trans} is limited by the product of the frequency of PFL anomalies times the total length of deposition holes, i.e. $P_{10,PFL} L_{dh} N_{dh}$.

This product does not change between the simulations for different Geo-DFN alternatives, so it should be expected that N_{trans} should be approximately the same. The small but significant differences between the mean values and ranges of N_{trans} for the different Geo-DFN alternatives, as seen in Table 4, may to some extent be an artefact of details of the discrete simulation methodology used here. It should not be affected by SKB's calibration of the size distributions, with the methodology used here.

In terms of the cumulative density functions of performance parameters, the results for the OSM-TFM and TCM alternatives (Figures 21 and 22) are practically identical to the results for the r_0-fixed alternative (Figure 16).

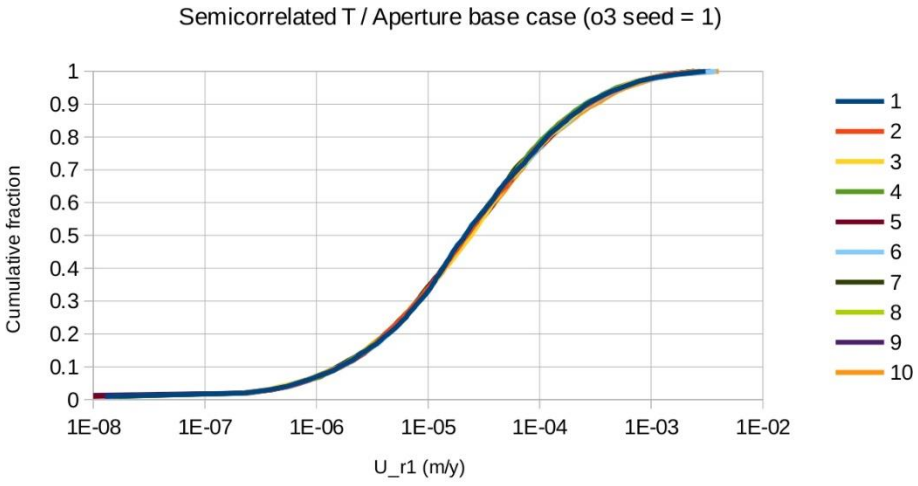

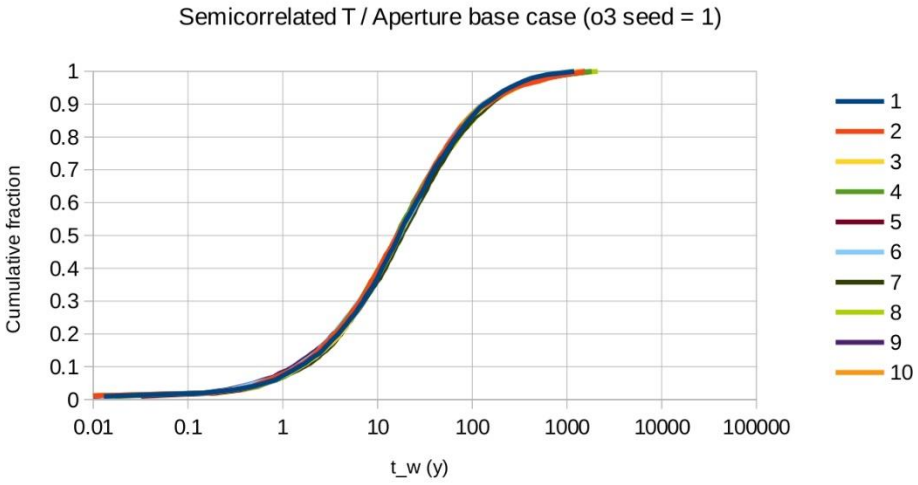

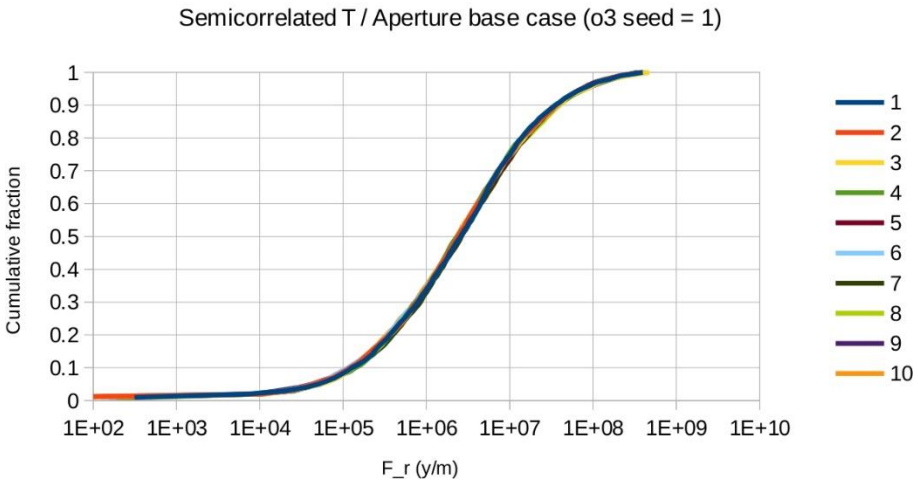

Figure 21: Performance parameter estimates for OSM-TFM alternative, semi-correlated transmissivity-size relationship, base-case aperture model and area-based scaling of transport-path frequency, for ten realizations of the Geo-DFN model (as indicated by differently colored lines).

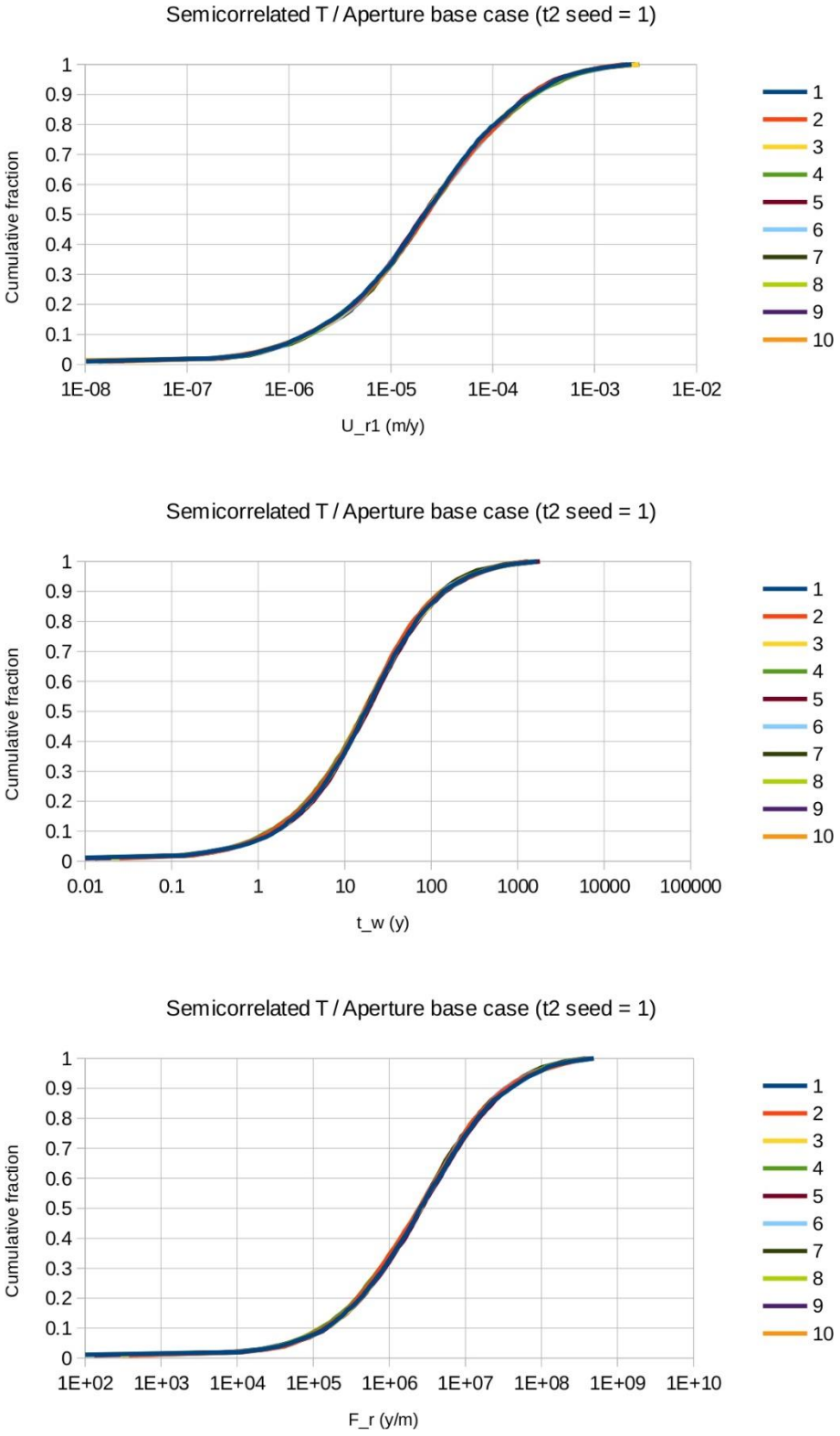

Figure 22: Performance parameter estimates for TCM alternative, semi-correlated transmissivity-size relationship, base-case aperture model and area-based scaling of transport-path frequency, for ten realizations of the Geo-DFN model (as indicated by differently colored lines).

2.3.4. Discussion

The distributions of performance measures obtained with the simple series model are generally quite similar to the results of SKB's much more complex hydrogeological models based on the DFN conceptual model.

Table 6 compares the statistics of the obtained distributions for U_r for the two different modelling approaches, for the three different fracture transmissivity vs. size relationships (semi-correlated, uncorrelated, and perfectly correlated) in combination with the base-case Äspö Task Force model for aperture. Table 7 gives a similar comparison in terms of the statistics for F_r. The statistics for SKB's DFN model correspond to the distributions as plotted in Figure 6, while the results for the simple series model correspond to the distributions as plotted in Figures 16, 19, and 20.

Table 6: Approximate percentiles of U_r from the temperate-climate model of SKB in comparison with the simple series model presented in this report, for three alternative models for the relationship of fracture transmissivity to fracture size in combination with the base-case model for base-case (Äspö Task Force) model for aperture. Values for SKB's model are estimated graphically from Joyce et al. (2010, Figure 6-28, reproduced as Figure 6 of this report). All values are in m/yr. The highest value in each column is highlighted in bold.

Transmissivity model	10th percentile	Median	90th percentile	Maximum
Semicorrelated (SKB)	$1.6\text{x}10^{-6}$	$1.0\text{x}10^{-5}$	$1.6\text{x}10^{-4}$	~$1\text{x}10^{-2}$
Semicorrelated (simple)	$1.8\text{x}10^{-6}$	$2\text{x}10^{-5}$	$2.5\text{x}10^{-4}$	~$1\text{x}10^{-2}$
Uncorrelated (SKB)	$4\text{x}10^{-6}$	$4\text{x}10^{-5}$	$5\text{x}10^{-4}$	~$1\text{x}10^{-2}$
Uncorrelated (simple)	$4\text{x}10^{-6}$	$8\text{x}10^{-5}$	$1.0\text{x}10^{-3}$	~$1\text{x}10^{-2}$
Correlated (SKB)	$2.5\text{x}10^{-6}$	$2\text{x}10^{-5}$	**$2.5\text{x}10^{-3}$**	**~$4\text{x}10^{-2}$**
Correlated (simple)	**$1.0\text{x}10^{-4}$**	**$1.6\text{x}10^{-4}$**	$2.5\text{x}10^{-4}$	~$5\text{x}10^{-4}$

Table 7: Approximate percentiles of F_r from the temperate-climate model of SKB in comparison with the simple series model presented in this report, for three alternative models for the relationship of fracture transmissivity to fracture size in combination with the base-case model for base-case (Äspö Task Force) model for aperture. Values for SKB's model are estimated graphically from Joyce et al. (2010, Figure 6-28, reproduced as Figure 6 of this report). All values are in yr/m. The lowest value in each column is highlighted in bold.

Transmissivity model	Minimum	10th percentile	Median	90th percentile
Semicorrelated (SKB)	~$4\text{x}10^{3}$	$5\text{x}10^{5}$	$2.5\text{x}10^{6}$	$4\text{x}10^{7}$
Semicorrelated (simple)	$4\text{x}10^{2}$ – $8\text{x}10^{3}$	$1\text{x}10^{5}$	$2.5\text{x}10^{6}$	$3\text{x}10^{7}$
Uncorrelated (SKB)	~$4\text{x}10^{3}$	$5\text{x}10^{5}$	$4\text{x}10^{6}$	$2\text{x}10^{7}$
Uncorrelated (simple)	**$1\text{x}10^{2}$** – $8\text{x}10^{3}$	**$3\text{x}10^{4}$**	$8\text{x}10^{5}$	$1.6\text{x}10^{7}$
Correlated (SKB)	~$3\text{x}10^{3}$	$1.6\text{x}10^{5}$	$2\text{x}10^{6}$	$2\text{x}10^{7}$
Correlated (simple)	~$1\text{x}10^{4}$	$8\text{x}10^{4}$	**$5\text{x}10^{5}$**	**$1.6\text{x}10^{6}$**

For the semi-correlated case, the distribution of U_r predicted by the simple model is slightly more conservative than SKB's estimates, but within a factor of 2. In terms of F_r the simple model is also more conservative than SKB's estimates, but within an order of magnitude for the most extreme low values, and practically converging to the same results for the upper part of the F_r distribution.

For the uncorrelated case, relationship between the two models is qualitatively the same as for the semi-correlated case. The distribution of U_r predicted by the simple model is again slightly more conservative than SKB's estimates but within a factor of 2. The distribution of F_r predicted by the simple model is more conservative than SKB's estimates, but once again within an order of magnitude for the most extreme low values, and converging to practically the same results for the upper part of the F_r distribution.

For the correlated case, a different relationship is seen. In terms of U_r, the simple model predicts a much narrower range of values than SKB's estimates for the correlated case, and is *less* conservative for the upper part of the distribution. In terms of F_r for the correlated case, the simple model is again less conservative than SKB's models, by about a factor of about 3 for the most extreme low values, but slightly more conservative in terms of the 10th percentile values and higher percentiles.

Considering the assumptions of the simple series model, the performance measures from the simple model are almost entirely determined by the size and transmissivity of the first fracture to intersect a given deposition hole, and then an assumption of a connection to the nearest HCD via large-scale fractures. The similarity with SKB's results for the semi-correlated and uncorrelated cases thus suggest that the performance measures produced by SKB's models are strongly determined by the same factor.

This has been suggested in a previous review by Black (2012) who noted that the very sparse fracture intensity (or density, in Black's terminology) of SKB's hydro-DFN models, in combination with the power-law models for fracture size (radius or extent) essentially leads to a hydrogeological model in which deposition holes are connected to the far-field hydrogeological network only – or with rare exceptions – if they are intersected by a fracture that connects directly to a "skeleton" or framework of very large, discrete fractures.

Although SKB's Geo-DFN model has been used here as the basis for calculating the frequency of intersections with deposition holes, the parameters of the intersecting fractures are based on SKB's Hydro-DFN model. The simple series approach used here effectively amounts to an assumption similar to that pointed out by Black (2012) with regard to SKB's models, namely that fractures intersecting deposition holes tend to connect directly to the large-scale conductive skeleton.

The difference between the results of SKB's model and the simple series-conductor model used here, in the case of perfectly correlated T vs. r, is believed to be an artefact of combining perfect correlation of transmissivity with the highly simplified assumption regarding the second segment in each path, namely that this is of length equal to the remaining distance to the HCD, or the maximum fracture radius (whichever is less). For fracture domain FFM01 the correlation model from Table 2 is effectively:

$$T \propto \sqrt{r}$$

In a two-segment path of total length L this means that the effective series transmissivity of a path with initial fracture radius r_1 will be proportional to:

$$f(r_1) = \frac{\sqrt{r_1}\sqrt{L - r_1}}{\sqrt{r_1} + \sqrt{L - r_1}}$$

From this relationship it can be seen that a large initial radius will be compensated by a smaller second segment length, resulting in a narrow range of effective transmissivity. As plotted in Figure 23, the result for path lengths of L from 600 m to 1000 m is less than an order of magnitude of variation over the possible range of r_1. In the DFN model used by SKB, the coupling between the transmissivity of the first and second fracture in a given path to the nearest HCD would presumably be less rigid, allowing a wider range of variation in both U_r and F_r.

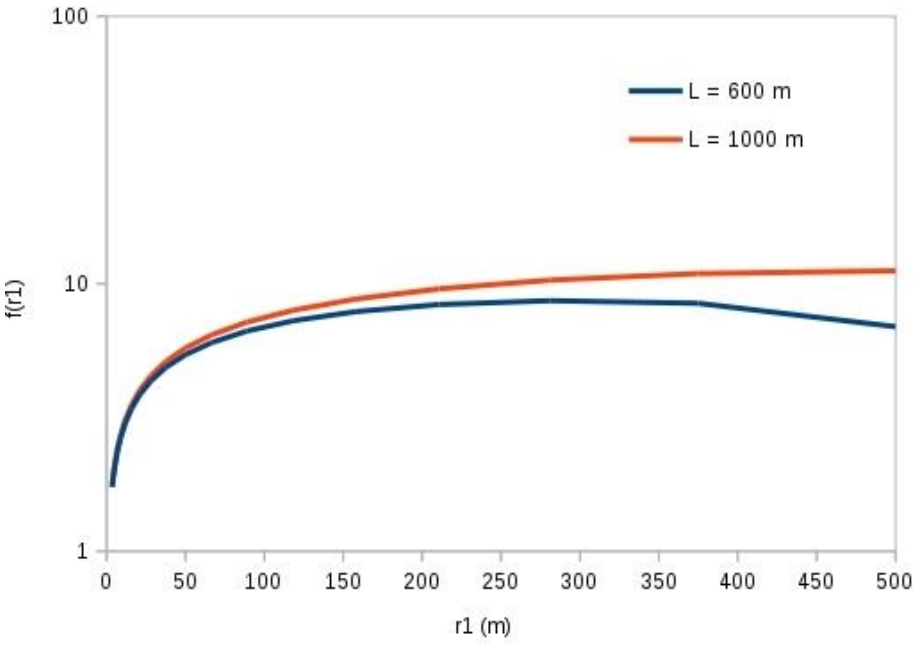

Figure 23: Plot of the function $f(r_1)$ as defined in the text for two different values of distance L to the nearest HCD.

As noted in Section 2.1.2, in SKB's approach the correlated model yields the highest values of U_r and lowest values of F_r. Joyce et al. (2010) speculate that the most extreme cases of Ur are due to a few large stochastic fractures, which for the correlated model will invariably have high transmissivities.

The possibility of such extreme connections apparently makes SKB's model of this case more conservative than the same case of the simple-series model. However, the 90th percentile and maximum values of U_r for the correlated case of SKB's model only exceed the corresponding statistics for the uncorrelated simple series model by factors of 2.5 and 4, respectively. In terms of F_r, the uncorrelated simple series model produces the most conservative values overall.

Relationship to sparse channel networks

The concept of "strong channelization" represented by the area-scaled estimates in the simple-series model differs from the idea of sparse channel networks as raised by Black et al. (2007) and Black (2012).

The idea of "strong channelization" used here refers only to the fraction of a fracture's width within which flow is concentrated. This is a simple geometric effect that relates directly to the probability of intersection with a deposition hole, if the typical channel width is small in comparison with the deposition-hole diameter.

The concept of sparse channel networks has an additional idea of long distances between the points at which channels connect. As developed by Black et al. (2007) and subsequent work, this concept provides an explanation of observations of apparent "hyperconvergence" effects around tunnels, and the apparent sparseness of mixing points in underground tracer studies. The concept doesn't depend so much on the absolute width of the channels, as it does on the distance between the points where channels connect to each other.

The simple series-conductor model, as presented here, still depends on SKB's parameterization of the sparsely fractured rock in terms of a DFN model. Thus the results, even with area-based scaling, do not resolve the questions raised by the alternative conceptual model of sparse channel networks. As noted by Black (2012) a sparse channel network might lead to a lower number of deposition holes with significant flow, which is the opposite of what comes from the area-based scaling of P_{32}.

Applicability of Hjerne aperture model for buffer erosion calculations

SKB has argued that the Hjerne model should be excluded for buffer erosion calculations, but the reasons are not well explained in SKB TR-10-66 or in the SR-Site Data Report.

A possible argument in favor of this position could be that the Hjerne model represents the effective aperture available for transport, for solutes moving between boreholes which can encounter the full range of apertures in a given fracture. This effective transport aperture does not represent the effective hydraulic aperture for fractures along a given transport path. Therefore it does not provide a "most likely" estimate of groundwater velocities affecting erosion of buffer at a deposition hole.

However, SKB has not provided any alternative approach for assessing the effects of uncertainty in the T vs. aperture relationship. Therefore, and for lack of a different bounding case, it seems reasonable to use this as a conservative case for buffer erosion calculations.

3. Effects of salinity

3.1. SKB's presentation of salinity effects

3.1.1. Development of groundwater salinity

SKB's treatment of the development of groundwater salinity has been described thoroughly in a technical note for SSM by Bath (2014). Therefore only the key points of SKB's presentation pertaining to estimation of performance measures are noted here, with reference to Bath (2014) for a more detailed treatment.

SKB's evaluation of salinity evolution is based on a regional ECPM model which is developed by upscaling from the Hydro-DFN model in combination with site-scale and regional-scale models of hydraulic conductor domains (HCDs). The parameters have been adjusted to match (at least approximately) a sparse dataset for the compositions of mobile groundwater and pore water at depth. The details of this work are described by Hartley et al. (2006), Follin et al. (2007), and Follin (2008). The models account for diffusive exchange of solutes between fracture waters and pore waters by means of a 1D model for matrix diffusion, which for the temperate case (Joyce et al., 2010) is a single-rate diffusion model, while the model for the periglacial and glacial periods (Vidstrand et al., 2010) incorporates a multi-rate diffusion model.

Site-scale impacts of the evolving salinity have been assessed with a hybrid ECPM-DFN approach. Salinity evolution on the site scale is modelled using a ECPM representation with a dual porosity model for diffusive exchange with matrix pore waters. The DFN submodel around the repository is coupled to the surrounding ECPM with continuity of pressure and mass flux for a series of time slices which are modelled as steady state, but without advective transport of salinity in the DFN. An analytical approximation is used to account for matrix diffusion within the DFN.

The parameters have been adjusted to match (at least approximately) a sparse dataset for the compositions of mobile groundwater and pore water at depth. The details of this work are described by Hartley et al. (2006), Follin et al. (2007), and Follin (2008). The models account for diffusive exchange of solutes between fracture waters and pore waters by means of a 1D analytical equation for matrix diffusion.

The effective matrix diffusivity used for paleohydrogeological modelling of saline water is calculated from the formula:

$$D_e = F_f D_w$$

where F_f is the formation factor (1.8×10^{-5} for undisturbed rock based on the mean of values obtained by electrical measurements) and D_w is the harmonic mean of the diffusivities of the ion pair Na^+ and Cl^- for temperatures at repository depth, and taking into account anion exclusion effects for Cl^- as discussed by Joyce et al. (p. 143), leading to a value of $D_e = 4 \times 10^{-14}$ m/s that was used for paleohydrogeological simulations.

In the model of Vidstrand et al. (2010, p. 51), a multi-rate formulation is used for matrix diffusion, parametrized in terms of ten exchange-rate coefficients α_i (i = 1, 2,

…, 10). The text refers to Appendix D for details on the choice of these coefficients but notes that the settings are provisional. The relevant part of Appendix D, Section D.3, refers to the description of how multi-rate matrix diffusion is implemented in DarcyTools as given by Svensson et al. (2010).

The multi-rate matrix diffusion model as implemented in DarcyTools (Svensson et al., 2007, Section 3.5) is based on the conceptualization of Haggerty and Gorelick (1995) in which the immobile zone within the matrix is conceptually considered to be divided into different sub-volumes with different characteristic length scales l that exchange mass with the mobile zone at different rates. In the DarcyTools implementation, these sub-volumes are considered to result from fractures on scales below those that participate in the flowing network, with properties derived from the following key assumptions (Svensson et al., 2010, p. 26):

- Fractures within the immobile zone have the same power-law size distribution exponent a as the larger fractures that participate the flowing network (thus a is extrapolated from larger scales);
- These fractures are assigned to a particular length-scale l based on their size;
- The transport apertures of these fractures are proportional to their length scales according to: $e_T \sim l^{\gamma}$.
- The effective diffusion coefficient associated with a given length scale is assumed to be $D_e(l) = D_m(l/l_{min})^{\Psi}$, where D_m is the molecular diffusion coefficient in free water.

Svensson et al. (2010, p. 35 and Appendix B) show that the parameters a, γ, and Ψ can be related to the late-time slope of the breakthrough curve k (for in-situ tracer tests):

$$k = \frac{a - \gamma - 2\Psi + 1}{2 - \Psi}$$

The parameters needed to specify the multi-rate diffusion model are thus the late-time slope k, the minimum and maximum rate coefficients α_{min} and α_{max}, and the volume ratio β between the immobile and mobile zones.

In applying this model Vidstrand et al. (2010, p.51) choose a value $\alpha_{min} = 4\text{x}10^{-12}$ s-1 which they note implies a time scale of approximately 8000 years for the portion of the immobile zone that interacts most slowly with the mobile zone (flowing fracture network). The volume ratio β is set to 10 based on a recommendation by Follin et al. (2005) that this should be in the range 10 to 100.

Vidstrand et al. note that "[b]oth settings are regarded as provisional." Their further discussion of these parameters (in Appendix D.3 of the same report) notes that the chosen values of α_{min} and β lead to penetration depths for the most remotely interacting part of the immobile zone on the order of 2 m to 6 m after 8000 years, given the range of D_e values adopted by Joyce et al. (2010). No further data-based evidence is cited for the choice of parameters, but Vidstrand et al. (2010) note that these values lead to a model in which matrix porewater chemistry far from the

flowing fractures at (or below) repository depth is unlikely to be affected by hydrodynamics during a glacial cycle.

3.1.2. Dilute water infiltration

SKB's assessment of the possibility for dilute water to reach deposition holes is described in Appendix F of Joyce et al. (2010). The method for calculating the persistence of dilute water is based on the standard analytical solution for the time-dependent concentration $C(t)$ of initially fresh water along a streamline with matrix diffusion of out of an infinite matrix initially having a solute at uniform concentration C_o:

$$\frac{C(t)}{C_o} = \text{erf}\left(\frac{F\sqrt{\epsilon_p D_e}}{2\sqrt{t - t_w}}\right)$$

where:

t_w = advective water travel time (estimated from flow models);

ϵ_p = matrix porosity = 0.0037 as used in paleohydrogeological simulations;

D_e = effective matrix diffusivity in situ = $4\text{x}10^{-14}$ m^2/s = $1.26\text{x}10^{-6}$ m^2/y as used for paleohydrogeological simulations.

F = transport resistance (estimated from flow models).

For a given dilution ratio α, the corresponding breakthrough time is obtained by setting $C(t)/C_o = \alpha$ and solving for t to give:

$$t = t_w + \frac{F^2 \epsilon_p D_e}{4[\text{erf}^{-1}(\alpha)]^2}$$

where $\text{erf}^{-1}(\alpha)$ is the inverse error function, *i.e.* $x = \text{erf}^{-1}(\alpha)$ implies that $\text{erf}(x) = \alpha$. For the case of where the matrix depth available for matrix diffusion is limited to a distance δ_m, and assuming that advection is slow enough to allow equilibrium transport conditions to apply, the time for advance of the mixing front is:

$$t = t_w + \epsilon_p \delta_m F$$

SKB has used the minimum of these two formulae (infinite-acting diffusion and steady-state finite-matrix depth) as a lower-bound (conservative) estimate of the breakthrough time required for water at a given dilution ratio α to reach a deposition hole:

$$t_b = t_w + \min\left\{\frac{F^2 \epsilon_p D_e}{4[\text{erf}^{-1}(\alpha)]^2}, \epsilon_p \delta_m F\right\}$$

According to Joyce et al. (2010, p. 164), the latter term becomes the limiting term when $F > 3\text{x}10^5$ y/m, when using $\alpha = 0.1$ and $\delta_m = 12.5$ m.

The value $\delta_m = 12.5$ m is based on the approximate spacing of Posiva Flow Log (PFL) anomalies. Joyce et al. (2010, p. 172) argue that there is evidence that matrix pore waters and fracture waters are in equilibrium in the upper bedrock above -300 m, and that there is "some field evidence" to support equilibrium conditions in the middle depths around -200 m to -400 m, where the PFL anomaly spacing is about 12.5 m.

Values of transport resistance F and advective travel time t_w are obtained from backward particle tracking in either the hydrogeological base case model of Joyce et al. (2010) or from variants with appropriate ice front locations. Although these models consist of a DFN component nested within a larger-scale continuum model, for purposes of estimating F and t_w, only the portions of the recharge paths that lie within the explicit DFN portions of the nested model are included in the calculation.

The backward particle tracking is done only from deposition-hole positions that are not excluded based on the full-perimeter criterion (FPC) or extended full-perimeter criterion (EFPC) as defined by Munier (2010). The breakthrough time for dilute water to reach the deposition holes along the paths thus identified is compared with the predicted durations of the three climate situations considered (Joyce et al., 2010, Table F-2):

- Temperate (10,000 y to 60,000 y);
- Ice front over site (20 y to 100 y);
- Ice sheet over site (20,000 y to 100,000 y).

If the breakthrough time is less than the duration of the climate situation, then the position is considered to be affected by dilute water penetration, and the transport resistance F_r for the release pathway is also calculated (by forward particle tracking).

Results are produced for two different dilution factors, $\alpha = 0.1$ and $\alpha = 0.02$. According to Joyce et al. (2010, p. 172) the higher value $\alpha = 0.1$ leads to a dilution of about 1 g/L TDS at repository depth for the temperate period and 0.3 g/L for the glacial period. As the buffer criterion requires salinity of at least 0.3 g/L TDS, this can be viewed as conservative or realistic depending on the climate situation considered. The lower value $\alpha = 0.02$ leads to a dilution of about 0.2 g/L TDS at repository depth for the temperate period and 0.06 g/L for the glacial period, which are both below the salinity criterion; these results are used as a sensitivity measure.

For the situation of an ice front over the site, in addition to calculations in which the permeability structure was the same as the hydrogeological base-case model, additional calculations were carried out using an "extended spatial variability" variant for the CPM portion, based on data from the ongoing SFR investigations as discussed in Section 5.4 of Joyce et al. (2010). For this case, the regional-scale and site-scale portions of the model are treated as a spatially variable ECPM rather than a homogeneous CPM. Also, the DFN portion of the model is extended northward beyond the Singö deformation zone, so this model include a larger DFN component.

A summary of the results for the hydrogeological base-case model as well as the extended spatial variability case is reproduced in Table 8. It can be seen that the results for the base-case permeability structure are insensitive to the use of a lower (non-conservative) value of α except for climate situations with a duration of about 10,000 y or less. Use of the extended spatial-variability variant reduces the number of holes that are predicted to encounter dilute water by 30% to 40% for the ice-front situation, due to taking credit for additional F through the recharge pathway via the extended DFN.

Table 8: Estimates of numbers of deposition holes that become critically diluted by the end of each climate situation, as calculated by Joyce et al. (2010, Tables F-3 and F-4) for different durations and values of the dilution factor α. Results are shown for calculations based on the hydrogeological base-case model which uses as homogeneous CPM representation on larger scales, as well as for an extended spatial-variability variant (for which results were obtained only for the situation of an ice front over the site).

Climate situation	Duration (y)	Base case permeability model α = 0.02	Base case permeability model α = 0.1	Extended spatial variability α = 0.1
Temperate	10,000	42	52	–
	60,000	166	166	–
Ice front over site	20	16	77	44
	100	32	147	99
Ice sheet over site	20,000	37	37	–
	100,000	157	157	–

3.2. Motivation of the assessment

Long-term stability of groundwater chemistry at repository depth, within certain broad acceptable bounds, is important for SKB's safety case in order to assure that the engineered barriers perform their safety functions. In particular, the bentonite buffer should not be exposed to highly saline waters (such as could result from up-coning of deep brines) or strongly dilute waters such could theoretically result from infiltration of either meteoric waters during a prolonged temperate period, or glacial meltwaters during a glaciation cycle.

SKB's primary means of assessing these issues are (1) paleohydrogeochemical evidence and (2) predictive hydrogeological models for the ongoing temperate period and for future glaciations. This assessment focuses on the predictive hydrogeological models, in particular their application to assess penetration of dilute waters to repository depth

3.3. The Consultant's assessment

The salinity evolution models require assumptions regarding the initial state 10,000 years before present (BP) in terms of the distribution of reference waters. SKB's choice of initial distributions are justified at least in part by comparison with the models' ability to match present-day groundwater compositions as determined from the site investigation program. The measurements at depth are sparse and, as Bath (2014) notes, the general match is modest with “no coherence between the shape of the modelled profile and the few available measurements.”

The ECPM model for infiltration of glacial water (Vidstrand et al., 2010) and the repository-scale DFN model for penetration of glacial melt water to repository structures (Joyce et al., 2010, p. 116-127) include out-diffusion of salts from matrix pore waters into the dilute meltwater. The models are conservative in that they do not take credit for other rock-water interactions that could be expected to attenuate

penetration of very dilute waters, and they assume zero initial salinity of the melt waters.

The key uncertainties in this approach as recognized by SKB (2011, p. 509-10), and as summarized by Bath (2014, p. 21), can mostly be viewed as having been handled in a conservative way in SKB's approach for predicting the penetration of dilute waters to the repository. These include use of steady-state flow fields, no rock-water interactions, and small domain size (which artificially limits the length of recharge paths. The use of simple scaling factors for comparing Darcy flux at different times during a glacial cycle is a simplification that might be either conservative or non-conservative, but the effect is unlikely to be large.

Uncertainties arising from the upscaling from a DFN to ECPM representation are not discussed at this level of SKB's reporting. The formulae for kinematic porosity φ and flow wetted surface a_r of the upscaled ECPM blocks as given by Joyce et al. (2010, p. 30, and in further detail in Appendix C) are simply summations of the contribution of each individual fracture, without regard to network effects. The kinematic porosity φ is furthermore multiplied by a factor of 10 to account for the porosity due to the inferred population of fractures that are smaller than the smallest ones included in the DFN simulations.

Thus the calculated values of φ and a_r in the ECPM thus are likely larger than what would be calculated if only fractures participating in network flow, depending on the flow direction, were included in the calculation. This would potentially lead to non-conservative results if the ECPM were used to estimate attenuation of dilute melt waters by matrix diffusion. Joyce et al. (2010) have avoided this problem by excluding the contribution of the ECPM portion of their model to the values of F and t_w that they use in calculating times for dilute water to reach deposition holes.

An additional uncertainty, as discussed by Bath (2014, p. 42-43), is the assumption that the entire matrix between transmissive fractures is accessible for matrix diffusion. For fracture domain FFM01, the diffusion-accessible matrix depth is thus assumed to be about 12.5 m. Positive evidence for matrix diffusion acting over these distances in granitic rock is scant, and the few in-situ experiments that give some support may be site-dependent. As noted by Bath (2014), evidence to contradict this assumption is also lacking. However a more conservative assumption would be that matrix diffusion depths are more limited, and possibly heterogeneous.

As discussed above, the value δ_m = 12.5 m used by Joyce et al. (2010) to calculate dilute water penetration times is based on the approximate spacing of Posiva Flow Log (PFL) anomalies. One question is whether the use of PFL anomaly spacing provides a conservative value for estimating the times for dilute waters to penetrate to the repository depth.

PFL anomalies are based on flowrates observed in fractures under strongly converging flow situations. In SKB's development of the Hydro-DFN model, it has been speculated that flows to some transmissive fractures are limited by “hydraulic chokes” In a non-converging flow situation, such “chokes” would be less likely to play such a strong role, and more of these fractures might participate in the flow, leading to a smaller effective spacing between hydraulically significant fractures. Smaller values of δ_m would lead to shorter estimates of the time needed for dilute waters to reach deposition holes.

The alternative treatment of matrix diffusion by use of a multi-rate model by Vidstrand et al. (2010) gives broadly consistent behavior with the single-rate model used by Joyce et al. (2010) at least for the longer time scales considered, *i.e.* on the order of 8000 years. This should be expected as the parameters of the multi-rate model that act on longer time scales were chosen to conform to the single-rate

model. For these long time scales all classes of immobile zones in the multi-rate are close to reaching equilibrium, so the behavior is controlled by assumptions regarding the total pore volume of the immobile zones.

Greater differences between the two matrix-diffusion models might be expected for shorter time spans, in particular the ice-front case for which the time scales of concern are in the range 20 to 100 years. At these shorter time scales, the slower-acting classes of immobile zones hypothesized for the multi-rate model of Vidstrand et al. (2010) would be less effective. The result could be less effective attenuation of dilute glacial meltwaters than predicted by the model of Joyce et al. (2010).

Hence the matrix-diffusion model of Vidstrand et al. may give more conservative results for this case. This could be checked by extending the methodology outlined in Appendix F of Joyce et al. (2010) to the multi-rate case, and calculating the resulting breakthrough times for dilute waters to reach the same set of deposition holes.

However it should be borne in mind that the data support for the parameter values used by Vidstrand et al. (2010) is minimal; in particular, values for the intermediate coefficients α_i are purely a result of assuming that the fracture network on scales below that of the Hydro-DFN characterization is fractal. While there is some evidence in the scientific literature to support this assumption, including analyses of the TRUE experiments at the Äspö Hard Rock Laboratory (Haggerty, 1999), the applicability to time scales on the order of years to tens or hundreds of years is uncertain, and there is a lack of comparable site-specific experimental data from Forsmark.

4. Effects of boreholes

4.1. SKB's treatment of effects of boreholes

SKB's analysis recognizes the possibility that boreholes could provide additional paths for flow and transport within the repository volume, whether these result from incomplete or ineffective sealing of boreholes that were drilled as part of the site characterization program, or by future human intrusion.

SKB's treatment of the effects of boreholes on groundwater flow and flow-related performance measures has been reported in Sections 5.6 and 6.3.2 of Joyce et al. (2010, SKB 09-20), with further details given in Appendix G of the same report.

The approach is based on adding hypothetical boreholes to the repository-scale CONNECTFLOW model (Hydro-DFN plus backfilled tunnels), and calculating steady-state flows based on boundary conditions and density at 2000 AD, as for the hydrogeological base-case model of Joyce et al. (2010). A freshwater density was assigned to the entire borehole, as a conservative assumption in terms of hydraulic driving forces.

The boreholes are represented as thin, narrow "fractures" with a width and thickness of 0.08 m, equal to the diameter of standard Forsmark boreholes. An arbitrarily high value of hydraulic conductivity (0.1 m/s) was assigned to these "fractures." Joyce et al. (2010, p. 211) note that these properties were "chosen in order to make a good enough numerical representation of a borehole," but that appropriate values of these parameters are hard to define.

Five types of cases of interest were considered (Joyce et al., 2010, Table 5-4):

1. *The borehole intersects a deposition tunnel and creates a new flowing pathway to the surface. This is likely to be downstream of where a deformation zone intersects a deposition tunnel, but where the tunnel currently has no significant outflow.*

2. *The borehole intersects near a deposition tunnel and creates a new flowing pathway to the surface. This could be an intersection with a transmissive fracture that intersects a deposition tunnel, but does not intersect with anything else carrying a significant flow.*

3. *The borehole intersects a deposition tunnel but does not cause a significant effect on the flow. Perhaps there is no supply of flow in this tunnel or all the flow is already going into a transmissive feature.*

4. *The borehole intersects near a deposition tunnel but does not cause a significant effect on the flow. Perhaps it does not intersect anything very transmissive or it intersects something that is transmissive but is already carrying a significant flow so that the borehole doesn't make much difference.*

5. *The borehole intersects a canister position directly and creates a new flowing pathway to the surface.*

For practical reasons, in initial runs multiple candidate boreholes were modelled simultaneously in each of the three repository blocks (Figure 24). Once boreholes matching one of the above cases of interest were identified, these were modelled individually to avoid complications due to coupled effects between boreholes.

Beyond these five cases of interest, additional boreholes were considered to investigate the effect of having a borehole directly above a canister location and also to study the effect of placing a borehole in the area of discharge flow present in the south-west portion of the repository.

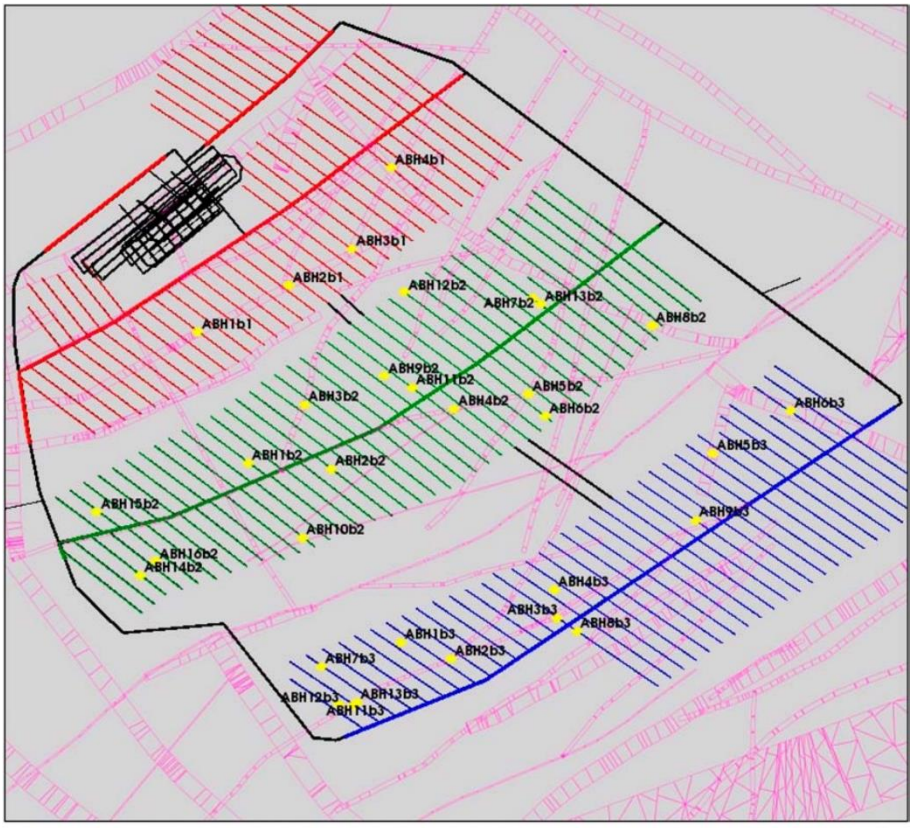

Figure 24: (from Joyce et al., 2010, Figure 5-5). Plan view of the repository with block 1 (red), block 2 (green) and block 3 (blue). The positions of the modelled boreholes are indicated using yellow markers. A horizontal slice through the HCD at elevation –455 m is shown in purple.

The results confirm that flow tends to be drawn into open boreholes, with particles being attracted to the borehole in all cases but one. Joyce et al. (2010, p. 114) summarize the results as follows: "In 16 out of the modelled 33 cases more than 5% of the released particles at some point enter the borehole. Eight cases have more than 10% of the particles entering the borehole and for one case as many as 23% of the released particles enter the borehole. "

However, the impact of open boreholes on performance measures is found to be minor. Performance measures generally are within 20% of the values obtained from the hydrogeological base case, with slight increases in initial Darcy flux and equivalent flow rate, and slight decreases in travel time, path length and F.

A stronger effect of up to a factor of 4 change in performance measures is observed in terms of the performance measures for just the particles that enter the boreholes (and thus represent the enhanced flow paths within the repository volume). These effects are illustrated by the CDF plots in Figure 25. These are non-normalized CDFs, meaning that the CDFs have not been adjusted to take account of the fraction of particles that fail to reach the model boundaries. Joyce et al. (2010) note that only the curve ABH5b3 shows a marked increase in U_r in comparison with the corresponding repository block from the base case. F_r decreases for all boreholes compared to the respective hydrogeological base case paths. This reduction is ascribed by Joyce et al. (2010) to the fact that the contribution from the borehole is not included in Fr, for particles that enter the borehole and thus bypass a portion of the rock.

The CDFs are somewhat difficult to interpret by inspection. Figure 26 gives an alternative presentation in terms of statistical measures for U_r and F_r of the particles that pass through the boreholes. Effects on U_r are at most half an order of magnitude. However it can be seen that the decrease in transport resistance for the repository blocks with the lowest F_r is more than an order of magnitude for ABH5b3 as compared with BC5b3, and nearly an order of magnitude for ABH9b3 as compared with BC9b3.

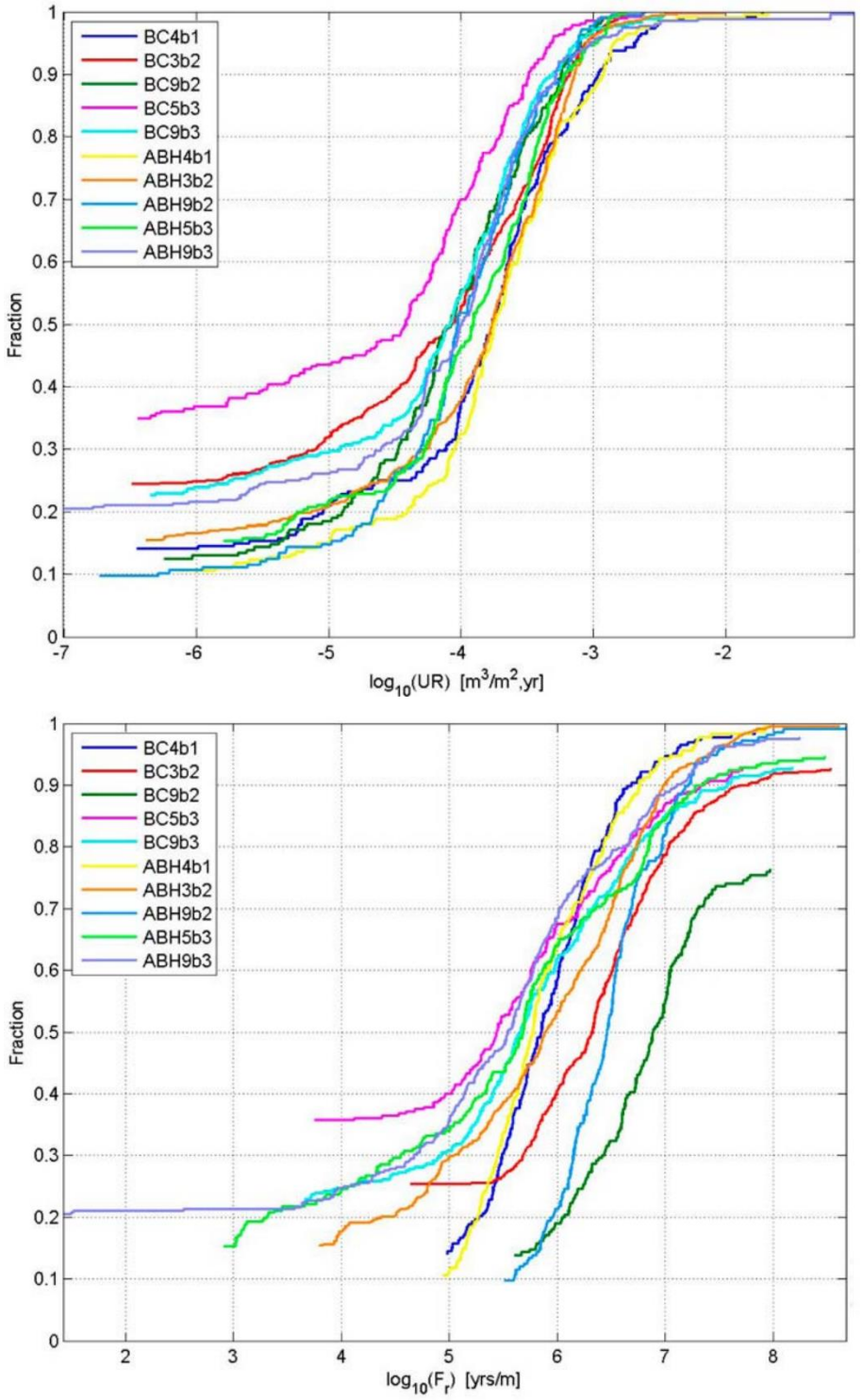

Figure 25: Non-normalized CDF plots of Ur (top) and Fr (bottom) for the repository blocks in the hydrogeological based case model (BC*b1 to BC*b3) and selected borehole cases (ABH*b*) for Q3 particles released at 2000 AD that enter the borehole and successfully reach the model top boundary. From Joyce (2010, Figures 6-37 and 6-38).

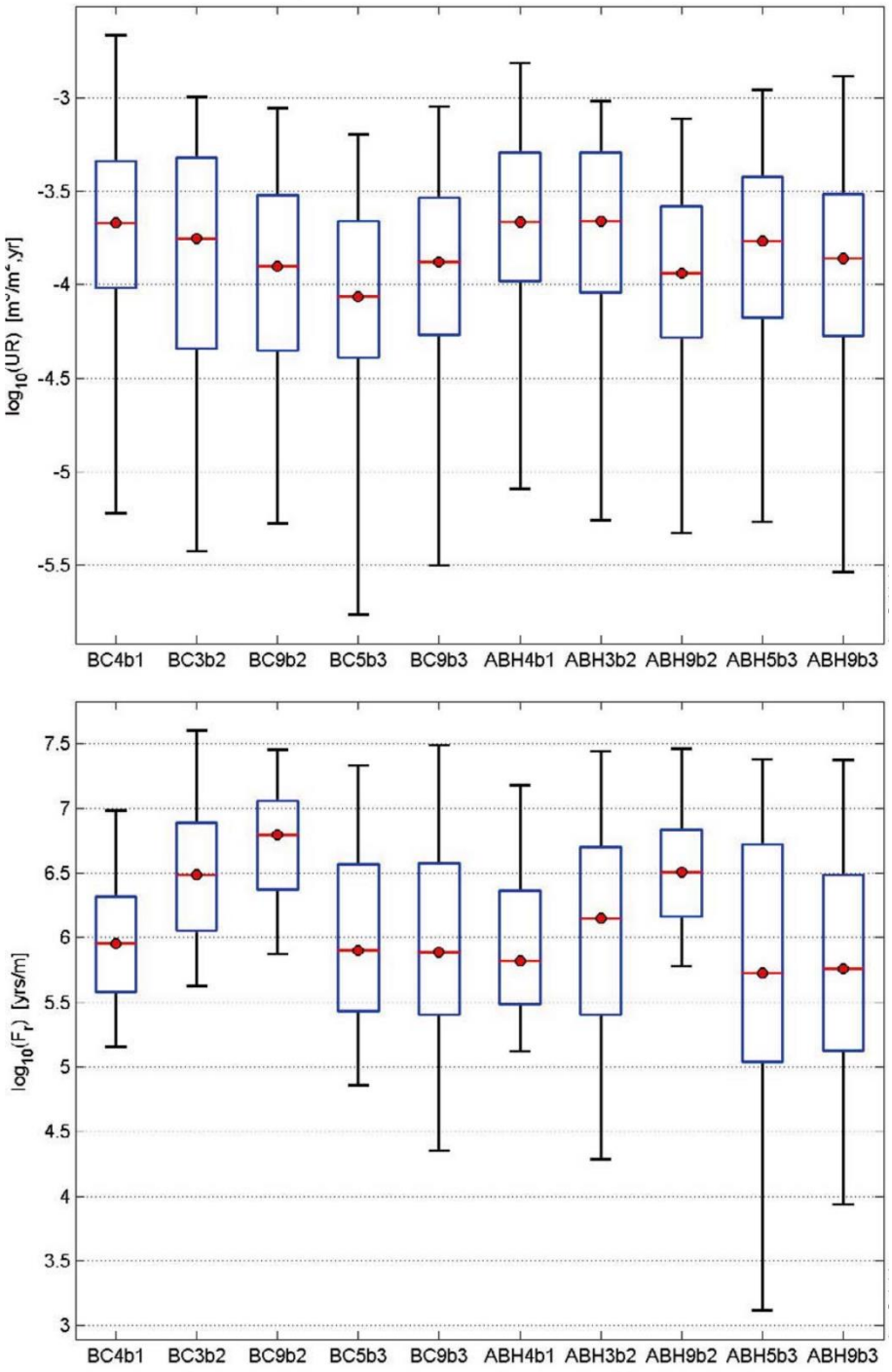

Figure 26: Bar and whisker plots of Ur (top) and Fr (bottom for the repository blocks in the hydrogeological based case model (BC*b1 to BC*b3) and selected borehole cases (ABH*b*) for Q3 particles released at 2000 AD that enter the borehole and successfully reach the model top boundary (from Joyce et al., 2010, Figures G-21 and G-19). The statistical measures are the median (red), 25th and 75th percentile (blue bar) and the 5th and 95th percentile (black "whiskers").

4.2. Motivation of the assessment

Boreholes that are left unsealed or are ineffectively sealed after site characterization and monitoring programmes, as well as boreholes that might be drilled during future human intrusion situations could hypothetically provide low-resistance pathways for groundwater flow and transport from the repository to the surface environment. The likely consequences of such boreholes therefore need to be considered among the scenarios for future release of radionuclides.

4.3. The consultant's assessment of borehole effects

The five cases of borehole locations considered are comprehensive, in terms of covering the main types of cases that could be envisioned for boreholes to enhance flow to deposition holes or to enhance transport of radionuclides.

However the number of boreholes modelled for each case (as listed in Table G-1 of Joyce et al., 2010) is small. The number of cases modelled for each type of case is as follows:

- Type 1 or 3: Intersection with a deposition tunnel: 13 cases
- Type 2 or 4: Intersection near a deposition tunnel: 12 cases
- Type 5: Direct intersection with canister position: 8 cases

Within these categories, no analysis has been provided of variables that could affect the impact, such as:

- Distance from a borehole-deposition hole intersection to the canister;
- Distance from a borehole-tunnel intersection to the nearest deposition hole;
- Distance from a borehole intersection with a fracture or fracture zone to the nearest deposition hole;
- Transmissivities of the intersected fractures or fracture zones; or
- Transmissivities of other fractures in the network that provide the most direct link from the intersected fracture or fracture zone and the nearest deposition holes.

It is doubtful that these parameters have been adequately sampled by such a small number of calculation cases.

Therefore the results can only be viewed as illustrative. While the modelling approach used embodies a high degree of realism in its treatment of repository geometry, a more stylized treatment based on a much simpler model could have been more effective for scoping the range of effects.

The analysis has not considered the potential effect boreholes that are larger in diameter than 0.08 m. Thus the modelled variants represent exploration technology similar to that used for Forsmark investigations, where the aim has been to minimize disturbance of the repository volume. A future exploration program for mineral resources could use larger-diameter boreholes or even enhanced drilling methods that lead to larger-diameter openings within the repository volume.

Coupled effects of two or more boreholes have not been analysed. Joyce et al. (2010) obtained results from such cases as a preliminary stage of modelling, but did not present the results. The main situation of interest would be if two boreholes combine to produce a U-tube type of enhanced flow path through a section of the repository.

Such a case seems unlikely as part of a future human intrusion scenario, but could arise from a common-mode failure of borehole sealing methods for site-investigation boreholes. As the locations of all surface-based boreholes that are planned for the repository are already known, it would have been most meaningful to assess this possibility based on the positions of actual site-investigation boreholes.

The representation of boreholes in the numerical model is an idealization as thin, narrow "fractures," with an arbitrarily high value of hydraulic conductivity (0.1 m/s) and unit porosity. These properties are not justified apart from a note by Joyce et al. (2010, p. 211) that these properties were "chosen in order to make a good enough numerical representation of a borehole." As noted by the same authors, a sensitivity study of these parameters would have been desirable since there seems to be no physical basis for the chosen values.

A further question not addressed by this analysis is the potential role of transport mechanisms other than laminar flow through the boreholes. Although the flowrates through unsealed boreholes would most likely be limited by the transmissivities of the fracture network and/or the hydraulic conductivities of the backfilled tunnels (depending on which are intercepted), so turbulent flow through the boreholes may not be an issue, convection-enhanced transport through the boreholes should perhaps be considered.

The stated overall conclusion: "*Including a borehole in the hydrogeological base case model does not have a major effect on the performance measures even if the groundwater flow pattern is affected and the flow paths of the released particles change*," seems to be overstated, considering the small number of cases modelled. At least one case yields more than 1.5 orders of reduction in the 5th percentile values of F_r.

In summary, the assessment of boreholes by Joyce et al. (2010) is impressive in terms of the degree of model complexity on multiple scales. However, the treatment of the boreholes themselves is highly idealized. The limited number of calculation cases means that some stochastic parameters of interest have not been fully investigated. A thorough study of the controlling parameters using simpler models could have helped to supplement these limited results, but such an analysis is lacking.

5. Thermal effects of waste on groundwater flow

5.1. SKB's treatment of thermal effects

Within SR-Site SKB did not evaluate the impact of thermal effects of spent nuclear fuel on groundwater flow. Table 3-1 of the SR-Site geosphere process report (SKB TR-10-48) states, "Impact of thermal effects of waste addressed in scoping calculations for SR-Can /Hartley et al., 2006a/. Effect negligible so not considered for SR-Site."

The accompanying text (SKB TR-10-48, p. 57) describes the expected thermal effects of spent fuel on groundwater flow as follows:

"The heat generated by the spent nuclear fuel would lead to a temperature perturbation that propagates out from the waste and ultimately falls off over time. The temperature perturbation would affect the groundwater viscosity and density, which would affect the groundwater flow. In particular, the variations in density would lead to buoyancy forces and convection cells would tend to form in the vicinity of the repository. "

The consequences of ignoring these thermal effects are described under the list of model simplification uncertainties (SKB TR-10-48, p. 68):

"Thermal effects are neglected in the calculations for the excavation, operation and resaturation period. This is considered to be a reasonable approximation because the effects of the temperature distribution on the drawdown and groundwater inflow to the repository, which are the key issues for this period, are relatively small. The effects of buoyancy-driven flow generated by the heat from the waste are not taken into account in the main calculations for the period after closure and repository resaturation. However, scoping calculations of the effects of the thermal buoyancy-driven flow are undertaken. This is considered an appropriate level of treatment, since there are not expected to be significant releases of radionuclides during the period when thermal effects are greatest. "

Justification for these statements is provided by reference to scoping calculations that were performed as part of the hydrogeological modelling for SR-Can (Hartley et al., 2006, Chapter 6).

These calculations were carried out using a continuum model for coupled groundwater flow and heat transport, neglecting the component of heat transport due to groundwater advection on the basis that conductive heat transport through the rock will dominate in such low-porosity, low-permeability rock.

The heat output from the spent fuel is represented as a uniformly distributed, rectangular source in the same approximate location as the repository. Thermal boundary conditions were fixed-temperature at the top of the model, a fixed uniform heat flux through the base of the model consistent with the local geothermal gradient, and no heat flux across the vertical boundaries.

Initial conditions for the flow field are taken from steady-state flow simulations in the base case model that neglects thermal effects, for boundary conditions applicable at 2020 AD. The time at which heat output from spent fuel begins is not clearly stated but apparently this begins at 2020 AD, uniformly throughout the entire area of the repository.

Results for two different hydraulic conductivity fields were presented by Hartley et al. (2006):

- A continuum porous medium (CPM) case in which the hydraulic conductivity is considered to be uniform throughout each rock domain (apart from the effects of deterministic fracture zones which are themselves represented as uniformly transmissive), and
- An equivalent-continuum porous medium (ECPM) case in which the hydraulic properties of each grid block within a given rock domain is calculated by upscaling from a DFN realization.

The authors regard the ECPM case as more realistic but note that the CPM case allows for easier interpretation of results due to the more homogeneous hydraulic conductivity field.

A comparison of vertical Darcy velocities for the CPM model with and without thermal effects (Figure 27) shows that thermal effects have a significant impact on the flow near the repository, and that this persists for hundreds of years.

Hartley et al. (2006) remark that the resulting flow is of a similar magnitude to the flow calculated without taking thermal effects into consideration. This is borne out by comparison of the "thermal" curves with the corresponding curves for most depth levels. However it appears that for the levels closest to the repository (z = -500 m, -450 m, and -400 m) it appears that the increase can be an order of magnitude or more in comparison with the very low vertical flows that are predicted for the model without thermal effects.

Hartley et al. (2006) note the development of downward flows in the rock below the repository, in the thermal case. This is explained by the effects of thermal expansion of water in the relatively large pore volume of the repository, which results in flow in all directions outward from the repository during the first 100 years. However after 100 years the thermal buoyancy effects become dominant, yielding a generally upward-directed flow field. In spite of the thermal buoyancy effects, the CPM model predicts very little up-coning of saline waters from below the repository

Particle tracking based on the calculated flow fields indicated that thermal effects influenced transport routes in the vicinity of the repository, but that discharge locations were not significantly different. Hartley et al. (2006) ascribe this to the controlling influence of surface topography and sea level.

The impact of thermal effects on travel times for particles released from the repository is a function of the time of release, because of the temporally evolving temperature and flow fields. The greatest impact predicted by the CPM model is for path lines starting shortly after repository closure; for such path lines the median travel time is reduced by more than an order of magnitude (Figure 28). However for later release times, the CPM model predicts longer median travel times compared with the steady-state case without thermal effects.

From Figure 28 it can also be seen (although not noted by the authors) that the variability of travel times is increased when thermal effects are present, and that the 5th percentile values are reduced even up to 1000 years after the start of the thermal perturbation.

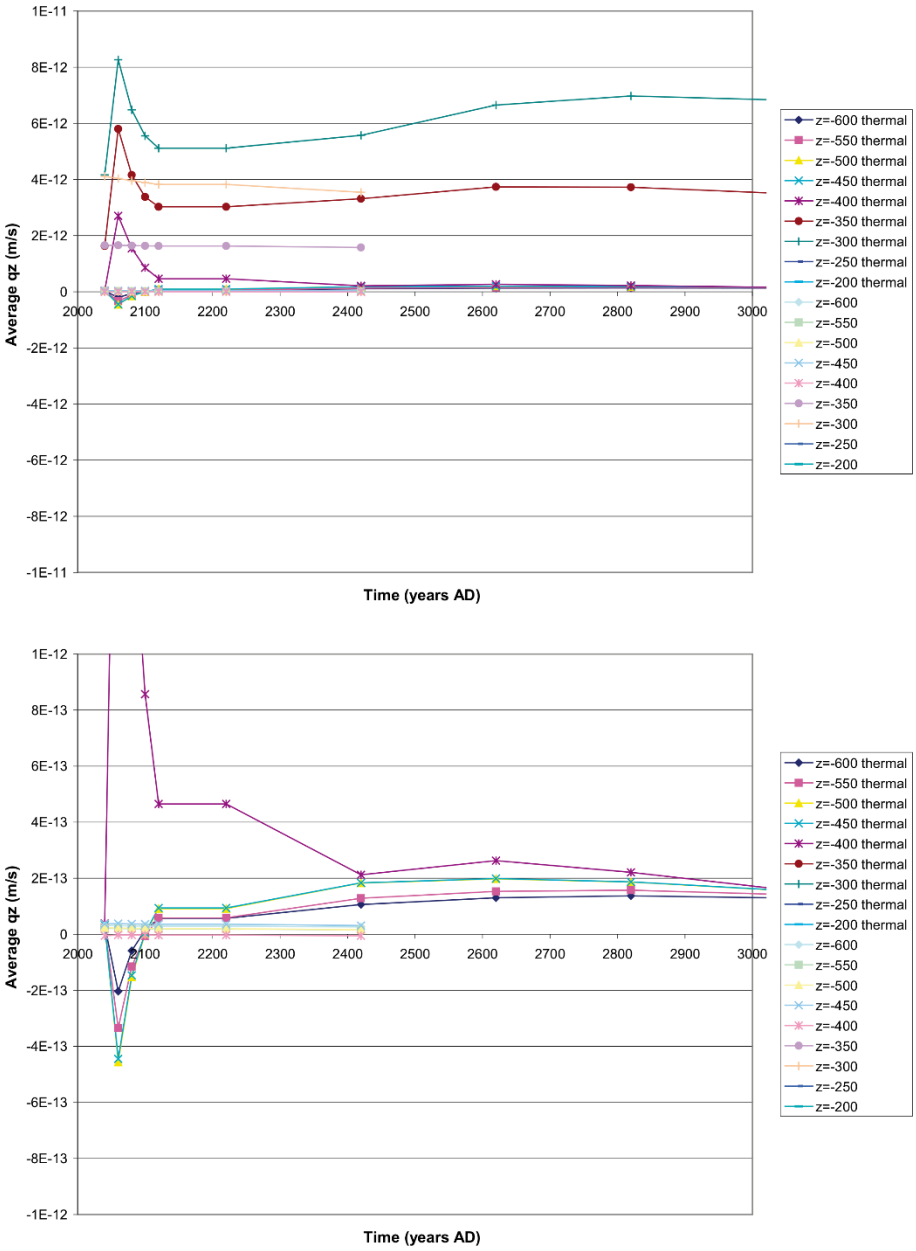

Figure 27: Comparison of the evolution of the average vertical Darcy velocity q_z with and without consideration of thermal effects of the spent fuel, based on flows calculated in the CPM model for grids of points at several horizontal levels directly above and below the repository. Top: variations on a scale from -10^{-11} to 10^{-11} m/s. Bottom: variations on a scale from -10^{-12} to 10^{-12} m/s. From Figure 6-10 of Hartley et al. (2006).

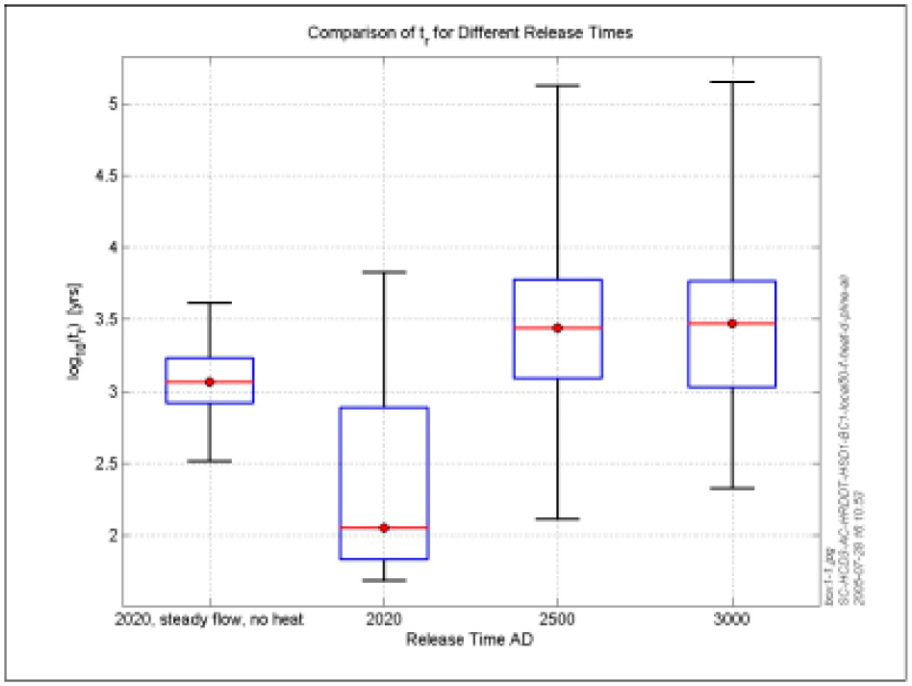

Figure 28: Box-and-whisker plot of distributions of travel time for particles released at different times from the thermally-affected CPM model, as compared with the results for a steady-state flow field with no thermal effects. Red lines indicate median values; blue boxes show the range of 25th and 75th percentiles, and black whiskers represent the 5th and 95th percentiles. From Hartley et al. (2006, Figure 6-15).

For the ECPM calculation case which embodies a more heterogeneous hydraulic conductivity field, the vertical Darcy velocities for the CPM model with and without thermal effects (Figure 29) show similar long-term influence of thermal effects on on the flows at z = -350 m or shallower. However, the short-term flows driven by thermal expansion effects are not evident as they were for the CPM case.

Hartley et al. (2006) suggest that the lack of strong short-term thermal-expansion driven flows in the ECPM is because this model has much higher permeability around the repository compared with the CPM, and hence accommodates larger flows. Hence the early time period in which the thermal-expansion driven flow would be apparent is shorter than the time step used.

Discharge locations for the ECPM case are generally similar to those for the CPM model, due to the controlling influence of topography and sea level.

In terms of travel times, as summarized in Figure 30 thermal effects produce a reduction in median travel time for path lines, even for particles released immediately after the repository closure date simulated by this model (2020 AD). In contrast to the CPM case, the greatest impact in the ECPM case occurs for path lines starting at 2500 AD.

Hartley et al. (2006, p. 266) conclude that thermal effects can potentially have a moderate impact on groundwater flow and transport from a repository, and note that the potential effects are greatest for radionuclides that are released shortly after repository closure, which can be considered very unlikely. They suggest that the most important effects of heat from the spent fuel might be in terms of groundwater viscosity near the repository, which could be reduced by a about a factor of two for many thousands of years, and suggest that this effect "possibly ought to be taken into account in the PA transport calculations. "

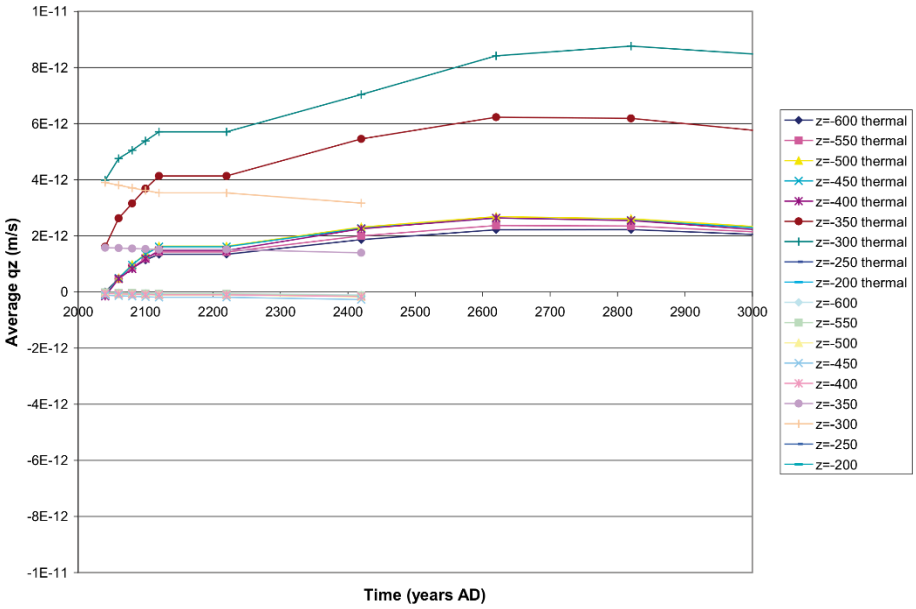

Figure 29: Comparison of the evolution of the average vertical Darcy velocity q_z with and without consideration of thermal effects of the spent fuel, based on flows calculated in the ECPM model for grids of points at several horizontal levels directly above and below the repository. From Figure 6-20 of Hartley et al. (2006).

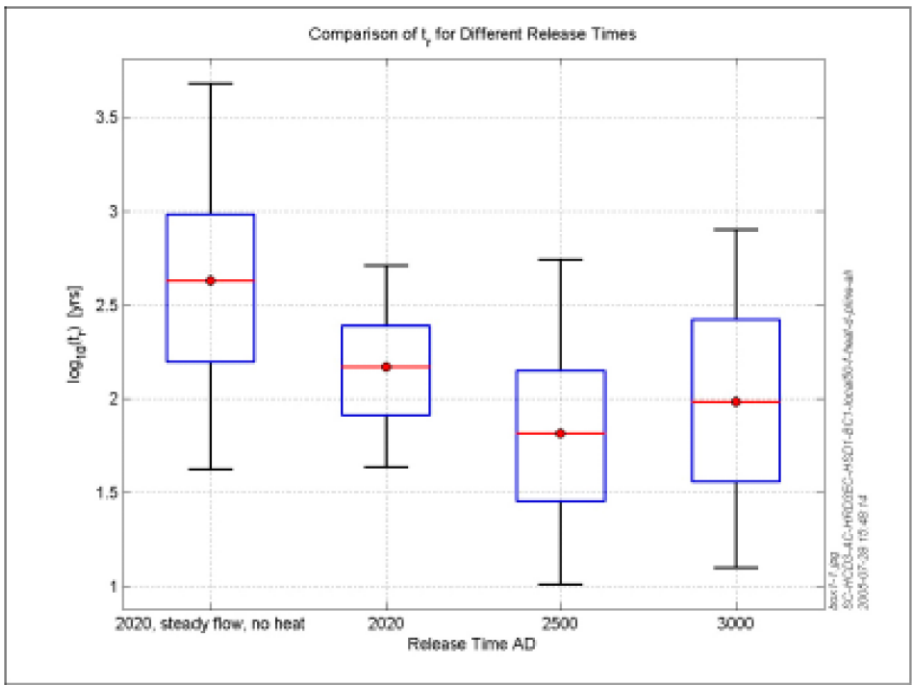

Figure 30: Box-and-whisker plot of distributions of travel time for particles released at different times from the thermally-affected ECPM model, as compared with the results for a steady-state flow field with no thermal effects. Red lines indicate median values; blue boxes show the range of 25th and 75th percentiles, and black whiskers represent the 5th and 95th percentiles. From Hartley et al. (2006, Figure 6-23).

However, Hartley et al. (2006) also note that thermal effects would be reduced in a transport model that takes account of the long times that radionuclides could spend in repository tunnels, while the heat source decays. The processes of sorption and rock-matrix diffusion would also tend to retard radionuclide migration during the thermally-affected period.

5.2. Motivation of the assessment

Thermal effects on groundwater flow have not been quantitatively evaluated as part of SKB's safety assessment. It can be expected that both thermal buoyancy and thermal reduction of water viscosity will enhance upward flow from the repository horizon, leading to faster travel times and lower transport resistance. Thus it is not obvious that SKB's decision to neglect thermal effects on groundwater flow is conservative. This assessment focuses on the questions of whether (1) the cited study by Hartley et al. (2006) is sufficient to scope the hydrogeological consequences, particularly flow-related performance measures, and (2) whether the consequence of neglecting thermal effects could be significant in consideration for the safety case.

5.3. The consultant's assessment

The scoping evaluation of thermal effects on flow by Hartley et al. (2006) is based on a continuum representation, but otherwise represents the main physical processes of concern (conductive heat transfer, effects of temperature on groundwater properties, density-dependent groundwater flow, and effects of flow on the evolution of salinity).

The processes of heat transfer and groundwater flow are not fully coupled in the model: Heat affects groundwater flow but groundwater flow is not considered to carry heat by advection. The consequences of this simplification as well as the use of a continuum representation are assessed below.

5.3.1. Convective heat transport by groundwater

The argument given by Hartley et al. (2006) for excluding the role of convective heat transport due to the low permeability and hence low fluid velocities is reasonable, at least within the framework of the continuum representation.

This can be seen simply by considering the maximum vertical heat flux that could be carried by groundwater heated close to 100ºC and moving through the bedrock at a rate equal to the calculated vertical component of Darcy flux:

$\phi_z = (\rho_w c_w \Delta T) q_z$

where:

ρ_w = density of water ≈ 1000 kg/m^3

c_w = specific heat capacity of liquid water ≈ 4200 K/(kg·K/m^3)

ΔT = temperature of water above ambient at repository depth

For ΔT = (100ºC – 15ºC) = 85ºC or 85 K and a vertical Darcy flux $q_z = 10^{-12}$ m/s, these values yield a maximum vertical heat flux of 3.6×10^{-4} W/m^2.

This is two orders of magnitude less than the geothermal gradient of 3.4×10^{-2} W/m^2 that has been considered in the model, which in turn is seen (from the results of the model) to be minor in comparison with the conductive heat flux through the rock from the repository. Thus the effects of heat transport by groundwater advection are minor within the context of this type of model.

5.3.2. Consequences of continuum representation

The use of a continuum representation of the bedrock by Hartley et al. (2006) is an understandable simplification for a scoping assessment, considering the mathematical and numerical difficulties of representing even weakly coupled groundwater, heat, and salinity evolution in a fracture network model. However, some consequences of the continuum representation need to be recognized in assessing the results.

First, equivalent continuum models (whether CPM or ECPM) generally yield much less heterogeneous flow fields than the corresponding discrete-fracture-network (DFN) models. This difference as observed in simpler models would presumably carry over into models that take account of thermal effects, if such models were available.

Buoyancy caused by thermal effects essentially affects the potential gradient that drives flow, whether through a DFN or a ECPM/CPM. In either type of model, the influence of potential gradient on flow is linear. Considering just this aspect of thermally-affected flow, the differences in flow between ECPM and DFN representations for the thermal case should be the same (both in terms of magnitude and variability) to those between ECPM and DFN representations for the simpler case where thermal effects are neglected.

Temperature increases caused by heating result in a reduction in the viscosity of water. As noted by Hartley et al. (2006), the temperature changes are sufficient to produce a long-term reduction of viscosity by about a factor of 2, even after 4000 years In both ECPM and DFN representations, flows and fluid velocities are inversely proportional to fluid viscosity. Hence it should be expected that accounting for thermal effects would result in about a factor of two enhancement of long-term flowrates, throughout the temperate period.

On shorter time scales of one or two centuries after closure, significantly higher temperatures and correspondingly lower viscosities can be expected to develop in the rock around the repository. Thus in early post-closure time, a factor of 2 increase in flows might not be fully conservative for assessing, for example, early post-closure erosion of the buffer. However, considering that the temperatures at repository depth are initially above 10°C and should remain below 100°C, corresponding to a dynamic viscosity range of about 1.2 cP to 0.3 cP, the maximum reduction in viscosity should be no more than a factor of 4. Thus a very conservative estimate of the effect of viscosity reduction on flows would be a factor of 4.

More complex effects on flow in a DFN could be expected from persistence of high fluid temperatures (and hence lower viscosities) along portions of the discrete network that carry most of the flow away from the repository. Thus the extreme (high) values of flow could become more exaggerated relative to median values.

When the fluid flux is concentrated through a smaller portion of the rock, the local convective thermal flux carried by groundwater could also become more significant, with the result that water flow and heat transport become more fully coupled.

The magnitude of these effects could be scoped by modelling fully coupled water flow and heat transport through a single vertical fracture with outward diffusion of heat into the wall rock, with temperature-dependent fluid viscosity and using rock thermal properties representative of the Forsmark repository volume, and considering a range of fracture hydraulic apertures. SKB has not presented any such calculations in the reports considered for this review. Further development and application of such a model for the case of a vertical fracture was not possible within the scope of this review.

The consequences of a DFN representation for the flow field will likely be accentuated when transport of radionuclides is considered. In the ECPM model of Hartley et al. (2006), particle tracking based on the calculated flow fields indicated that thermal effects influenced transport routes in the vicinity of the repository, but that discharge locations were not significantly different, due to the controlling influence of surface topography and sea level in a continuum model. However, in a discrete network the flow field is more constrained by connections through the sparse network. Furthermore, the preferred paths for transport may switch in a

temporally evolving flow field. Therefore the conclusions of Hartley et al. (2006) on insensitivity of discharge locations to thermal effects may not be reliable for a discrete representation.

For the purposes of SR-Site, given the apparent low sensitivity of overall risk to the biosphere, it seems doubtful that path-switching phenomena and their effect on discharge locations would significantly alter the main conclusions. Of greater concern is the possibility that discrete pathways with relatively low transport resistance could be enhanced by thermal effects on the flow field.

One phenomenon of possible concern is water viscosity reduction due to increased temperatures in the fractures that intersect deposition holes. A decrease in viscosity due to temperature has an inverse effect on the effective transmissivity of the fracture. This is mainly of concern for fractures that have low transmissivity (at normal in-situ groundwater temperatures) relative to the fractures that they connect between, and thus act as "bottlenecks" in the flow system. For such "tight" fractures a reduction in local viscosity could result in a net increase in flow. For other fractures, the effects of viscosity reduction on flow around or through the deposition hole are limited by the tighter fractures elsewhere along the flow path.

This effect may to some extent be mitigated if liquid water is driven away from the deposition hole during the period of significant thermal effects of spent-fuel storage, resulting in an unsaturated zone around the deposition holes during the period of most elevated temperatures.

6. The Consultant's overall assessment

6.1. Assessment of flow-related performance measures

The simple series-conductor model developed here gives reasonably conservative estimates of performance parameters, as summarized in Tables 5 and 6. A caveat is that these estimates are predicated on SKB's derivation of hydrogeological DFN model parameters, although a range of variants have been considered.

The results are substantially in agreement with the calculations performed by SKB, using much more complex models. Considering the assumptions of the simple series-conductor model, the performance measures from the simple model are almost entirely determined by the size and transmissivity of the first fracture to intersect a given deposition hole, and then an assumption of a connection to the nearest HCD via large-scale fractures. The similarity with SKB's results suggest that the performance measures produced by SKB's models are strongly determined by the same factors that govern the simple model.

This gives confidence that the basic performance of the hydrogeological system inferred by SKB can be understood without resort to complicated models. At the same time, it raises concerns that the real system may be more complex than the interpretation that has resulted from calibration of a model based on an assumption of a DFN in which flow takes place uniformly across the width of fractures, rather than through discrete channels.

If SKB's conceptualization of the rock mass as an unchannelized DFN is assumed to be correct, then their conclusions regarding performance measures for future temperate and glacial climates appear to be reasonably conservative. SKB have omitted contributions of the CPM and ECPM portions of their models from calculations of performance measures, which is appropriate because the porosity and flow-wetted surface values upscaled from the DFN model in the ECPM are not conservative, and should not be relied upon.

SKB's U_r values are barely sensitive to the time of release for the temperate period. F_r values a marginally higher for release times after 5000 AD, due to shoreline retreat and longer travel times in the rock. Higher values of U_r and lower values of F_r are expected during the glacial period as a consequence of steeper hydraulic gradients. While the simple series-conductor model has not been applied explicitly to glacial situations, the consequences of steeper hydraulic gradients can be calculated directly by scaling with respect to the anticipated gradients.

The simple model results as presented here are only for deposition holes that would be accepted based on the full-perimeter criterion (FPC), but include holes that would be rejected based on the extended criterion (EFPC). These holes have been identified in the detailed data deliveries to permit further analysis for the effects of EFPC on consequence assessment.

The main effects of the OSM-TFM and TCM alternative Geo-DFN models are in terms of the number of deposition holes that connect to transport pathways for area-based scaling. The TCM and OSM-TFM models both produce more intersections with deposition holes. In terms of the cumulative density functions of performance parameters, the results for the OSM-TFM and TCM alternatives are practically identical to the results for the r_0-fixed alternative.

The area-scaled estimates can best be viewed as a bounding case for upscaling from of the linear frequency of hydraulic conductors intercepted by small-diameter boreholes, to the number of conductors that would be intersected by deposition holes in a strongly channelized system. The results obtained are extreme, as effectively all deposition holes end up being hydraulically connected. This result seems unlikely but the degree of channelization has not been well characterized by SKB's site-characterization programme so far.

Considering on one hand the possibility of strong channelling of a DFN, and on the other hand the alternative concept of a sparse channel network, it should be recognized that there is considerable uncertainty in the number of deposition holes that will be connected to significant flow paths. This uncertainty may remain until detailed data are obtained from underground for a wider range of scales.

6.2. Salinity and penetration of dilute waters

SKB's models for salinity evolution models are subject to uncertainties regarding the initial state (in terms of distribution of reference waters) as well as the extent to which the matrix is accessible for diffusion on the relevant range of time scales for modeling future glacial cycles.

The models are highly sophisticated in terms of their mathematical development, but their reliability for safety-assessment purposes is ultimately constrained by the limited amount of hydrogeochemical data from relevant depths, the dearth of sufficiently long-term tracer tests from the Forsmark site to constrain possibilities for matrix-diffusion models, and the at best modest match of model predictions to observed groundwater compositions.

However, the models can be regarded as reasonable given the current level of data support. Generally SKB's approach to calculating the risk of dilute waters penetrating to deposition holes is based on conservative assumptions. The models do not take credit for other rock-water interactions that could be expected to attenuate penetration of very dilute waters, and they assume zero initial salinity of the melt waters. Steady-state flow fields are used for the main quantitative predictions.

The semi-analytical approach used by Joyce et al. (2010) for calculating breakthrough times for dilute waters uses values of transport resistance F and advective travel times t_w that are conservative, in that they neglect any contribution from the portions of the model that are represented as a continuum. This is a sensible degree of conservatism, in view of the non-conservative methods that are used to upscale porosity and flow-wetted surface for ECPM blocks.

One possibly non-conservative assumption in the dilution calculations by Joyce et al. (2010) is that the entire matrix between transmissive fractures is regarded as accessible for matrix diffusion. A more conservative assumption would be that matrix diffusion depths are more limited, and possibly heterogeneous.

The multi-rate matrix diffusion model used by Vidstrand et al. (2010) must be regarded as hypothetical as it is mainly based on assumptions of fractal scaling of the immobile zones of varying rate coefficients for mass transfer, with limited data support. However it could be more conservative than the single-rate model used by Joyce et al. (2010) to calculate dilute water penetration times, particularly on the intermediate time scales that are of interest for situations where an ice front is located above the site. A reanalysis of the results of Joyce et al. (2010) based on the multi-rate model of Vidstrand et al. (2010) is therefore recommended.

The model of Joyce et al. (2010) assumes that the entire matrix up to 12.5 m from the nearest fracture that participates in the site-scale flow network is uniformly accessible for matrix diffusion. Evidence for matrix diffusion on this scale is lacking. Furthermore, the model does not consider the possibilities that the spacing of fractures that participate in the site-scale flow network, based on PFL anomalies, may be overestimated both due to convergent flow effects around boreholes, and very strong directional sampling bias for boreholes at depth. PFL measurements in near-vertical boreholes mainly sample subhorizontal fractures, while the properties sub-vertical fractures are of greater interest for assessing time scales for dilute water infiltration.

6.3. Effects of boreholes

SKB's analysis of borehole effects covers the main types of cases that could be envisioned for boreholes to enhance flow to deposition holes or to enhance transport of radionuclides. However the number of boreholes modelled for each case (as listed in Table G-1 of Joyce et al., 2010) is very small.

Within these categories, no analysis has been provided of variables that could affect the impact, such as:

- Distance from a borehole-deposition hole intersection to the canister;
- Distance from a borehole-tunnel intersection to the nearest deposition hole;
- Distance from a borehole intersection with a fracture or fracture zone to the nearest deposition hole;
- Transmissivities of the intersected fractures or fracture zones; or
- Transmissivities of other fractures in the network that provide the most direct link from the intersected fracture or fracture zone and the nearest deposition holes.

It is doubtful that these parameters have been adequately sampled by such a small number of calculation cases. Therefore the results can only be viewed as illustrative. A more stylized treatment based on a much simpler model would be more effective for scoping the range of effects.

The occurrence of unsealed boreholes is treated as a hydrogeological variant in SR-Site, rather than as part of the risk assessment. The adequacy of SKB's treatment will need to be assessed in terms of its adequacy as an illustrative scenario. The analysis by SKB could be viewed as a reasonable level of effort for a low-probability scenario, at this stage of the licensing process, although it has not been fully developed as a scenario.

Coupled effects of two or more boreholes have not been analysed. Joyce et al. (2010) obtained results from such cases as a preliminary stage of modelling, but did not present the results. It would be reasonable for SSM to request these results, to check if these limited simulations produced any examples of situations in which two boreholes combine to produce a U-tube type of enhanced flow path through a section of the repository.

Such a case seems unlikely as part of a future human intrusion scenario, but could arise from a common-mode failure of borehole sealing methods. As the locations of all surface-based boreholes that are planned for the repository are already known, it

would have been most meaningful to assess this possibility based on the positions of actual site-investigation boreholes.

A sensitivity study of the parameters used to describe boreholes would have been desirable since there seems to be no physical basis for the chosen values. In addition, there should be an analysis of the possibility of convection-enhanced transport through the boreholes.

6.4. Thermal effects of waste on flow

The scoping evaluation of thermal effects on flow by Hartley et al. (2006) is limited by the use of a continuum representation, and in that the processes of heat transfer and groundwater flow are not fully coupled in the model: Heat affects groundwater flow but groundwater flow is not considered to carry heat by advection.

The argument given by Hartley et al. (2006) for excluding the role of convective heat transport due to the low permeability and hence low fluid velocities is reasonable, at least within the framework of the continuum representation. However some consequences of the continuum representation need to be recognized in assessing the results.

Equivalent continuum models (whether CPM or ECPM) generally yield much less heterogeneous flow fields than the corresponding discrete-fracture-network (DFN) models. This difference as observed in simpler models would presumably carry over into models that take account of thermal effects, if such models were available.

Temperature increases caused by heating, leading to a reduction in the viscosity of water, could result in a factor of two enhancement of long-term flowrates, for at least the first 1000 years of the temperate period. A more conservative estimate of the effect of viscosity reduction on flows would be a factor of four.

More complex effects on flow in a DFN could be expected from persistence of high fluid temperatures (and hence lower viscosities) along portions of the discrete network that carry most of the flow away from the repository. The magnitude of these effects could be scoped by modelling fully coupled water flow and heat transport through a single vertical fracture with outward diffusion of heat into the wall rock, with temperature-dependent fluid viscosity and using rock thermal properties representative of the Forsmark repository volume, and considering a range of fracture hydraulic apertures. However it seems unlikely that this will result in significant enough effects to challenge SKB's conclusion that thermal effects can be neglected, especially if desaturation of fractures around deposition holes during the thermal post-closure period is taken into account.

The conclusions of Hartley et al. (2006) on insensitivity of discharge locations to thermal effects may not be reliable for a discrete representation. For the purposes of SR-Site, given the apparent low sensitivity of overall risk to the biosphere, it seems doubtful that path-switching phenomena and their effect on discharge locations would significantly alter the main conclusions.

7. References

Aho, A.V., Kernighan, B.W., and Weinberger, P.J., 1988. The AWK Programming Language. Addison-Wesley, 1988. ISBN 0-201-07981-X.

Bath, A., 2014. Groundwater salinity evolution and dilute water infiltration to repository depth. SSM Technical Note 2014:47, Swedish Radiation Safety Authority, Stockholm.

Black, J.H., 2012. Selective review of the hydrogeological aspects of SR-Site. SSM Technical Note 2012:37, Swedish Radiation Safety Authority, Stockholm.

Black, J.H., Barker, J.A., and Woodman, N.D., 2007. An investigation of 'sparse channel networks'. Characteristic behaviours and their causes. SKB Report R-07-35. Swedish Nuclear Fuel and Waste Management Co., Stockholm.

Dershowitz, W., Winberg, A., Hermanson, J., Byegård, J., Tullborg, E-L., Andersson, P., and Mazurek, M., 2003. Äspö Task Force on modeling of groundwater flow and transport of solutes. Task 6c: A semi-synthetic model of block scale conductive structures at the Äspö HRL. International Progress Report IPR-03-13, Swedish Nuclear Fuel and Waste Management Co., Stockholm.

Fox, A., La Pointe, P., Hermanson, J., and Öhman, J., 2007. Statistical geological discrete fracture network model. Forsmark modelling stage 2.2. SKB R-07-46, Swedish Nuclear Fuel and Waste Management Co., Stockholm.

Follin, S., 2008. Bedrock hydrogeology Forsmark. Site descriptive modelling, SDM-Site Forsmark. SKB Report R-08-95, Swedish Nuclear Fuel and Waste Management Co., Stockholm.

Follin, S., Johansson, P-O., Hartley, L., Jackson, P., Roberts, D., and Marsic, N., 2007. Hydrogeological conceptual model development and numerical modelling using CONNECTFLOW, Forsmark modelling stage 2.2. SKB Report R-07-49, Swedish Nuclear Fuel and Waste Management Co., Stockholm.

Geier, J., 2010. Discrete-feature model implementation of SDM-Site Forsmark. SSM Report 2010:05, Swedish Radiation Safety Authority, Stockholm.

Geier, J., 2014. Independent evaluation of the number of critical canister positions in the KBS-3 repository at Forsmark – Main Review Phase. SSM Technical Note 2014:44, Swedish Radiation Safety Authority, Stockholm.

Haggerty, R., 1999. Application of the multirate diffusion approach in tracer test studies at Äspö HRL. SKB Report R-99-62, Swedish Nuclear Fuel and Waste Management Co., Stockholm.

Haggerty, R., and Gorelick, S. M., 1995. Multiple-rate mass transfer for modeling diffusion and surface reactions in media with pore-scale heterogeneity. Water Resources Research, vol. 31, pp 2383–2400.

Hartley, L., Hoch, A., Jackson, P., Joyce, S., McCarthy, R., Rodwell, W., Swift, B., and Marsic, N., 2006. Groundwater flow and transport modelling during the

temperate period for the SR-Can assessment . Forsmark area – version 1.2 . SKB Report R-06-98, Swedish Nuclear Fuel and Waste Management Co., Stockholm.

Hjerne, C., Nordqvist, R. and Harrström, J., 2010. Compilation and analyses of results from cross-hole tracer tests with conservative tracers. SKB Report R-09-28, Swedish Nuclear Fuel and Waste Management Co., Stockholm.

Joyce, S., Simpson, T., Hartley, L., Applegate, D., Hoek, J., Jackson, P., Swan, D., Marsic, N. and Follin, S. 2010. Groundwater flow modelling of periods with temperate climate conditions – Forsmark. Report R-09-20, Swedish Nuclear Fuel and Waste Management Co., Stockholm.

Munier R, 2006. Using observations in deposition tunnels to avoid intersections with critical fractures in deposition holes. SKB R-06-54, Swedish Nuclear Fuel and Waste Management Co., Stockholm.

Munier, R., 2010. Full perimeter intersection criteria. Definitions and implementations in SR-Site. SKB Technical Report TR-10-21, Swedish Nuclear Fuel and Waste Management Co., Stockholm.

SKB, 2008. Site description of Forsmark at completion of the site investigation phase. SKB Technical Report TR-08-05. Swedish Nuclear Fuel and Waste Management Co., Stockholm.

SKB, 2009. Underground Design Forsmark Layout D2. SKB Report R-08-116. Swedish Nuclear Fuel and Waste Management Co., Stockholm.

SKB, 2010. Geosphere process report for the safety assessment SR-Site. Swedish Nuclear Fuel and Waste Management Co., Stockholm.

SKB, 2011. Long-term safety for the final repository for spent nuclear fuel at Forsmark. Main Report of the SR-Site project. SKB Technical Report TR-11-01. Swedish Nuclear Fuel and Waste Management Co., Stockholm.

Svensson, U., Ferry, M., and Kuylenstierna, H-O., 2010. DarcyTools, Version 3.4. Concepts, methods, and equations. SKB R-07-38, Swedish Nuclear Fuel and Waste Management Co., Stockholm.

Vidstrand, P., Follin, S. and Zugec, N. 2010. Groundwater flow modelling of periods with periglacial and glacial climate conditions – Forsmark. Report R-09-21, Swedish Nuclear Fuel and Waste Management Company (SKB), Stockholm.

APPENDIX 1

Coverage of SKB reports

Table 1: SKB reports considered in the present calculations.

Reviewed report	Reviewed sections	Comments
SKB TR-11-01	10.4, 12.1, 12.2	Focus on scenarios that could result in buffer erosion.
SKB TR-10-48 Geosphere process report	Table 3-1 and accompanying discussions	Focus on arguments for not evaluating thermal effects of waste on groundwater flow.
SKB R-06-98	Background	Justification for temperate period flow models.
SKB R-09-20	All with additional focus on Appendix F.	Main reference for analysis of dilute water penetration.
SKB R-07-38	Sections 3, 4, and appendices.	Focus on implementation of multi-rate matrix diffusion model.
SKB R-09-21	All	Main model for salinity evolution during periglacial and glacial periods.
SKB R-09-28	Aperture relationships	
SKB R-07-46	Overview	Background information for assessment of how DFN model implemented.
SKB TR-10-21	Background only	Definition of EFPC and FPC.
SKB R-06-54	Background only	Definition of FPC.
SKB R-99-62	Background only	Overview to consider implications and experimental evidence for multi-rate matrix diffusion model.

Model setup and scripts

A2.1 Calculation of distances from fracture-deposition hole intersections for deformation zones

The Linux C shell script SRHCD_calcdists_v1 was used to set up and run the following DFM module:

> *pancalc* (version 2.4.1.1, executable pancalc2411 compiled February 17, 2014)

to find the 3D distance from each fracture-deposition hole intersection (as listed in the fxd file for the calculation case and realization) to each of 18 deformation zones that are considered as HCDs in the site-scale model.

Execution of this script for the r_0-fixed Geo-DFN model was automated by the following commands (contained in the script calc_distances_all_r3):

```
foreach CASE ( r3 )
    foreach N ( 01 02 03 04 05 06 07 08 09 10 )
      SRHCD_calcdists_v1 $CASE $N
   end
end
```

Execution of this script for the TCM and OSM-TFM Geo-DFN alternatives was produced by the commands (contained in the script calc_distances_all_t2_o3):

```
foreach CASE ( t2 o3 )
   foreach N ( 01 02 03 04 05 06 07 08 09 10 )
      SRHCD_calcdists_v1 $CASE $N
   end
end
```

The main script SRHCD_calcdists_v1 is listed below, followed by three subordinate scripts:

> condense_fxd.awk
> extract_distances.awk
> append_distances.awk

which are written in the AWK programming language (Aho et al., 1988).

SRHCD_calcdists_v1

```
#!/bin/csh -f
 nohup
 if( "blank$2" == "blank" ) then
    echo "Syntax: SRHCD_calcdists_v1 opt seed"
    echo "where"
    echo "   opt = v1|..."
    echo "   seed= 01,02,..."
    exit
```

```
 endif
 set SRC  = "../../FMcrit_repo3"
 set STEM = "SRGeoPFC_${1}_${2}"
 set FXD  = "$SRC/${STEM}.fxd"
 if ( -f $FXD ) then
    awk -f condense_fxd.awk $FXD | sort | uniq > $STEM.pts
    set FILES
    foreach DZ (ENE0060A ENE0061 ENE0062A ENE0159A ENE1061A NNE0725 NWO017 NWO805
NW1200 WNW0001 WNW0123 WNW0809A WNW0813 WNW0835A WNW1053 WNW1127 WNW2225 A2 )
       set DZFILE="DZs/ZFM${DZ}.pan"
       set DIST="Distances/${STEM}_${DZ}.dists"
       if( -f $DZFILE ) then
          if( !( -f $DIST ) ) then
             pancalc2411 $DZFILE ${STEM}.pts > $DIST
          endif
          awk -f extract_distances.awk -v DZ=$DZ $DIST > ${DZ}.tmp
          set FILES="$FILES ${DZ}.tmp"
       else
          echo "$DZFILE not found."
          exit
       endif
    end
    paste $FILES > distances.tmp
    awk -f append_distances.awk distances.tmp $FXD > $STEM.fxdd
    rm -f ${STEM}.pts
    rm *.tmp
 else
    echo "$FXD not found."
 endif
```

condense_fxd.awk

```
BEGIN {
   pan0 = 0;
}
{
   if( NR>1 )
   {
      pan = $1;
      if( pan != pan0 )
      {
         printf( "%s %s %s %s¥n",$1,$4,$5,$6 );
      }
      pan0 = pan;
   }
}
```

extract_distances.awk

```
BEGIN {
   TRUE = 0==0;
   FALSE=!TRUE;
   reading_header = TRUE;
   print "Panel " DZ;
}
{
   if( reading_header )
   {
   #  print "Reading header line" $0;
      if( $1 == "ID" ) reading_header = FALSE;
   }
   else
      print $1 " " $5;
}
```

append_distances.awk

```
BEGIN {
   TRUE = 0==0;
   FALSE=!TRUE;
   reading_distances = TRUE;
}
{
   if( FNR==NR ) # Reading distances.
   {
      if( NR==1 )
      {
         nzones = NF/2;
         for( i=0; i<nzones; i++ ) zone_name[i] = $(2*i+2);
      }
      else
      {
         pan = $1;
         for( i=0; i<nzones; i++ ) distance[pan,i] = $(2*i+2);
      }
   }
   else
   {
      if( FNR==1 )
      {
         printf( "%s",$0 );
         for( i=0; i<nzones; i++ ) printf( " %8s",zone_name[i] );
         printf( "¥n" );
      }
      else
      {
         pan = $1;
         printf( "%s",$0 );
         for( i=0; i<nzones; i++ ) printf( " %8s",distance[pan,i] );
         printf( "¥n" );
      }
   }
}
```

A2.2 Calculation of performance measures

The main script to calculate performance measures for the case of linear scaling is a C-shell (Linux) script named parameter_estimation_v#, and the corresponding script for the case of area-based scaling is named parameter_estimation_v#a, where # = 1,2,3,4, or 5 depending on the data delivery:

1 Delivery 2014-08-24
2 Delivery 2014-08-28
3 Delivery 2014-08-29
4 Delivery 2014-09-12
5 Delivery 2014-09-28

The different versions were to extend the options for different calculation cases, but are practically identical in other respects. The versions for each delivery have been archived. Here just the scripts used for the final delivery (2014-09-28) are presented.

Runs of the final version of the scripts for all 10 realizations of a given Geo-DFN alternative were automated by means of the script run_all_NN_for_variant (for length-based scaling):

```
#!/bin/csh -f
 if ( "blank$4" == "blank" ) then
    echo "Syntax: run_all_NN_for_variant var Topt bopt seed"
    echo "where:"
    echo "   var  = r3, o3, t2"
    echo "   Topt = transmissivity option (semi, corr, or unco)."
    echo "   bopt = aperture option (aspo, hjerne, cubic, or stoch)."
 else
    foreach NN (01 02 03 04 05 06 07 08 09 10)
       parameter_estimation_v5 $1 $NN $2 $3 $4
    end
 endif
```

and the script run_all_NN_for_variant_a (for area-based scaling):

```
#!/bin/csh -f
 if ( "blank$4" == "blank" ) then
    echo "Syntax: run_all_NN_for_variant_a var Topt bopt seed"
    echo "where:"
    echo "   var  = r3, o3, t2"
    echo "   Topt = transmissivity option (semi, corr, or unco)."
    echo "   bopt = aperture option (aspo, hjerne, cubic, or stoch)."
 else
    foreach NN (01 02 03 04 05 06 07 08 09 10)
       parameter_estimation_v5a $1 $NN $2 $3 $4
    end
 endif
```

The scripts parameter_estimation_v5 and parameter_estimation_v5a both function by setting up command-line arguments for the main script that implements the simple series model, parameter_estimation.awk. This script and its subsidiary scripts are written in the AWK programming language (Aho et al., 1988). These scripts are reproduced under separate headings below.

parameter_estimation_v5

```
# Script used to …
#!/bin/csh -f
 set VER  = "Scripts/Version2014-09-12"
 set AWK  = "-f $VER/parameter_estimation.awk -f $VER/repository_heads.awk -f
$VER/HCD_heads.awk -f $VER/Tmodels_skb.awk -f $VER/aperture_models.awk"
 set SAWK = "-f $VER/parest_math.awk"
 set STEM = "SRGeoPFC_$1_$2"
 set FXD  = "HCD_Distances/$STEM.fxdd"
#
 if ( "blank$5" == "blank" ) then
    echo "Syntax: parameter_estimation var NN Topt bopt seed"
    echo "where:"
    echo "   var  = r3, o3, t2"
    echo "   NN   = 01, 02, ..."
    echo "   Topt = transmissivity option (semi, corr, or unco)."
    echo "   bopt = aperture option (aspo, hjerne, cubic, or stoch)."
 else
    set PAWK  = "$VER/inputpars_$3_$4.awk"
    if ( -f $PAWK ) then
       if ( -f $FXD ) then
          set OUT  = "${STEM}_$3_$4_$5.prn"
          set NXS = `grep -c '^' $FXD`
          @ NXS --
          echo "awk -f $PAWK $AWK $SAWK -v N_intersections=$NXS -v SEED=$5 $FXD >
$OUT"
          echo ""
          awk       -f $PAWK $AWK $SAWK -v N_intersections=$NXS -v SEED=$5 $FXD >
$OUT
       else
          echo "Input file $FXD not found."
       endif
    else
       echo "Script $VER/$PAWK for options Topt = $3 and bopt = $4 not found."
    endif
 endif
```

parameter_estimation_v5a

```
#!/bin/csh -f
 set VER  = "Scripts/Version2014-09-12"
 set AWK  = "-f $VER/parameter_estimation.awk -f $VER/repository_heads.awk -f
$VER/HCD_heads.awk -f $VER/Tmodels_skb.awk -f $VER/aperture_models.awk"
 set SAWK = "-f $VER/parest_math.awk"
 set STEM = "SRGeoPFC_$1_$2"
 set FXD  = "HCD_Distances/$STEM.fxdd"
#
 if ( "blank$5" == "blank" ) then
    echo "Syntax: parameter_estimation var NN Topt bopt seed"
    echo "where:"
    echo "   var  = r3, o3, t2"
    echo "   NN   = 01, 02, ..."
    echo "   Topt = transmissivity option (semi, corr, or unco)."
    echo "   bopt = aperture option (aspo, hjerne, cubic, or stoch)."
 else
    set PAWK  = "$VER/inputpars_$3_$4_a.awk"
    if ( -f $PAWK ) then
       if ( -f $FXD ) then
          set OUT  = "${STEM}_$3_$4_$5_a.prn"
          set NXS = `grep -c '^' $FXD`
          @ NXS --
          echo "awk -f $PAWK $AWK $SAWK -v N_intersections=$NXS -v SEED=$5 $FXD >
$OUT"
          echo ""
          awk       -f $PAWK $AWK $SAWK -v N_intersections=$NXS -v SEED=$5 $FXD >
$OUT
       else
          echo "Input file $FXD not found."
       endif
    else
       echo "Script $VER/$PAWK for options Topt = $3 and bopt = $4 not found."
    endif
 endif
```

parameter_estimation.awk

```
function print_header()
{
      printf( "# Program:         parameter_estimation.awk v. 2014-08-29¥n" );
      printf( "# Input file:      %s¥n# Seed value: %d¥n",FILENAME,SEED );
      printf( "# Fracture domain: %s¥n",FDOMAIN );
      printf( "# Transmissivity option: %s   Aperture option: %s   Frequency option:
%s¥n",T_OPT,B_OPT,F_OPT );
      printf( "# Deposition holes:      L_dh %6.2f m  r_dh %6.3f m  N_dh
%d¥n",L_dephole,r_dephole,N_depholes );
      printf( "# Frequency parameters:  P10_PFL[%s] %5.3f /m  r_bh %5.3f m   N_X
%d¥n",FDOMAIN,P10_PFL[FDOMAIN],r_borehole,N_intersections );
#
      printf( "Tun Pos Meets     X (m)        Y (m)   Dip  r_eq (m)  T (m2/s)   b (m)
u_0 (m/y)    t_w (y) F_r (y/m)  L_r (m)  N Discharge Zone¥n" );
}
function set_input_parameters_default()
{
#
#  Set default values of input parameters. Note that these values can be overridden
by the
#  external function set_input_parameters() which is called later.
#
   L_dephole  = 7.83;         # Length of deposition hole in meters.
   r_dephole  = 0.875;        # Radius of deposition hole in meters.
   r_borehole = 0.038;        # Radius of deep core-drilled holes according to
Forsmark SDM 1.2 report (SKB R-05-18 p. 356).
   N_depholes = 6000;         # Number of deposition holes.
   P10_PFL["FFM01"] = 0.005;  # P_10 intensity of flowing features in boreholes (per
m) in FFM01 (from SKB R-08-23, Table 3-4).
   P10_PFL["FFM03"] = 0.05;   # P_10 intensity of flowing features in boreholes (per
m) in FFM03 (from SKB R-08-23, Table 3-6).
                              # The observed linear frequency of flowing fractures in
boreholes
                              # (as an estimate of the number of fractures or
channels, per total length
                              # of deposition holes) that can be expected to connect
to deposition holes;
   L_max = 1000;              # Maximum segment length.
   r_max = 1000 / sqrt( PI ); # Maximum fracture radius (not used).
#  N_intersections = 0;       # Number of fracture/deposition-hole intersections --
Provide as command-line input.
   FDOMAIN = "FFM01";
}
#
function equivalent_transmissivity_series( T,l,nsegs,     i,sum,L )
#
# Calculates the equivalent transmissivity for a series of conductors with
transmissivities:
#   T_i,  i = 0,1,...,nsegs
# and lengths l_i, based on the formula T_eq = L / sum( l_i / T_i ). It is assumed
that all
# segments have the same effective width.
#
{
   sum = 0;
   L   = 0;
   for( i=0; i<nsegs; i++ )
   {
      sum += l[i]/T[i];
      L   += l[i];
```

```
   }
   return( L/sum );
}
function random_connection( P10_flowing, L_factor,      p_c )
{
   p_c = P10_flowing * L_factor; # Probability of this intersection being connected
to the flowing network.
   return( vrand("p") <= p_c );
}
BEGIN {
   TRUE  =  0==0;              # Define some logical constants and mathematical
constants.
   FALSE = !TRUE;
   PI    = 2*atan2(1,0);
   LN10  = log( 10 );
   seconds_per_year = 365.25 * 24 * 3600;
#
   set_input_parameters_default();
   set_input_parameters();         # This function is contained in a separate code
file so that it can easily be changed
                                   # for calculations to test different assumptions.
   initialize_zone_heads();        # This function is contained in a separate code
file, together with the look-up function
                                   # head_in_zone(), to allow specification of
different heads in different discharging HCDs.
                                   # In the simplest case, this is a dummy function
and head_in_zones() returns 0 for all HCDs.
#
   L_factor = L_dephole * N_depholes / N_intersections;
#
   if( F_OPT == "area" )           # Probability of intersection based on ratio of
areas rather than lengths.
   {
      L_factor *= r_dephole/r_borehole;
   }
#
   srand( SEED );   # Initialize the awk random number generator rand() with the seed
value specified on the command line.
   initialize_vrand( "p",N_intersections ); # Initialize table of random values used
for p_c.
   initialize_vrand( "T",N_intersections ); # Initialize table of random values used
for T.
   initialize_vrand( "b",N_intersections ); # Initialize table of random values used
for b.
#
   i0 = 19;         # Position of first deformation zone distance in input line.
}
{
   if( NR==1 ) # Read the first line of the fxdd file which contains the column
headings.
   {
#
#     Print output file header.
#
      print_header();
#
#     Read deformation zone names from first line of fxdd input file. The standard
fxdd file header
#     has 11 extra words in the i0 column headings that precede the zone names, hence
the offset of i0+11.
#
      for( i=i0; i<=NF; i++ )
      {
```

```
         zone_name[i-i0-11] = $i;
      }
   }
   else        # Read and process the next data line in the fxdd file.
   {
      panelID = $1;
#
      r_bound = $2;    # Bounding radius of fracture (not used).
      r_equiv = $3;    # Equivalent radius of fracture.
#
      c[0]    = $4;    # Fracture centroid.
      c[1]    = $5;
      c[2]    = $6;
      n[0]    = $7;    # Fracture normal vector.
      n[1]    = $8;
      n[2]    = $9;
      n[3]    = $10;   # Intercept of fracture plane in form n[0]*x + n[1]*y + n[2]*z
+ n[3] = 0.
#
      EFPCkeep   = $11 == "KEEP";
      EFPCdetect = $12 == "Y";  # D? TRUE if fracture is detectable according to
EFPC-strict flag (i.e. if requiring FPI with deposition hole).
      tunnel     = $13;
      tposition  = $14;
      cross_axis = $15 == "Y";  # X? TRUE if fracture crosses axis within the length
of the deposition hole.
#
      X[0]    = $16;   # Intersection coordinates.
      X[1]    = $17;
      X[2]    = $18;
#
#     Read distances from deposition holes to discharging deformation zone and find
the closest one.
#
      Lzone = 1e20;
      for( i=i0; i<=NF; i++ )
      {
         L = $i;
         if( L<Lzone )
         {
            Lzone = L;
            nzone = i-i0;
         }
      }
      connected = random_connection( P10_PFL[FDOMAIN], L_factor );
#
      if( connected )
      {
         n2 = n[2];
         if( n2 < 0 ) n2 = -n2;
         dip = 180*acos( n2 )/PI;                                  # Dip of
intersecting fracture in degrees (for output).
#
      #  printf( "Segment 0: L = %g¥n",r_equiv );
         l[0] = r_equiv;                                           # First segment
assumed to have length equal to the fracture radius.
         T[0] = segment_transmissivity( r_equiv,FDOMAIN,T_OPT );
         nsegs = 1;
         L_residual =  Lzone - r_equiv;                            # Note this assumes
no tortuosity.
         while( L_residual > 0 )
         {
            r = L_residual;
```

```
            if( r > L_max ) r = L_max;                              # Segments cannot be
longer than the maximum fracture extent.
         #  printf( "Segment %d: L = %g¥n",nsegs,r );
            l[nsegs] = r;
            T[nsegs] = segment_transmissivity( r,FDOMAIN,T_OPT );
            nsegs++;
            L_residual -= r;
         }
         L_r = 0;
         for( i=0; i<nsegs; i++ )
         {
            L_r += l[i];                                            # Cumulative length
of path from deposition hole to zone.
            b[i] = transport_aperture( T[i],B_OPT );                # Transport aperture
for segment.
         }
         Tequiv = equivalent_transmissivity_series( T,l,nsegs ); # Equivalent
transmissivity of path.
         dh  = local_head_in_repository( X[0],X[1] );               # Head difference
from deposition hole
         dh -= head_in_zone( nzone );                               # to nearest
discharging zone.
         q   = dh*Tequiv/L_r;                                       # Flux density
(flowrate per unit width).
#
#        Calculate the total advective transport time and transport resistance along
the path.
#
         F_r = 0;
         t_r = 0;
         u_0 = q/b[0];                                              # Advective velocity
in the initial segment.
         for( i=0; i<nsegs; i++ )
         {
            u  = q/b[i];                                            # Advective velocity
in the ith segment.
            dl = l[i];                                              # Segment length.
            dt = dl/u;                                              # Advective travel
time in the ith segment.
            dF = 2*dl/q;                                            # dF = a_w * dl / u
=  2*dl / (b*u);
            t_r += dt;                                              # Add to sums for
t_r and F_r.
            F_r += dF;
         }
         u_r = L_r / t_r;                                           # Mean advective
velocity.

#
#        Scale from units of seconds and m/s units of years and m/y.
#
         u_0 *= seconds_per_year;
         t_r /= seconds_per_year;
         F_r /= seconds_per_year;
#
#        Output follows:
#
         printf( "%3d %3d ",tunnel,tposition );
         if( EFPCkeep )                                             # Record whether
acceptable with EFPC ...
            printf( "EFPC" );
         else                                                       # ... or just with
FPC.
```

```
            printf( "FPC " )
         printf( " %12.2f %12.2f",X[0],X[1] );                  # Record position of
deposition hole.
         printf( " %3d %9.2f %9.3e %9.7f",dip,r_equiv,T[0],b[0] );      # Record
initial r_equiv, T and b.
         printf( " %9.5f %10.3f %9.3e %8.2f",u_0,t_r,F_r,L_r ); # Record performance
measures.
         printf( " %2d %-12s",nsegs,zone_name[nzone] );
         printf( "¥n" );
      }
   }
}
```

repository_heads.awk

```
function local_head_in_repository( X,Y,     h )
{
   h = 2;        # Moderately pessimistic value. Upper end of range calculated by
Geier (2010) DFM model was >1 m,
                 # 0.01 m/m gradient of SKB TR-08-05 Figure 8-62 gives 2 m for a
typical transport distance of 200 m.
   return( h );
}
```

HCD_heads.awk

```
function head_in_zone( nzone,     h )
{
   h = 0;
   return( h );
}
function initialize_zone_heads(     h )
{
   h = 0;
}
```

Tmodels_skb.awk

```
#
# SKB's DFN interpretation of fracture transmissivity distributions
# Based on Tables C-1 and C-3 of SKB R-08-95 as in 2013-08 erratum..
#
function SKB_transmissivity_FFM01( r,opt,   T )
{
   if( opt == "semi" )
      T = loglinear_correlation( r, 5.3e-11,  0.5, 1.0, "T" ); # Semi-correlated
model.
   else if( opt == "corr" )
      T = loglinear_correlation( r, 1.8e-10,  0.5, 0.0, "T" ); # Correlated model.
   else
      T = loglinear_correlation( r, 1.58e-9,  0.0, 1.0, "T" ); # Uncorrelated model
with a = 10^(-8.8) = 1.58e-9

   return( T );
}
function SKB_transmissivity_FFM03( r,opt,   T )
{
   if( opt == "semi" )
      T = loglinear_correlation( r, 1.8e-8, 0.3, 0.5, "T" ); # Semi-correlated model.
   else if( opt == "corr" )
      T = loglinear_correlation( r, 7.1e-9, 0.6, 0.0, "T" ); # Correlated model.
   else
      T = loglinear_correlation( r, 6.3e-8, 0.0, 0.8, "T" ); # Uncorrelated model
with a = 10^(-7.2) = 6.3e-8
   return( T );
}
function segment_transmissivity( r,fdomain,corr_opt,    T )
{
   if( fdomain == "FFM01" || fdomain == "FFM06" )
      T = SKB_transmissivity_FFM01( r,corr_opt );
   else if( fdomain == "FFM03" )
      T = SKB_transmissivity_FFM03( r,corr_opt );
   return( T );
}
```

aperture_models.awk

```
function transport_aperture( T,aperture_option,    b )
{
#  Various empirical relationships for fracture hydraulic aperture vs. fracture
transport aperture or its inverse, flow-wetted surface.
#
   if( aperture_option == "aspo" )        # Aspo Task Force model (Dershowitz et al.,
2003 ): b = 0.5 * T^0.5
      b = 0.5 * exp( 0.5 * log( T ) );
   else if( aperture_option == "hjerne" ) # Hjerne et al. (2010) model b = 0.28 *
T^0.3 (SKB TR-10-52, Figure 6-66).
      b = 0.28 * exp( 0.3 * log( T ) );
   else if( aperture_option == "cubic" )  # Cubic law
      b = 0.0117 * exp( log( T )/3 );     # Coefficient from SKB TR-10-52, Figure 6-
66 as calculated by Hjerne et al. for density 1000 kg/m3 and viscosity of 1.3 cP at
10 C.
   else if( aperture_option == "stoch" )  # Stochastic model based on Aspo Task Force
model but with a half-order-magnitude standard deviation.
      b = loglinear_correlation( T,0.5,0.5,0.5,"b" );
   return( b );
}
```

inputpars_corr_aspo.awk

```
function set_input_parameters()
{
   L_max = 1000;              # Maximum segment length.
   FDOMAIN = "FFM01";
   T_OPT   = "corr";
   B_OPT   = "aspo";
   F_OPT   = "length";
}
```

inputpars_corr_aspo_a.awk

```
function set_input_parameters()
{
   L_max = 1000;              # Maximum segment length.
   FDOMAIN = "FFM01";
   T_OPT   = "corr";
   B_OPT   = "aspo";
   F_OPT   = "area";
}
```

inputpars_semi_aspo.awk

```
function set_input_parameters()
{
   L_max = 1000;              # Maximum segment length.
   FDOMAIN = "FFM01";
   T_OPT   = "semi";
   B_OPT   = "aspo";
}
```

inputpars_semi_aspo_a.awk

```
function set_input_parameters()
{
   L_max = 1000;              # Maximum segment length.
   FDOMAIN = "FFM01";
   T_OPT   = "semi";
   B_OPT   = "aspo";
   F_OPT   = "area";
}
```

inputpars_semi_cubic.awk

```
function set_input_parameters()
{
   L_max = 1000;              # Maximum segment length.
   FDOMAIN = "FFM01";
   T_OPT   = "semi";
   B_OPT   = "cubic";
   F_OPT   = "length";
}
```

inputpars_semi_cubic_a.awk

```
function set_input_parameters()
{
   L_max = 1000;              # Maximum segment length.
   FDOMAIN = "FFM01";
   T_OPT   = "semi";
   B_OPT   = "cubic";
   F_OPT   = "area";
}
```

inputpars_semi_hjerne.awk

```
function set_input_parameters()
{
   L_max = 1000;              # Maximum segment length.
   FDOMAIN = "FFM01";
   T_OPT   = "semi";
   B_OPT   = "hjerne";
   F_OPT   = "length";
}
```

inputpars_semi_hjerne_a.awk

```
function set_input_parameters()
{
   L_max = 1000;              # Maximum segment length.
   FDOMAIN = "FFM01";
   T_OPT   = "semi";
   B_OPT   = "hjerne";
   F_OPT   = "area";
}
```

inputpars_semi_stoch.awk

```
#function set_input_parameters()
{
   L_max = 1000;              # Maximum segment length.
   FDOMAIN = "FFM01";
   T_OPT   = "semi";
   B_OPT   = "stoch";
   F_OPT   = "length";
}
```

inputpars_semi_stoch_a.awk

```
function set_input_parameters()
{
   L_max = 1000;              # Maximum segment length.
   FDOMAIN = "FFM01";
   T_OPT   = "semi";
   B_OPT   = "stoch";
   F_OPT   = "area";
}
```

inputpars_unco_aspo.awk

```
function set_input_parameters()
{
   L_max = 1000;              # Maximum segment length.
   FDOMAIN = "FFM01";
   T_OPT   = "unco";
   B_OPT   = "aspo";
   F_OPT   = "length";
}
```

inputpars_unco_aspo_a.awk

```
function set_input_parameters()
{
   L_max = 1000;              # Maximum segment length.
   FDOMAIN = "FFM01";
   T_OPT   = "unco";
   B_OPT   = "aspo";
   F_OPT   = "area";
}
```

inputpars_unco_hjerne.awk

```
function set_input_parameters()
{
   L_max = 1000;              # Maximum segment length.
   FDOMAIN = "FFM01";
   T_OPT   = "unco";
   B_OPT   = "hjerne";
   F_OPT   = "length";
}
```

inputpars_unco_hjerne_a.awk

```
function set_input_parameters()
{
   L_max = 1000;              # Maximum segment length.
   FDOMAIN = "FFM01";
   T_OPT   = "unco";
   B_OPT   = "hjerne";
   F_OPT   = "area";
}
```

parest_math.awk

```
#*********************************************************************
# Standard mathematical functions and random simulation functions.
#*********************************************************************
#
#*********************************************************************
# Inverse trigonometric functions not supported by standard AWK.
#*********************************************************************
#
function atrig_setup( )
{
   PI_2 = atan2(1,0);
   PI   = 2*PI_2;
}
function acos( x,    c )
{
   if( PI_2 == 0 ) atrig_setup();
   if( x == 0 )
      c = PI_2;
   else
   {
      c = sqrt( 1-x*x )/x;
      c = atan2( c,1 );
      if( x < 0 ) c = PI + c;
   }
   return( c );
}
function atan( x )
{
   return( atan2( x,1 ) );
}
function asin( x )
{
   if( PI_2 == 0 ) atrig_setup();
   return( PI_2 - acos( x ) );
}
#
#*********************************************************************
# vrand(t)
#*********************************************************************
function initialize_vrand( t,N,      i )
{
   for( i=0; i<N; i++ )
      R_vrand[t,i] = rand();  # Fill the list with N random values.
   N_vrand[t] = N;            # Store the number of values for thread t.
   I_vrand[t] = 0;            # Initialize pointer to first value.
}
function vrand( t,     i )
{
   i = I_vrand[t] % N_vrand[t];
   I_vrand[t]++;
   return( R_vrand[t,i] );
}
#
#*********************************************************************
# GaussianDev(t):
# Returns a normally distributed deviate with zero mean and
# unit variance, using the Box-Muller transformation. From the
# book "Numerical Recipes," by Press et al, 1986, p.203.
# Input : iseed  = seed for random number generator
# Output: gasdev = normally distributed deviate
# Adapted for multiple threads 2014-08-28.
#*********************************************************************
```

```
#
function GaussianDev ( t,     v1,v2,r,fac )
{
   if( GaussianDev_iset[t] == 0 )
   {
      do
      {
         v1 = 2 * vrand(t) - 1;
         v2 = 2 * vrand(t) - 1;
         r  = v1 * v1 + v2 * v2;
      }
      while( r >= 1 );

      fac = sqrt( -2 * log( r ) / r );
      GaussianDev_gset[t] = v1 * fac;
      GaussianDev_iset[t] = 1;
      r = v2 * fac;
   }
   else
   {
      GaussianDev_iset[t] = 0;
      r = GaussianDev_gset[t];
   }
   return( r );
}
#
#*********************************************************************
# loglinear_correlation( x,a,b,sigma,t)
#
# Generate values of the form:
#
#    log10 y = log10 a + b log10 x + sigma * N(0,1)
#
# or equivalently:
#
#    y = a * x^b * 10^[sigma*N(0,1)]
#
# where log10 is the base-10 logarithm. The special cases:
#    b = 0 ( uncorrelated model with lognormal variation around the logarithmic mean.
#    sigma = 0 (perfectly correlated model)
# are also handled efficiently.
# Multithread version where t = index to thread.
#*********************************************************************
#
function loglinear_correlation( x, a, b, sigma, t,      y,d )
{
   y = a;
   if( b != 0 )
      y *= exp( b*log(x) );
   if( sigma != 0 )
   {
      d = sigma * GaussianDev(t);
      y *= exp( d*LN10 );
   }
   return( y );
}
      T = loglinear_correlation( r, 1.8e-10,  0.5, 0.0, "T" ); # Correlated model.
```

2015:40

The Swedish Radiation Safety Authority has a comprehensive responsibility to ensure that society is safe from the effects of radiation. The Authority works to achieve radiation safety in a number of areas: nuclear power, medical care as well as commercial products and services. The Authority also works to achieve protection from natural radiation and to increase the level of radiation safety internationally.

The Swedish Radiation Safety Authority works proactively and preventively to protect people and the environment from the harmful effects of radiation, now and in the future. The Authority issues regulations and supervises compliance, while also supporting research, providing training and information, and issuing advice. Often, activities involving radiation require licences issued by the Authority. The Swedish Radiation Safety Authority maintains emergency preparedness around the clock with the aim of limiting the aftermath of radiation accidents and the unintentional spreading of radioactive substances. The Authority participates in international co-operation in order to promote radiation safety and finances projects aiming to raise the level of radiation safety in certain Eastern European countries.

The Authority reports to the Ministry of the Environment and has around 300 employees with competencies in the fields of engineering, natural and behavioural sciences, law, economics and communications. We have received quality, environmental and working environment certification.

Strålsäkerhetsmyndigheten
Swedish Radiation Safety Authority

SE-171 16 Stockholm
Solna strandväg 96

Tel: +46 8 799 40 00
Fax: +46 8 799 40 10

E-mail: registrator@ssm.se
Web: stralsakerhetsmyndigheten.se